NATIONAL UNIVERSITY OF IRELAND MAYNOOTH

Design and Analysis of Quasioptical Components for use in Terahertz Optics and Future CMB Missions

by

David Byrne

A thesis submitted in partial fulfillment for the degree of Master of Science

in the

Faculty of Science and Engineering

Experimental Physics Department

February 2021

Declaration of Authorship

I, David Byrne, declare that this thesis titled, 'Design and Analysis of Quasioptical Components for use in Terahertz Optics and Future CMB Missions' and the work presented in it are my own. I confirm that:

- This work was done wholly or mainly while in candidature for a research degree at this University.
- Where any part of this thesis has previously been submitted for a degree or any other qualification at this University or any other institution, this has been clearly stated.
- Where I have consulted the published work of others, this is always clearly attributed.
- Where I have quoted from the work of others, the source is always given. With the exception of such quotations, this thesis is entirely my own work.
- I have acknowledged all main sources of help.
- Where the thesis is based on work done by myself jointly with others, I have made clear exactly what was done by others and what I have contributed myself.

Signed: 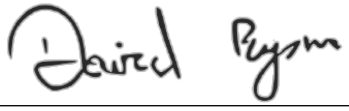

Date: 30/10/2020

Abstract

The main topic of this thesis concerns itself with the development and analysis of optical components used in CMB (Cosmic Microwave Background) missions in the terahertz frequency spectrum. In particular, the optical performance of PRISTINE, a mission proposal for the ESA fast (F) mission call and a PLA (Polylatic Acid) GRIN (Gradient Index) lens was analysed using GBM (Gaussian Beam Mode) theory and PO (Physical Optics). This thesis also includes the work the author did as part of an international team of 16 students to design a candidate ESA mission. The final chapter, therefore, concerns itself with "Geophysics from Space using Micro-or Nano-Satellite Constellations" and is separate from the rest of the thesis.

Detailed analysis of PRISTINE was carried out in *GRASP 10.5* a commercial package which uses PTD (Physical Theory of Diffraction) and PO to measure the EM (Electromagnetic) radiation generated from reflector antennas. The EM fields predicted from GRASP were compared with GBMA (Gaussian Beam Mode Analysis). The beam quality of PRISTINE was tested using its Gaussicity and ellipticity (this was the chosen method used to compare the simulated data with the theoretically predicted data). Each surface of PRISITNE's twelve mirror pFTS (polarising Fourier Transform Spectrometer) was designed using code written by the author to optimise the focusing and collimation of each elliptical surface from criteria outlined in Chapter 3.

Chapter 4 deals with the design, manufacturing and analysis of a 3-D printed PLA GRIN lens designed to focus W-band radiation (75-110 GHz) 250 mm from the lens. For this, a commercial package known as *CST* microwave was used to analyse the refracted radiation. The simulated radiation was also compared with GBM analysis and the experimental lab data performed in Maynooth University's VNA (Vector Network Analyser) laboratory. Along with this, some material analysis was performed at 100 GHz in the laboratory to determine the permittivity of the PLA. The final section of this thesis moves away from quasi-optical analysis and instead concerns itself with Geophysics. MAGMA-C is a proposed eight satellite constellation in a Low Earth Orbit (LEO) to measure the Earth's magnetic field to study the induced magnetic field in the mantle. The primary goal of the MAGMA-C mission is to map Earth's mantle conductivity derived from its induced magnetic field. The secondary goal of this mission is to use this conductivity profile to better estimate the water content of the mantle.

Acknowledgements

I would first of all like to give a special thanks to my supervisor for all of his guidance and insight throughout my thesis. Neil's open door policy and his wealth of knowledge benefited my academic growth and the writing of my thesis. I would like to thank all of the staff of the Experimental Physics Department at Maynooth University for all of the help you provided me with throughout my thesis. I would like to thank Gráinne, who was always there to help. No matter what the situation, Gráinne always had the solutions. I would like to thank Pat Seery and David Watson for all their assistance with manufacturing equipment and for helping me to become more knowledgeable in their fields. I would like to thank Dr Créidhe O'Sullivan for all her help with Gaussian Beam modes and her amazing work as the newly appointed head of the department. I would also like to give special thanks to Dr Marcin Gradziel for his time and assistance in the VNA lab.

I would like to thank all my fellow postgrads of the Experimental Physics for everything from their insights into particular subjects to all of the laughter and memories I will cherish. Thank you, Julianne, David, Aisling, James, and Jack. Special thanks to Joe for all of the help you gave me in the VNA lab. Special thanks to Andrew for all Python related question you helped me with. I want to thank my partner Megan for all the love and support (during the highs and lows) she gave me, without which writing this thesis would have been much more difficult. Lastly, I would like to thank my family for all their support. Thank you, Mam, Dad, Craig and Lauryn for all your support.

Contents

Declaration of Authorship i

Abstract ii

Acknowledgements iii

List of Figures viii

List of Tables xi

Abbreviations xii

1 Background and Theory 1
- 1.1 Introduction . . . 1
- 1.2 Submilimeter and Infared Optics . . . 2
- 1.3 The Big Bang Theory and Cosmic Background Radiation . . . 4
  - 1.3.1 The Big Bang Theory . . . 4
  - 1.3.2 Cosmic Background Radiation . . . 4
  - 1.3.3 Pertubations (Anisotropies or Temperature Variations) . . . 8
  - 1.3.4 E-mode and B-mode Polarisation . . . 12
- 1.4 3D Printing . . . 16
  - 1.4.1 3-D Printing and PLA . . . 16
  - 1.4.2 Extrusion System . . . 17
  - 1.4.3 Layering and Meshing . . . 18
- 1.5 S-Parameters . . . 19
  - 1.5.1 Standing Wave Filter . . . 21
- 1.6 Thesis Outline . . . 23
  - 1.6.1 Chapter 2 . . . 23
  - 1.6.2 Chapter 3 . . . 23
  - 1.6.3 Chapter 4 . . . 24
  - 1.6.4 Chapter 5 . . . 24

2 Optical Design and Analytical tools for modelling Quasi-optical systems 25

2.1 Gaussian Beam Analysis . . . 25
2.1.1 Gaussian Beam Mode Propagation . . . 26
2.1.2 Higher Order Modes (Cylindrical Coordinates) . . . 29
2.1.3 Confocal Distance . . . 31
2.2 ABCD Matricies . . . 32
2.3 Commonly Used ABCD Matricies . . . 35
2.3.1 Uniform Medium . . . 36
2.3.2 Curved Surfaces . . . 36
2.3.3 Thin Lens . . . 37
2.3.4 Thick Lens . . . 37
2.3.5 Elliptical and Spherical Mirrors . . . 38
2.4 Gaussian Beam Telescopes . . . 38
2.5 GRASP 10.5 . . . 39
2.5.1 Introduction . . . 39
2.5.2 Geometrical Objects . . . 39
2.5.2.1 Surfaces . . . 39
2.5.2.2 Rims . . . 43
2.5.3 Electrical Objects . . . 44
2.5.3.1 PO (Physical Optics) . . . 45
2.5.3.2 Feed . . . 45
2.5.3.3 Planar Cut . . . 46
2.5.3.4 Planar Grid . . . 48
2.5.4 Dual Reflector Wizard . . . 50
2.5.4.1 Mizuguchi Condition . . . 51
2.5.5 Commands . . . 51
2.6 CST . . . 52
2.6.1 CST Solvers . . . 55
2.6.2 Gaussian Beam Solver . . . 56

3 Pristine **58**
3.1 Introduction . . . 58
3.2 Primary Science Goals . . . 59
3.2.1 Secondary Science Goals . . . 61
3.3 Requirements . . . 62
3.4 GRASP Output Beam Characterisation . . . 63
3.4.1 Beam Fitting . . . 63
3.4.1.1 Verification of a Predefined Gaussian Function . . . 64
3.4.1.2 Example of *GRASP 10.5* Data Fitted to Gaussian Model . . . 65
3.4.2 Gaussicity & Ellipticity . . . 65
3.4.2.1 Gaussicity . . . 65
3.4.2.2 Ellipticity . . . 66
3.5 Optical Design . . . 67
3.5.1 12 Mirror Array . . . 69

3.6 Analysis of the pFTS Array . . . 73
3.6.1 Mirror 1 & 2 . . . 73
3.6.2 Mirrors 3-12 . . . 76
3.6.3 Beam Exiting the Array . . . 79
3.6.4 Cassegrain Telescope Design . . . 81
3.7 Conclusion . . . 87

4 GRIN Lens - Gradient index lens 90
4.1 Introduction . . . 90
4.2 Lens Design . . . 92
4.2.1 Prototype Lens CST Simulation . . . 94
4.3 Prototype Lens Manufacturing . . . 96
4.4 VNA(Vector Network Analyser) Description & Mathematical Model 97
4.4.1 Measurement System . . . 98
4.4.2 Vector Analysis Analyser . . . 99
4.4.3 Feed Horn . . . 100
4.4.4 Receiver Port . . . 101
4.4.5 Device Under Test . . . 102
4.4.6 Lens Mounting . . . 102
4.4.7 VNA Interface . . . 103
4.4.8 Scanning Control System . . . 104
4.4.9 Scatter Matrix . . . 105
4.4.10 Calibration . . . 106
4.4.11 Alignment . . . 107
4.4.11.1 Initial Alignment & Transitional Stage Setup . . . 107
4.4.11.2 Alignment Procedure . . . 108
4.4.11.3 Through & Reflection Standard . . . 110
4.4.12 GBMA of GRIN Lens . . . 112
4.5 Protolens Lab Measurements . . . 117
4.5.1 Measurements . . . 118
4.5.2 PLA Testing . . . 119
4.5.3 PLA Measurements . . . 120
4.6 Final Lens Design & Manufacturing . . . 125
4.7 Final Lens CST and ABCD Simulations . . . 127
4.7.1 Beam Normalisation . . . 127
4.7.2 CST Modeling . . . 129
4.8 Final Lens Lab Results & Measurements . . . 134
4.8.1 Measurements . . . 134
4.9 Conclusion . . . 138

5 MAGMA-C geomagnetic space mission 140
5.1 Alpbach Summer School . . . 140
5.2 Mission Overview . . . 141
5.3 State of the Art . . . 142

5.4 Background and Theory . . . 145
5.4.1 Ionospheric Variations . . . 148
5.5 Mission Objectives and Scientific Requirements . . . 148
Science Objectives . . . 148
Primary Objectives . . . 149
Specific Objectives . . . 149
5.6 How Can We Achieve This? . . . 150
5.6.1 The Geomagnetic Field Model . . . 151
5.6.2 Measurement of Magnetic Field Components to Conductivity Profile . . . 157
5.7 Selected Inducing Sources to Map Induced Responses in the Mantle 158
5.7.1 Separation of Magnetic Field Contributions . . . 161
5.7.2 Summary of the Scientific Requirements . . . 163
5.8 Data Products . . . 163
5.9 Payload . . . 164
5.10 Mission Profile . . . 166
5.10.1 Launch and Operations . . . 167
5.11 Spacecraft Design . . . 168
5.11.1 Structure and Mechanisms . . . 168
5.11.2 Summary of Propulsion, Altitude Orbit Control and Thermal Systems . . . 169
5.11.3 Power & Power Budget . . . 170
5.12 Descoping Options and Risk Analysis . . . 171
5.12.1 *In case of boom deployment malfunction* . . . 171
5.12.2 *In case of launch failure* . . . 171
5.12.3 Risk Analysis . . . 171
5.13 Programmatic Considerations . . . 173
5.14 Conclusion . . . 173

A Lens Designer Code **175**

B Ellipse parameters **178**

Bibliography **183**

List of Figures

1.1 Atmosphere transmission spectrum . . . 3
1.2 The Big Bang . . . 6
1.3 Hydrogen helium abundance . . . 7
1.4 COBE, WMAP, Planck . . . 8
1.5 Fluid oscillations . . . 10
1.6 Angular frequency . . . 11
1.7 Temperature power spectrum . . . 11
1.8 E and B mode polarisations . . . 13
1.9 Thomson scattering . . . 14
1.10 Scalar and Tensor perturbations . . . 15
1.11 3D printer . . . 17
1.12 Nozzle . . . 18
1.13 PLA infill patterns . . . 19
1.14 S-parameters . . . 20
1.15 Two port S-parameter . . . 20
1.16 Schematic diagram of S matrix parameters of a two horn system. . . 22

2.1 Radius and Waist . . . 29
2.2 Confocal distance . . . 32
2.3 ABCD Matrix . . . 33
2.4 Ray Transfer Matrix . . . 35
2.5 Surface Options . . . 40
2.6 2nd Order Polynomial Options . . . 41
2.7 Ellipse parameters *GRASP10.5* . . . 43
2.8 Ray tracing for elliptical mirror . . . 44
2.9 Inputs for PO class . . . 45
2.10 Inputs for Gaussian source . . . 46
2.11 Inputs for planar cuts . . . 47
2.12 Planar cut example . . . 48
2.13 Planar grid parameters . . . 49
2.14 Planar grid example . . . 50
2.15 Reflector wizard . . . 51
2.16 GRASP command window . . . 52
2.17 CST mesh . . . 53
2.18 Tetrahedral mesh . . . 55

2.19 Leapfrog method . . . 56
2.20 Gaussian beam propagation CST . . . 56
2.21 Gaussian beam CST . . . 57

3.1 PRISTINE 12 mirror array schematic . . . 68
3.2 GRASP 12 mirror design . . . 70
3.3 Mirror1 . . . 71
3.4 Mirror 3 . . . 72
3.5 Co and cross polar grid M1 . . . 74
3.6 Co and cross polar cut M1 . . . 74
3.7 M1 fitting data . . . 76
3.8 Co and cross polar grids M3 . . . 77
3.9 Co and cross polar cut M3 . . . 77
3.10 Fitting data M3 . . . 78
3.11 Co and cross polar grids M12 . . . 79
3.12 Co and cross polar cut M12 . . . 80
3.13 Fitting data M12 . . . 81
3.14 Cassegrain schematic . . . 81
3.15 Cassegrain design GRASP . . . 82
3.16 Co and cross polar grids Cassegrain . . . 83
3.17 Co and cross polar cut Cassegrain . . . 84
3.18 Cassegrain farfield cut . . . 85
3.19 Fitting data for Cassegrain . . . 86

4.1 Snells law . . . 90
4.2 GRIN schematic . . . 92
4.3 Step function . . . 93
4.4 Lens power distribution . . . 93
4.5 GRIN lens CST . . . 94
4.6 Proto - lens propagation . . . 95
4.7 Printed proto - lens . . . 96
4.8 Converter head . . . 98
4.9 Emitter - receiver schematic . . . 98
4.10 VNA configuration . . . 99
4.11 Emitter - receiver - VNA schematic . . . 100
4.12 Horn performance . . . 101
4.13 Emitter - receiver - DUT schematic . . . 102
4.14 3D printed lens holder and sample holder . . . 103
4.15 Labview . . . 104
4.16 Scatter matrix schematic . . . 106
4.17 Calibration heads . . . 106
4.18 Lab optical bench setup . . . 108
4.19 Scan 3 lab optical bench setup . . . 109
4.20 Alignment process . . . 110
4.21 Aperture alignment plate . . . 111

4.22 Reflection plate . . . 111
4.23 Full schematic of optical bench . . . 112
4.24 Beam mode selection . . . 116
4.25 preliminary focus of proto - lens . . . 118
4.26 Infill sample percentages . . . 120
4.27 Scematic of optical bench for sample scans . . . 122
4.28 S_{11} and S_{22} for each infill sample . . . 123
4.29 Permittivity Vs infill percentage . . . 124
4.30 Lens visualisation . . . 126
4.31 3D printed final lens . . . 126
4.32 Propagation of GRIN lens predicted by ABCD matrix . . . 128
4.33 Truncated Bessel Vs Gaussian beam normalised to unity power . . . 128
4.34 Truncated Bessel Vs Gaussian beam normalised on axis to 1 . . . 129
4.35 Propagation of beam in CST . . . 130
4.36 20 mode Vs 1 mode . . . 131
4.37 Beam development(CST,perfect Gaussian and ABCD matrix) . . . 132
4.38 CST and ABCD data at beam focus . . . 133
4.39 Intensity plot of CST beam Vs lab measurements . . . 134
4.40 Lab intensities . . . 135
4.41 100 GHz normalised intensities . . . 137
4.42 W band normalised intensities . . . 137

5.1 Orsted . . . 142
5.2 Orsted: Earths Dipole . . . 143
5.3 SWARM . . . 144
5.4 Schematic magnetosphere . . . 147
5.5 X, Y, Z, H, I, D and f components of magnetic field . . . 155
5.6 Field Components . . . 156
5.7 Schematic magnetosphere . . . 156
5.8 Internal external . . . 158
5.9 Inducing sources . . . 159
5.10 3D-conductivity models . . . 161
5.11 Instruments requirements . . . 164
5.12 Vector Field Magnetometer . . . 165
5.13 Scalar magnetic field . . . 165
5.14 Star tracker . . . 165
5.15 Orbits . . . 167
5.16 Spacecraft Design . . . 168
5.17 Risk . . . 172

List of Tables

2.1 Ellipse Variables 42

3.1 Returned parameters from the fitting code using a predefined Gaussian as the data set 64
3.2 Returned parameters from the fitting code using GRASP 10.5 data as the data set 65
3.3 Geometric parameters of elliptical surface for M1&M2 70
3.4 Elliptical parameters for M3-M12 72
3.5 Gaussian beam parameters for a beam reflected from M1 using an initial ω_x and ω_y of 10 mm 75
3.6 Gaussian beam parameters for M3 - M12 78
3.7 Gaussian beam parameters for M12 beam exit 80
3.8 Geometric parameters for the primary and secondary mirrors of the Cassegrain telescope 82
3.9 Left: Gaussian beam parameters for a cut taken 850 mm from the Cassegrain primary mirror. Rigth: Gaussian beam parameters for spherical farfield cut. 84

4.1 Permitivity profile of prototype lens 94
4.2 Test design parameters 97
4.3 Table of mode coefficients for the first 20 Laguerre-Gaussian 115
4.4 Infill percentages and sample thickness 119
4.5 Table of improved ϵ_r measurements for different infill percentages at 100 GHz 124
4.6 Table of relative permitivities and their corresponding percentage infills 126
4.7 Beam waists and distances from GRIN lens 130

5.1 Required periods and corresponding penetration depth 160
5.2 Summary of Science Requirements 163
5.3 tab:Constellation orbital param 166
5.4 Summary of Propulsion, Altitude Orbit Control and Thermal systems 170
5.5 Summary of the power budget for each operating system 170
5.6 Mission Schedule 173

Abbreviations

GBM	**G**aussian **B**eam **M**ode
GBMA	**G**aussian **B**eam **M**ode **A**nalysis
PO	**P**hysical **O**ptics
EM	**E**lectromagnetic
CMB	**C**osmic **M**icrowave **B**ackground
CBR	**C**osmic **B**ackground **R**adation
ESA	**E**uropean **S**pace **A**gency
PLA	**P**oly**L**atic **A**cid
pFTS	**p**olarising **F**ourier **T**ransform **S**pectrometer
PTD	**P**hysical **T**heory of **D**iffraction
VNA	**V**ector **N**etwrk **A**naliser
GRIN	**GR**adient **IN**dex
COBE	**CO**smic **B**ackground **E**xplorer
WMAP	**W**ilkinson **M**icrowave **A**nisotropy **P**robe
DUT	**D**evice **U**nder **T**est
ΛCDM	Λ (Cosmological Constant) **C**old **D**ark **M**atter
PRISNTINE	**P**olarised **R**adiation **I**nterferometer for **S**pectral dis**T**ortions and **IN**flation **E**xploration
CST	**C**omputational **S**imulation **T**echnology
FIT	**F**inite **I**ntegration **T**echnique

Chapter 1

Background and Theory

1.1 Introduction

The work presented in this thesis was undertaken from October 2018 to September 2020 as part of the author's MSc through research. Research into several topics such as reflector antenna design, planar lens design and development at W-band frequencies (75 - 110 GHz), PLA material testing and development of a geophysics space mission to measure the Earth's induced magnetic field of the mantle are discussed in detail.

In this thesis, the optical modelling of a millimetre/sub-millimetre receiver known as PRISTINE is conducted. PRISTINE is a space mission proposed as part of ESA's fast (F) mission opportunities. Its goal is to map the CMB temperature anisotropies and B-mode polarisation (all of these concepts are outlined in this chapter), which would allow for the measurement of polarisation patterns caused by relic gravitational waves produced during inflation. The author specifically worked on the optical design and analysis of the pFTS (seen in Chapter 3). PRISTINE will ultimately operate in the 90 - 3000 GHz range, using an array of multimoded horns. However, the author's design and analysis of PRISTINE was

carried out in *GRASP 10.5* at a frequency of 150 GHz, using only a single mode for preliminary optical analysis.

A significant part of this thesis deals with the design, manufacturing and analysis of a PLA GRIN lens optimised to operate at 100 GHz. The compact size of the lens and ease of access to 3 D printers make it ideal for prototyping lens designs in the laboratory for operation at terahertz frequencies. The GRIN lens was tested in the VNA (Vector Network Analyser) laboratory in the Experimental Physics Department at Maynooth University at W band frequencies. These results were then modelled (using GBMA and ray transfer matrices outlined in section Chapter 2) and simulated using CST (outlined in section 2.6).

The terahertz spectrum spans the region between the radio bands to the infrared spectrum. This means the technology used at these frequencies is a mixture of radio technology such as horns and antennas, and more traditional optical devices such as lenses and mirrors. This chapter describes the background information relating to terahertz astronomy, cosmology and the CMB radiation. A brief history of the CMB is given, including the most recent discoveries. This is followed by some general information describing the operation of 3D printers and scatter matrices.

1.2 Submilimeter and Infared Optics

Not all the EM radiation that is incident on the Earth's atmosphere is able to reach ground-based observatories. For a large part of the frequency spectrum the waves are either absorbed or reflected back into space, so they cannot be measured. The submillimeter and infrared ranges fall in this category.

There are frequency bands throughout the EM spectrum that are unaffected by the Earth's atmosphere, and can travel freely to the surface. When it comes to microwave radiation there is a spectrum of transmission depending on the incident

radiation frequency. Figure 1.1 illustrates the absorption lines in the atmosphere that occur in the microwave spectrum which ranges from 300 MHz to 300 GHz. The downward spikes in the graph correspond to absorption, which in the case of the microwave spectrum is caused by oxygen and water vapour in the troposphere [Luini et al., 2017].

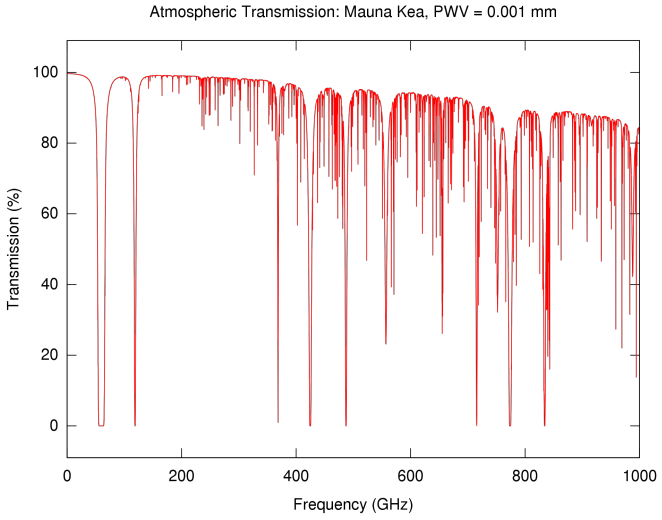

(a) Atmospheric Transmission in the microwave frequency spectrum [Pardo et al., 2001].

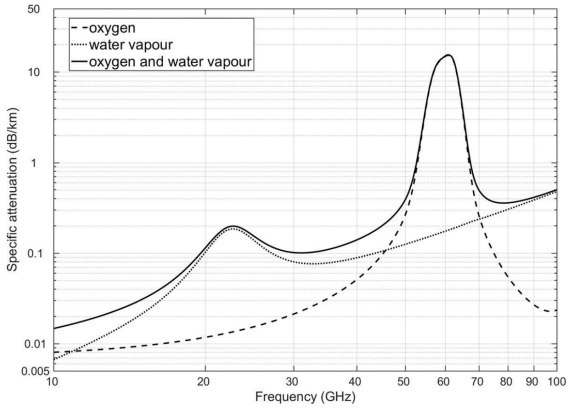

(b) Oxygen (dashed line), water vapour (dotted line) and total gas (solid line) specific attenuation at reference conditions (water vapour density 7.5 g/m3, temperature 15°C, atmospheric pressure 1013 hPa) [Luini et al., 2017].

FIGURE 1.1

There are also some polarisation issues that come with submillimeter wavelengths, that make it difficult to measure the direct polarisation of a source. The most

prominent effect comes from Faraday rotation which occurs due to radiation passing through the ionospheric layers. The radiation in this case can become rotated by several degrees, or several revolutions depending on the layer. This in turn makes it difficult to determine the original polarisation of the source.

1.3 The Big Bang Theory and Cosmic Background Radiation

1.3.1 The Big Bang Theory

The Big Bang Theory is one of the most widely accepted theories of the early Universe. It was the first theorised by Belgian astronomer and mathematician Georges Lemaître, who stated that if the Universe was expanding, there must have been a point in the past where it was much denser than it is now. He referred to this state as the primordial atom. He theorised that at this point (which is now estimated to be 13.8 billion years ago), the Universe underwent a rapid period of expansion now known as inflation. As the Universe expanded, it cooled allowing energy to transform into subatomic particles (e.g protons, electrons and neutrons). It was not until after $\approx 380,000$ years that this plasma of radiation and subatomic particles could cool to 3000 K and form into atoms (hydrogen, helium and deuterium) and allow photons to propagate without scattering. This epoch of the early universe is known as recombination.

1.3.2 Cosmic Background Radiation

Cosmic Background Radiation (CMB) was first theorised in 1948 by Gamow, Alpher and Herman. The key idea came from their α-$\beta\gamma$ paper [Alpher and Herman, 1948], which suggest that the early universe must have been very hot.

In this hot, dense universe before reionisation, the mean free path of photons would have been short enough that the entire universe would be in thermodynamic equilibrium. In an attempt to understand the formation of elements in successive-neutron-capture theory it was found that the Big Bang cosmological model combined with nuclear physics gave an approximate average temperature of 5 K for the earlier universe [Luminet et al., 2003]. This was an early estimation, that would later be reviewed but overall this estimation was a good first attempt at understanding the CMB. Subsequent cosmological studies found that a more likely value of 2.7 K that would prove to be an accurate temperature for the CMB.

The CMB radiation originates from the recombination epoch when light first decoupled from radiation. Before this, the Universe was in a plasma state, photon radiation and baryons being coupled together. Due to the large Thompson scattering cross-section of the electrons, radiation had a much shorter mean free path resulting in an opaque universe and thermal equilibrium. In the early '80s inflation theory was first introduced by Dr. Alan Guth and Andrei Lindle. They theorised that at 10^{-38} seconds after The Big Bang, the Universe expanded rapidly. Inflation predicts an expansion rate of half the speed of light, which would cause ripples in space time compressing and expanding it. These spatial oscillations are more commonly known as gravitational waves. Gravitational waves are unique when compared with EM radiation as they can travel undisturbed through matter. As the Universe expanded, density and temperature decreased until recombination occurred. The Universe became transparent to radiation and atoms were formed. These atoms, under the influence of gravity and the presence of dark matter, would later become the stars and galaxies we now see today.

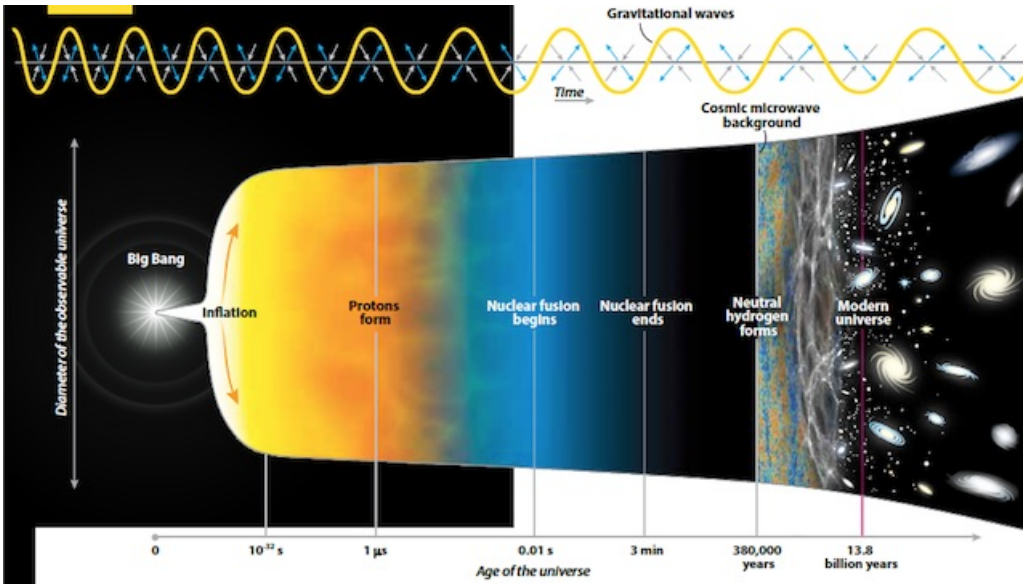

FIGURE 1.2: Inflation took place 10^{-38} seconds after the Big Bang, well before the signal from the CMB. This process dramatically increased the size of the Universe in a short amount of time, both magnifying local density fluctuations and diluting the Universe's temperature structure resulting in the CMB pattern we now observe. Other evidence of inflation is anticipated to come from identification of the gravitational waves produced during inflation, which should have a characteristic B-mode polarisation [Goodwin, 2012]

The first measurement of the CMB was taken by Aron Penzias and R. Wilson at the Bell laboratory in 1964 [Dicke et al., 1965]. The Bell laboratory having the most advanced horn antenna at the time, were trying to investigate radio transmissions from communication satellites. They picked up the signal as noise in their antenna that could not be accounted for. They reported measurements indicating an isotropic "excess antenna temperature" produced by their detection at 4080 MHz.

The first anisotropy found in the CMB was a temperature dipole of (3.5 ± 0.6) mK [Dicke et al., 1965]. This could be attributed to the Doppler effect as a result of the Earths motion relative to the CMB, which makes parts of the CMB appear red shifted and blue shifted with respect to us. It wasn't until November 1989 when NASA launched COBE that much finer anisotropies could be seen and

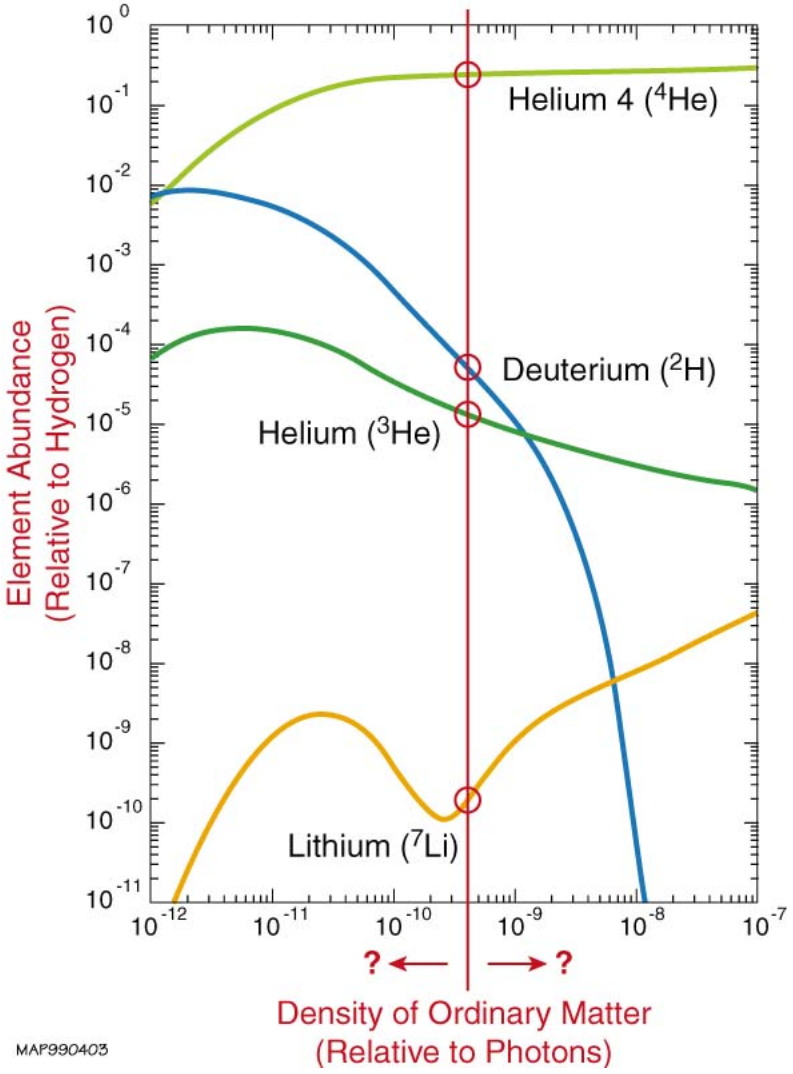

FIGURE 1.3: The abundance of hydrogen relative to the density of ordinary matter [Lepine-Szily et al., 2012].

the first observations were published in 1993. COBE had the ability to measure fluctuations in the CMB to the order of 10^{-5} K [Durrer, 2015].

Since COBE there have been two major CMB space missions undertaken to analyse the anisotropies and spectrum of the background emissions. WMAP (NASA, [Bennett et al., 2013]) and Planck (ESA, [Planck Collaboration et al., 2020]) have both imaged the primordial radiation with greater precision and sensitivity than COBE. The heightened resolution of theses instruments allowed for even smaller temperature fluctuations to be detected. Planck could measure the temperature fluctuations with the cosmic-variance- limited sensitivity down to the angular scale

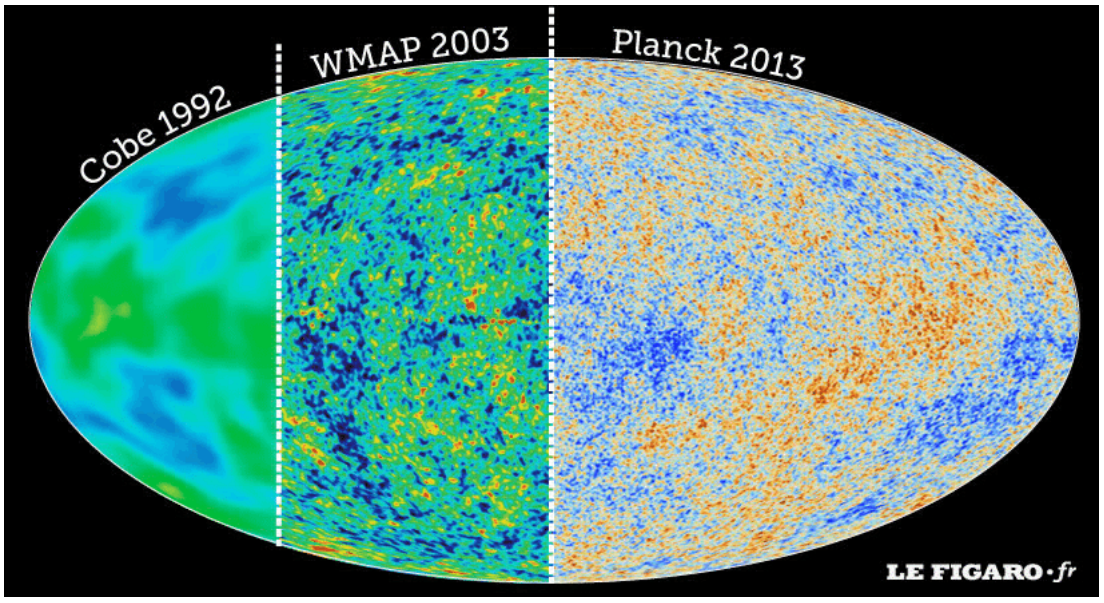

FIGURE 1.4: Satellite images of the CMB temperature variations from Cobe in 1992, WMAP in 2003 and Plank in 2013 [Voplatka, 2014].

of a few arc minutes [Planck, 2009]. As sensitive as Planck was, it wasn't optimised to measure polarisation. The current temperature estimate for the CMB is said to be 2.72548±0.00057 K [Bengaly et al., 2020].

1.3.3 Pertubations (Anisotropies or Temperature Variations)

It is the perturbations or anisotropies in the CMB which are of interest to us because they tell us how the Universe behaved at recombination. Before recombination, Thomson scattering between photons and electrons and the Coulomb interactions between electrons and baryons were sufficiently rapid that the photon-baryon system behaves as a single tightly coupled fluid. As mentioned in the previous section, the Big Bang Theory could account for the general isotropic spectrum of the CMB. However, it does leave some questions unanswered. For example, the Big Bang model does not explain the origin of the structure of the Universe and its constituent stars, galaxies, galaxy clusters and superclusters. The model also

struggles to account for the redshift of the Universe and its apparent expansion. Another important problem is the horizon problem; at the time of decoupling, regions of the CMB that are now separated by more than 2° could have never been in causal contact, meaning they would never be in thermal equilibrium [Guth, 1981]. A more rigorous theory is needed to answer these questions.

The features in Figure 1.4 show the different photon energies at the epoch of last scattering of photons from electrons. The areas coloured in red correspond to the higher temperatures, while the areas in blue correspond to lower temperatures. These temperature fluctuations are believed to be caused by mass inhomogeneities in the early universe. These density fluctuations are believed to be caused by quantum fluctuations during inflation which were then stretched out into cosmic scales over time. These fluctuations in energy density imply fluctuations in the local gravitational potential. Regions of high density generate potential wells. Regions of low density create potential hills. Compression of the photon-baryon fluid occurs in the potential wells and rarefaction occurs in the potential hills. In these wells, the seeds of the structure of the Universe are formed [Khlopov and Rubin, 2004]. As gravity tries to compress the fluid, radiation pressure resists, resulting in acoustic oscillations. Figure 1.5 shows an analogous image using springs as radiation pressure and the inertia of the fluid as spherical masses falling under the presence of gravity.

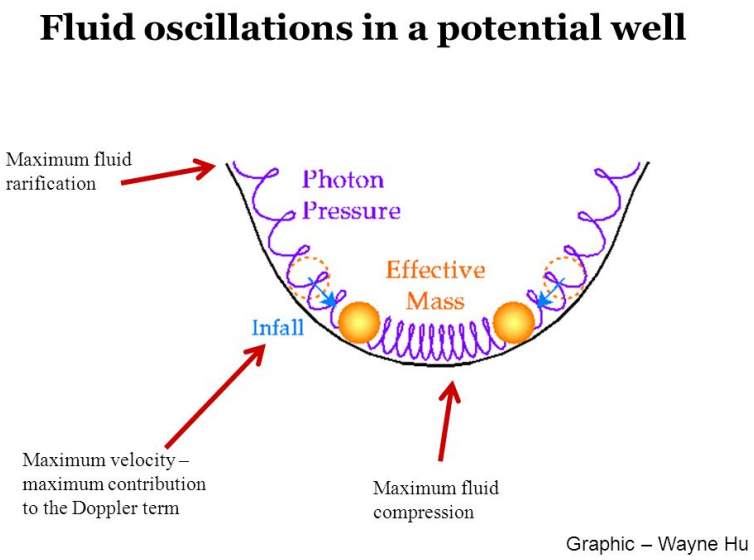

FIGURE 1.5: Analogy of the two competing forces within the photon-baryon fluid. The springs represent the pressure exerted by the photons. The effective masses act as the baryons attracted by the gravitational potential well. [Hu, 1990]

According to inflation, there should be potential oscillations caused by gravity on all scales [Riotto, 2002]. The acoustic oscillations become frozen at recombination when the baryons decoupled from the photons. Modes of oscillation later manifest as temperature fluctuations. These peaks cause spatial variation in the CMB temperature. As time progresses, radiation from more distant regions of the CMB reaches us and can be expressed as an angular scale structure.

Figure 1.6 shows the acoustic peaks in the CMB anisotropy power spectrum at two wavenumbers l (e.g. a multipole). Taking an angular power spectrum of the anisotropies of the CMB gives information about the contents of the Universe. This angular power spectrum corresponds to temperature variations in the sky from one point to another (angular frequency l i.e. $l = 2$ corresponds to two cycles in the fluctuation around the whole sky, while $l = 100$ represents 100 cycles around the sky).

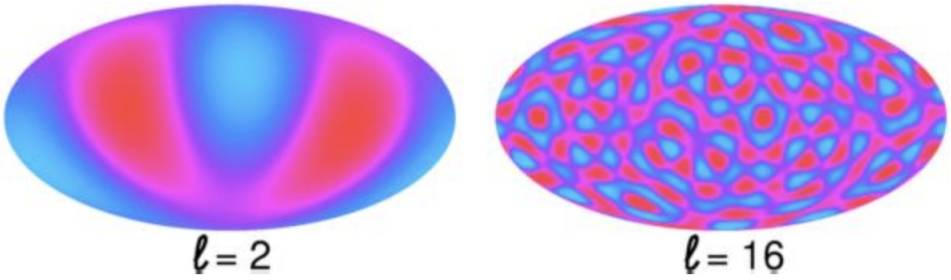

FIGURE 1.6: CMB temperature at at different multipoles, showing anisotropies in the CMB [Kelly].

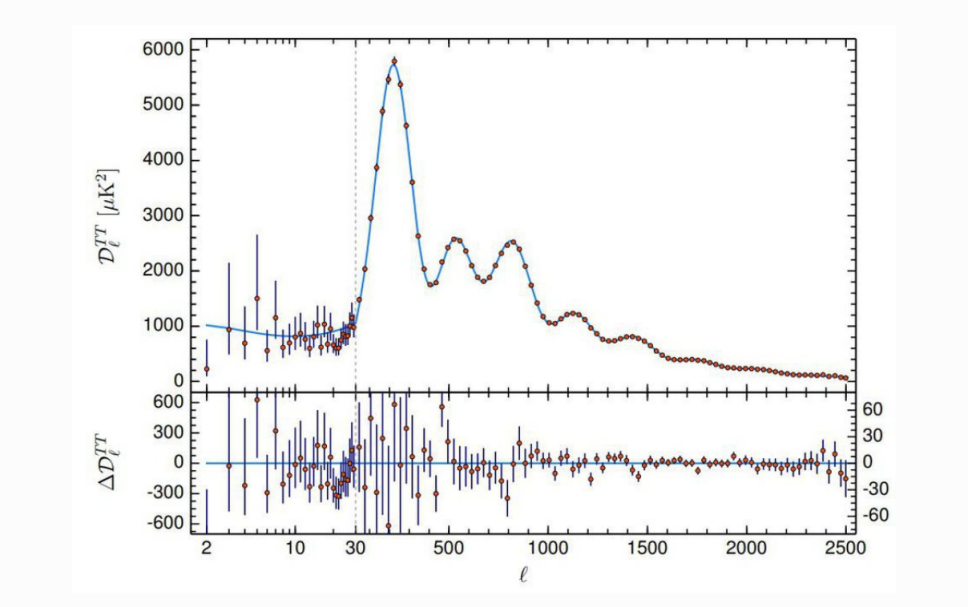

FIGURE 1.7: *Planck* 2018 temperature power spectrum [White et al., 2018]. Note that the vertical scale changes at l = 30, where the horizontal axis switches from logarithmic to linear.

Figure 1.7 above shows the modes of oscillation caught at their extrema during recombination. They form a harmonic series based on the distance sound can travel by recombination, known as the sound horizon [Cuesta et al., 2015]. The first peak represents a mode that compressed inside a potential well before recombination. This tells us about the spatial curvature of the Universe. The first maxima are seen at l=200, which is an indication that the Universe is very close to being spatially flat. This corresponds to a universe where dark matter density and dark energy dominate the energy density of today. The second peak tells us about

the baryon density. The second peak is compressed compared with the first and third peak. A higher density of baryons in a potential well causes an enhanced compression in that well and less rarefaction. Due to symmetrical symmetry, all of the even maxima correspond to compression and all of the odd extrema correspond to rarefaction. The much lower amplitude indicates that there is an excess of dark bayrons. The third peak measures the physical density of the dark matter in the Universe. Raising the dark matter density reduces the overall amplitude of the peaks. Lowering the dark matter density eliminates the baryon loading effect. The most up to date observations for the ΛCDM model in which a flat Universe is dominated by dark energy indicate that dark energy has a total density of 68.3%, dark matter has a density of 26.8% and the ordinary matter has a density of 4.9% [Kelly].

1.3.4 E-mode and B-mode Polarisation

Since 2007 interest has quickly shifted from the temperature varations to the patterns of polarisation in the CMB. Different sources give rise to different polarisation patterns. These patterns are known as E=modes and B-modes. E-modes and B-modes are curl free and divergence free respectively. Figure 1.8 illustrates the difference in polarisation between the two modes.

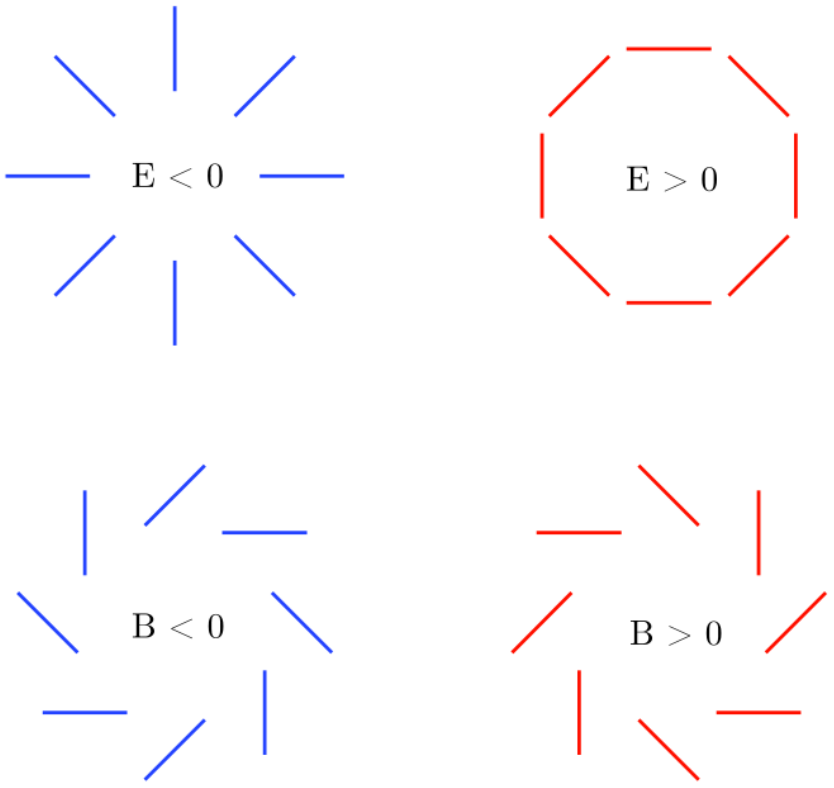

FIGURE 1.8: Diagram depicting E and B mode polarisation [Hanson et al., 2013]

.

Isotropic EM radiation occurs only if incoming radiation from both directions are equal in intensity. In this case, there will be no net polarisation in the outgoing direction. If the intensity of radiation varies at 90°, the distribution has a quadruple pattern. Therefore one will get a net linear polarisation of the outgoing radiation. Figure 1.9 below demonstrates the concept. Photons from different temperature regions meet a temperature inhomogeneity and are converted into an anisotropy. At the end of recombination, this then creates a quadrupole anisotropy which then scatters the radiation into a linear polarisation. These angular variations in the polarisation only occur on small scales. For scales larger than the diffusion length, photons from hot and cold regions of the perturbation do not have a chance to meet before recombination.

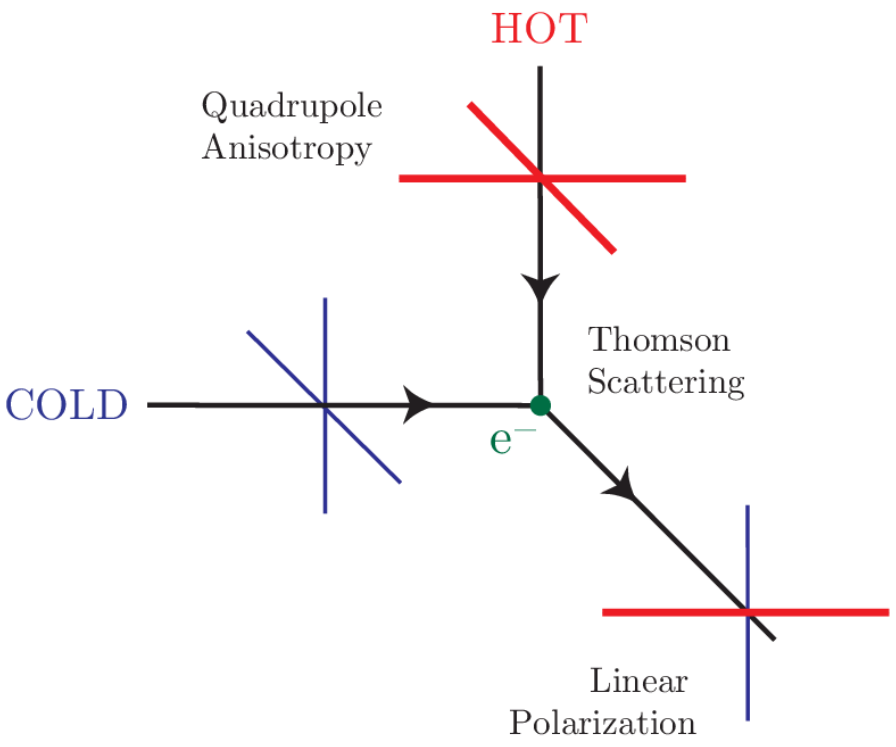

FIGURE 1.9: Quadrupole radiation becoming linearly polarised due to electron Thomson scattering [Duband, 2015].

Perturbations are known as scalar, vector or tensor as follows[Hu and White, 1997]:

:

1. **Scalar** perturbations occur due to instabilities in the gravity potential at last scattering. The modes associated with this type of polarisation are **E-modes** and are generated by Thomson scattering of radiation with quadrapole temperature anisotropy.

2. **Vector** perturbations represent vortical motions in the early Universe. The velocity field v obeys $\nabla v = 0$ and $\nabla \times v \neq 0$. In this case there is no density perturbation and the voricity is damped by the expansion of the Universe as are all motions that are not enhanced by gravity. However, the temperature fluctuations do not decay. A dipole pattern radiation field is produced by bulk motion of the velocity field. Again much like the scalar

field, polarisation is generated via Thomson scattering. This perturbation primarily generates **B-mode** polarisation.

3. **Tensor** perturbations are due to gravitational waves. Due to the stretching of space caused by these gravitational waves, perturbations occur in the plane of the wave. This creates a quadrupole, which generates both **E** and **B modes**.

The two main sources of quadrupole radiation at recombination shown below in Figure 1.10:

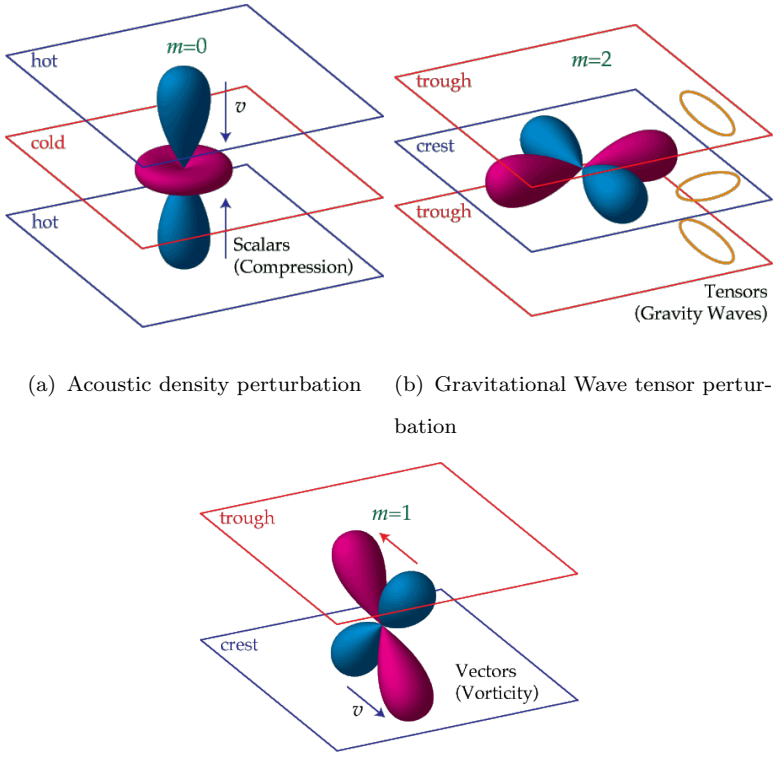

(a) Acoustic density perturbation (b) Gravitational Wave tensor perturbation

(c) Vector (vorticity) perturbation

FIGURE 1.10: Difference between the scalar density perturbations and the tensor gravitational wave perturbations [Hu, 1990].

Figure 1.10(a) describes the density (scalar) perturbations. Here the movement of the photons from hot to cold regions produces a symmetric quadrupole moment. Figure 1.10(b) describes a tensor perturbation caused by gravity. These gravitational waves cause an anisotropic stretching of space. This produces a quadrupole

moment variation in temperature which is not symmetric. This asymmetry causes a "handedness" to the pattern of polarisation. Scalar compression due to acoustic density perturbation is the origin of E-mode polarisation, which is characterised by the polarisation pattern in Figure 1.10. The tensor perturbations caused by gravitational waves generates a crossed polarisation at 45° (Figure 1.10). Vorticity (seen in Figure 1.10(c)) the plasma will create a different type of quadrupole due to the Doppler shift associated with the velocity; vorticity perturbations are predicted to be negligible by recombination [Hu]. One of the main goals of CMB astronomy is to detect primordial polarisations anisotropies.

1.4 3D Printing

1.4.1 3-D Printing and PLA

The Anet A8+ 3-D printer (3D printer used in Chapter 4) uses Fused Deposition Modelling (FDM). 3D printing (also referred to as additive manufacturing) involves the manufacturing of objects via successive addition of PLA layers [Megahed, 2016]. FDM printers have two main mechanisms: the motion system and the extrusion system. The motion system moves the printer to the desired location within the bounds of the printer bed, while the extrusion system lays down the material.

The Anet A8 is designed with three freely moving axes which mimic a Cartesian coordinate system. Stepper motor driven belts and lead screws to transfer the rotary motion into linear motion are used to move each axis (x, y, z). The printer is configured with a Cartesian xz print head, which means the print head can move in the x and z direction, whilst the print bed moves in the y-direction. [Blok et al., 2018]

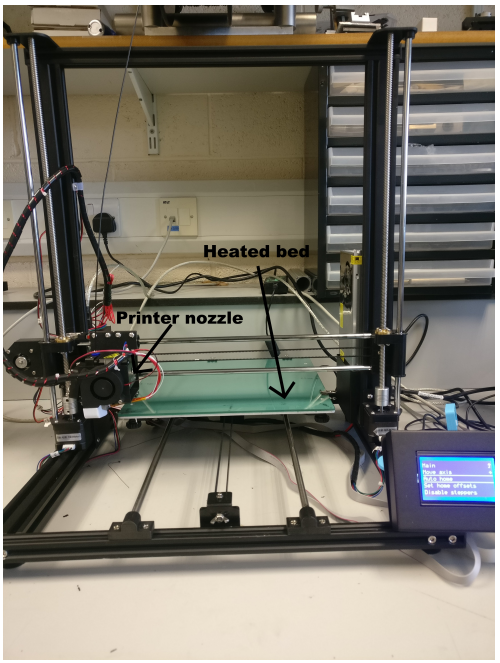

FIGURE 1.11: Anet A8+ 3-D printer, with heated bed and pinhead with xz-axis.

1.4.2 Extrusion System

FDM printers usually use a stepper motor to push the desired PLA through a heated nozzle. The part moving the filament is called the *feeder* while the heated nozzle block is called the *hot-end*. The pushing force into the feeder comes from a driver gear which is fed directly from the stepper motor. The 1.75 mm filament is fed directly into the *hot-end*. Here the filament is heated which is achieved using a heating element monitored using a thermostat. To get the PLA to its desired output diameter, it is pushed through a heated brass nozzle. The nozzle diameter is 0.4 mm.

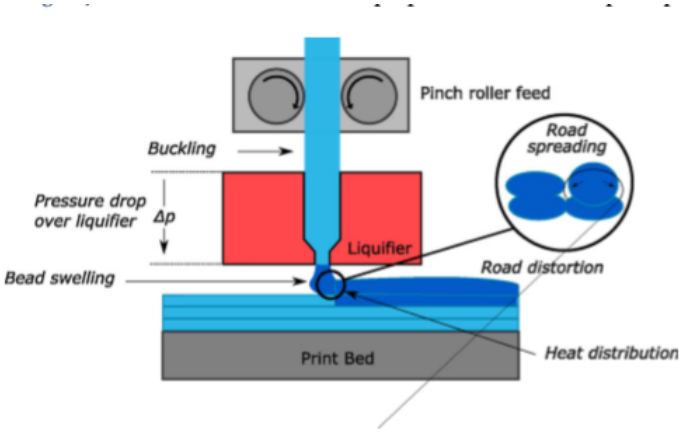

FIGURE 1.12: Anet A8+ 3-D printer's pin-head printer nozzle [Blok et al., 2018].

Once pushed through the nozzle, the first layer is deposited onto the print bed. The print bed is a flat glass surface the object is built on. The print bed is also heated to 200°C to increase adhesion. For additional adhesion, other gluing agents may be used. An 8-bit Arduino controls both the motors and heaters, which could be controlled on the GUI or accessed remotely through the printer's network.

1.4.3 Layering and Meshing

For all 3D modeling, an infill pattern must be chosen to suit the desired application of the object. For example if the object is replacing a metal component, it is best to choose an infill pattern that gives the most structural integrity.

For printing the test infills and lens infills, the default pattern known as the Alternating Raster, [Waterman, 2019] was chosen. Each layer deposits straight lines of parallel filament, with no gaps between the filament. The layer direction then alternates by 90° per layer. This infill uses the most material but offers the highest density and structural integrity. Figure 1.13 shows a number of different infill patterns, all with different structural integrity and attributes.

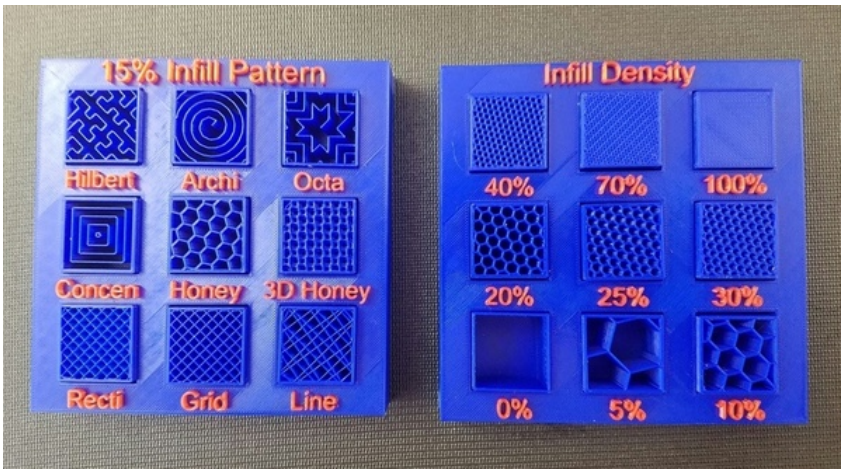

FIGURE 1.13: Different infill patterns used in 3D printing [Vaught].

Infill percentage can also influence the optical properties such as dielectric constant ϵ_r,[Goulas et al., 2019],[Huang et al., 2018] whilst the infill pattern can change the polarisation of an incoming beam.

1.5 S-Parameters

S-parameters are used to describe the magnitude and phase relationship between incident and reflected waves in a port to port system. Here ports refer to wave ports (which are rectangular in the simplest case) and are used to collect and emit radiation. S-parameters are often arranged as a matrix known as a scatter matrix. In order to understand the operation of a scatter matrix, an example from geometrical field optics is given below. In the image below we have a source light bulb transmitting light through a lens and undergoing refraction due to the influence of the lens material. However, some of the light will be reflected back by the lens toward the direction of the light source, which is seen in Figure 1.14.

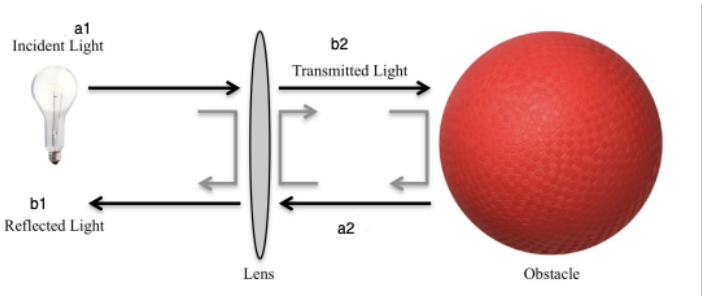

FIGURE 1.14: Optical equivalence of S-parameter behaviour [Duband, 2015].

It is also of interest to see how the light behaves once it has passed through the lens. If an obstacle exists behind the lens part of the transmitted beam will be reflected back towards the light source. Thus, the reflection from the object is added to the initial reflection from the light source. This splits the reflection into two parts: the original beam reflected by the lens and a part of the reflection from the obstacle. This is also the case for the transmitted wave, which consist of the original beam transmitted through the lens and the partially reflected beam from the object, shown in Figure 1.14.

b_1 and b_2 can be described as a combination of both a_1 and a_2, and formally represented as S-parameter equations from a two-port device as shown in Equation 1.1.

$$\begin{aligned} \boldsymbol{b}_1 &= \boldsymbol{S}_{11}\boldsymbol{a}_1 + \boldsymbol{S}_{12}\boldsymbol{a}_2, \\ \boldsymbol{b}_2 &= \boldsymbol{S}_{21}\boldsymbol{a}_1 + \boldsymbol{S}_{22}\boldsymbol{a}_2. \end{aligned} \tag{1.1}$$

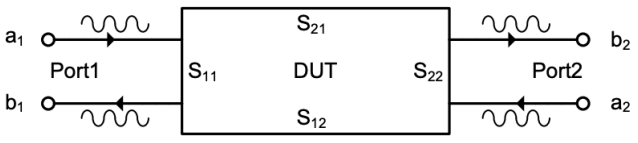

FIGURE 1.15: Two port S-parameter model [National Instruments, 2012]

It is important that the waves leaving the Device Under Test (DUT) ($b_1$or b_2) are a linear combination of the waves entering the lens (a_1 and a_2). From the characteristic impedance of the DUT, the S-parameters can then be extracted. If the impedance of the DUT is 50 ohms and if a 50 ohm termination is present in port 2, a_2 becomes zero, resulting in equation 1.2 for S_{11} and S_{21}. This principle can be applied in the reverse direction too. If a_1 is set to zero, you can obtain equation for S_{22} and S_{21} as seen below in Equation 1.2

$$\begin{aligned} \boldsymbol{S}_{11} &= \left.\frac{\boldsymbol{b}_1}{\boldsymbol{a}_1}\right|_{\boldsymbol{a}_2=0}, \quad \boldsymbol{S}_{12} = \left.\frac{\boldsymbol{b}_1}{\boldsymbol{a}_2}\right|_{\boldsymbol{a}_1=0}, \\ \boldsymbol{S}_{21} &= \left.\frac{\boldsymbol{b}_2}{\boldsymbol{a}_1}\right|_{\boldsymbol{a}_2=\boldsymbol{0}}, \quad \boldsymbol{S}_{22} = \left.\frac{\boldsymbol{b}_2}{\boldsymbol{a}_2}\right|_{\boldsymbol{a}_1=0}. \end{aligned} \tag{1.2}$$

First it must be noted that the S parameters are complex values which carry both magnitude and phase components of the system as a function of frequency. These parameters are usually subscripted S_{mn} to represent the receiver port and subscript n to represent the source port. For example S_{12} is the transmission coefficient for a wave sourced at port 2 and received at port 1. This can be represented in an S matrix for any number of ports n,m.

$$\begin{aligned} \boldsymbol{b} &= \boldsymbol{S} \cdot \boldsymbol{a}, \\ \boldsymbol{S} &= \begin{bmatrix} \boldsymbol{S}_{11} & \dots & \boldsymbol{S}_{1n} \\ \vdots & \ddots & \vdots \\ \boldsymbol{S}_{n1} & \dots & \boldsymbol{S}_{nn} \end{bmatrix}. \end{aligned} \tag{1.3}$$

1.5.1 Standing Wave Filter

To understand how standing waves occur, the S-matrix of a horn-DUT-horn must be considered.

- S_{11} is the reflection from the DUT measured horn 1.

- S_{22} is the reflection from the DUT measured horn 2.
- S_{12} is the transmission from horn 1 to horn 2.
- S_{21} is the transmission from horn 2 to horn 1.

Figure 1.16 below shows a schematic diagram of these coefficients and their corresponding paths.

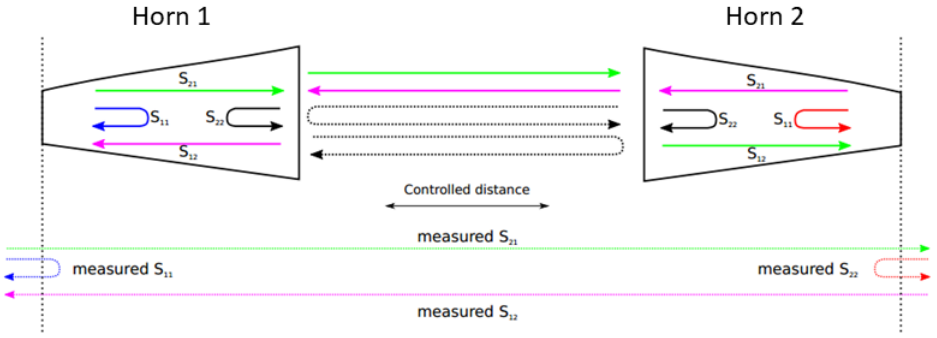

FIGURE 1.16: Schematic diagram of S matrix parameters of a two horn system.

A simulation framework for modelling standing wave modulation of complex measurement data was developed at Maynooth University by Dr Marcin Gradziel to allow standing wave effects to be accurately removed from measured data recorded with the VNA measurement system. It is applicable to a wide class of VNA-based measurement systems consisting of a chain of components (transmitting horn to receiving horn with optical components in between also) where the positioning of individual components can be controlled. This model has been successfully applied to measurement setups with 2 and 3 optical elements between the two ports of the VNA (including the horn antenna effects). This comprehensive model of measurement data, accounting for low-Q standing wave effects, allows individual reflection contributions to be extracted or simply removed reliably (filtered out) in measured data. The model relies on a coherent radiation model where path lengths are well defined initially and with numerical fitting techniques excellent data filtering can

be achieved. This ability allows much better comparison of measured data with simulated data where an accurate comparison is required [Gradziel and Trappe, 2018].

1.6 Thesis Outline

The contents of the thesis will now be outlined by the author, chapter-by-chapter.

1.6.1 Chapter 2

Chapter 2 includes a description of Gaussian Beam Mode analysis and modelling, a key concept of this thesis. To complement this a full description of PO and ray transfer matrices are described by the author, as they are used frequently through this thesis. The analysis software packages *GRASP 10.5* and *CST* are explored in detail due to their use in Chapter 3 and Chapter 4 respectively.

1.6.2 Chapter 3

This chapter introduces the proposed space mission PRISTINE. PRISTINE's main goals are explained by the author in great detail in this chapter. In this chapter the author describes the design process for the pFTS (polarising Fourier Transform Spectrometer), for which the author designed each mirror using *Python* code written using the relevant equations outlined in Chapter 2. Once designed, the mirrors underwent a full EM and PO analysis in *GRASP 10.5* to test the beam quality of a single moded perfect Gaussian source, at 150 GHz, simulated in the aforementioned software. Finally, the resultant EM field cuts were taken by the author along the optical train, plotted and fitted by a perfect Gaussian (fitting

algorithm explained in Section 3.4.1). Once fitted, the beam waist for each cut was found and compared to the waist predicted by the equivalent GBMA.

1.6.3 Chapter 4

In this chapter, the design, manufacturing and analysis of PLA GRIN lenses were described by the author. Chapter 4 describes the experimental setup and procedure undertaken in Maynooth University's VNA laboratory to test the focusing ability of the PLA lenses at W band frequencies. Before any testing was done in the laboratory, full simulations of both lenses were run by the author in *CST*. Cuts of the EM field generated in *CST* were taken by the author and compared to the lab results and the GBM model of the laboratory setup (the exact model used is described by the author in Section 4.4.12). Alongside the analysis of the lenses, some material analysis was performed by the author to determine the relative permittivity of PLA at 100 GHz

1.6.4 Chapter 5

The final chapter of this thesis ventures away from quasioptical analysis, and instead concerns itself with Geophysics. As part of the authors MSc, the author participated in a two-week summer school where he alongside a cohort of international students designed a space mission (MAGMA-C) designed to probe the magnetic field which has been induced in the Earth's mantle by the magnetosphere. The role of the author was to research as part of the science team, to determine the scientific objectives and requirements for the prescribed mission. Included in this chapter are an outline of each component which makes up the overall magnetic field, a brief mathematical description of the science teams goals and objectives, a description of the payload and orbital parameters, the spacecraft design and a short description descoping options and risk analysis.

Chapter 2

Optical Design and Analytical tools for modelling Quasi-optical systems

2.1 Gaussian Beam Analysis

Quasi-optical systems deal with the propagation of relatively well-collimated beams of EM radiation which have relatively large wavelengths when to the compared with the visible spectrum, spanning from the infrared to the submillimeter. When $\lambda \approx$ *system dimensions*, diffraction tends to dominate due to the relative size of the wavelength compared the optical components and a PO approach to analysis is required. If $\lambda \approx 0$ then a ray tracing technique is a reasonable approach to take. The middle ground between PO and geometric optics allows for the use of Gaussian beam modes and Gaussian beam propagation.

When we are dealing with coherent electromagnetic radiation which is diffraction dominated the beam propagates and spreads out (by definition) in the direction traverse to propagation. When taking a ray tracing approach the beam is always

said to be a plane wave, however when this is not the case the beam is said to have a characteristic profile. This regime is often referred to as paraxial beam propagation. In this approach the propagating wave is represented as a transverse component of an EM field:

$$E = \sum_n A_n \Psi, \tag{2.1}$$

where Ψ represents the complex independently propagating modes, each with a transverse amplitude distribution

This approach was first surmised in the '60s by [Fox and Li, 1961] to model masers interacting with two paraxial mirrors. The effects of repeated diffraction were relatively unknown at the time and more work and modelling needed to be done. A laser can be modelled as a Gaussian distribution, with a wide variety of modes depending on the different laser mirror dimensions.

2.1.1 Gaussian Beam Mode Propagation

Once EM waves become incident on an optical component they are no longer considered to have a plane wave form. Instead, due to diffraction they can be modelled as Gaussian beam modes. When deriving Gaussian beam mode theory the following assumptions were made:

• The radiation is treated as a paraxial beam, whose beam width is not large enough to be treated as plane wave.
•The radiation can be treated as a scalar field distribution.

Thus, now we can develop the paraxial wave equation using the Helmholtz equation [Samarskii et al., 1993]:

$$(\nabla^2 + k^2)\psi = 0, \tag{2.2}$$

where ψ represents any component of the **E** or **H** field. In rectangular coordinates the paraxial equation is

$$\frac{\partial^2 u}{\partial^2 x} + \frac{\partial^2 u}{\partial^2 y}\partial z - 2jk\frac{\partial u}{\partial z} = 0. \tag{2.3}$$

u in this case represents a complex scalar function. Solutions to this equation can also be obtained in the cylindrical coordinate system. In this coordinate system, r represents the perpendicular distance from the axial ray of propagation and the angular coordinate is represented by ϕ. The paraxial equation looks a little different in this case (the equation below assumes axial symmetry,and that u is independent of ϕ).

$$\frac{\partial^2 u}{\partial^2 r} + \frac{1}{r}\frac{\partial^2 u}{\partial^2 r} - 2jk\frac{\partial u}{\partial z} = 0, \tag{2.4}$$

where $u = u(r, \phi\, z)$

From [Goldsmith, 1998, p 11] the solution to this equation can be taken as

$$u(r, z) = A(z)\exp[\frac{-jkr^2}{2q(z)}], \tag{2.5}$$

A and q are the complex functions (of z only). The distribution looks Gaussian in form. Subbing Equation 2.5 into 2.4 two relationships are formed. Namely,

$$\frac{\partial q}{\partial z} = 1, \tag{2.6}$$

and

$$\frac{\partial A}{\partial z} = -\frac{A}{q}, \tag{2.7}$$

2.6 has the solution

$$q(z) = q(z)_0 + (z - z_0). \tag{2.8}$$

A solution with a Gaussian distribution (see [Goldsmith, 1998] for full derivation) can be found.

$$f(r) = f(0) \exp^{-(\frac{r}{r_0})^2}, \tag{2.9}$$

where r_0 represents the distance to the $\frac{1}{e}$ point relative to the on-axis values of amplitude.

Its follows from [Goldsmith, 1998] that an equation to describe the radius of curvature R and a newly defined term known as the beam radius ω can be used.

$$R = z + \frac{1}{z}(\frac{\pi w_0^2}{\lambda})^2, \tag{2.10}$$

$$\omega = \omega_0[1 + (\frac{\lambda z}{\pi \omega_0^2})]^{0.5}, \tag{2.11}$$

where z is the on-axis distance, ω_0 is the beam waist radius at $z = 0$. The beam waist radius is the minimum value of the beam width which occurs when the radius of curvature is infinite and this gives it plane wave characteristics. The transverse spreading Gaussian wave requires a lower amplitude as it propagates and diffracts as shown in Figure 2.1 b). In contrast, the radius of curvature is infinity at the beam waist and then becomes smaller and as the wave spreads out before increasing again. A schematic representation of R can be seen in Figure 2.1 also.

Finally to obtain the phase slippage of the beam we must use Equation 2.7, which we rewrite as

$$\frac{dA}{A} = \frac{-dz}{q}, \tag{2.12}$$

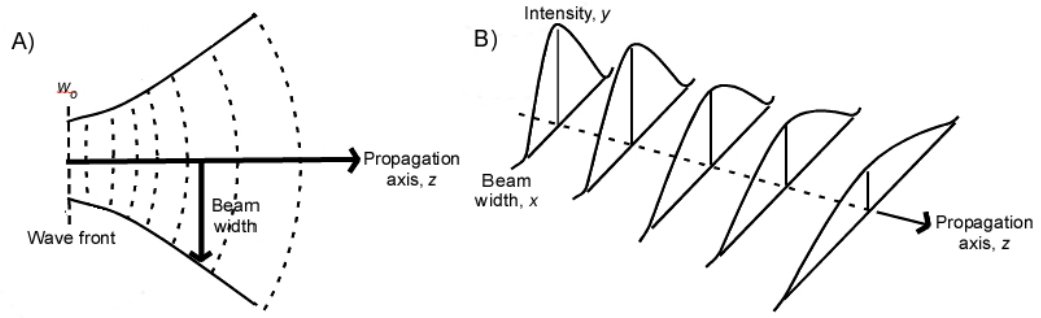

FIGURE 2.1: a) represents the change in radius of curvature R and b) shows the change in beam waist due to propagation [Goldsmith, 1998, p 14]

and from Equation 2.6 can be written as $dz = dq$

$$\therefore \frac{dA}{A} = -\frac{dq}{q}, \tag{2.13}$$

and subbing in for q the equation becomes

$$\frac{A(z)}{A(0)} = \frac{1 + \frac{j\lambda z}{\pi\omega_0^2}}{1 + (\frac{\lambda z}{\pi\omega_0^2})^2}. \tag{2.14}$$

This equation can now be expressed in terms of a phasor

$$\tan(\phi)_0 = \frac{\lambda z}{\pi\omega_0}, \tag{2.15}$$

so that $\frac{A(z)}{A(0)} = \frac{\omega_0}{\omega} \exp j\phi_0$.

Solving for ϕ_0, any phase difference after a wave has propagated can be estimated. ϕ_0 is known as the Gaussian beam phase shift.

2.1.2 Higher Order Modes (Cylindrical Coordinates)

A Gaussian beam profile is the simplest solution to the paraxial wave equation. For most cases, this will suffice, however for more complex systems, a more complex field distribution is required. For this higher order beam mode solutions are

needed. These higher order modes are characterised by the beam radius ω(z), the radius of curvature *R(z)* and an additional phase slippage term. In cylindrical coordinates, Gaussian-Laguerre modes define the beam modes e.g,[O'Sullivan and Murphy, 2012]:

$$\begin{aligned}\Psi_{pm}(r,\phi,z) = &\left[\frac{2p!}{\pi(p+m)!}\right]^{0.5}\frac{1}{w(z)}\left[\frac{\sqrt{r}}{w(z)}\right]^{m}L_p^m\left(\frac{2r^2}{w^2(z)}\right)\\ &\cdot\exp\left[\frac{-r^2}{w^2(z)}\right]\exp[-jkz]\exp\left[-j\frac{\pi r^2}{\lambda R(z)}\right]\\ &\cdot\exp\left[-j(2p+m+1)\phi_0(z)\right]\exp(jm\phi),\end{aligned} \tag{2.16}$$

where L_p^m are the generalised Lauguerre polynomials. The phase slippage term is now defined by Equation 2.17:

$$\phi(z) = (2p+m+1)\phi_0(z). \tag{2.17}$$

$\phi_0(z)$ is the phase slippage of the fundamental mode, m azimuthal order number, p is the radial mode number.

The Gaussian-Laguerre modes are orthonormal sets of modes which are solutions to the paraxial wave equation in a cylindrical coordinate system. Depending on the symmetry of the system, any solution to the wave equation can be expressed in terms of a summation of the Gaussian modes, for the particular mode set Ψ_i, such that E can be represented by Equation 2.18 [O'Sullivan and Murphy, 2012]

$$E(r) = E(x,y,z) = \Sigma_i A_i \Psi_i(x,y,z;w(z),R(z),\phi_i(z)), \tag{2.18}$$

where $E(r)$ is the field, A_i are the mode coefficients, $\omega(z)$, *R(z)*, and the $\phi_i(z)$ are the usually variables defined above. If the beam coefficients A_i are known, the beam can be recreated at any plane in the optical system. If E is integrated

over the surface S, then the mode coefficients can be calculated using the overlap integrals.

$$A_i = \iint_S E(x, y, z) \cdot \Psi_i^*(x, y, z; w(z), R(z), 0) ds. \tag{2.19}$$

A beam can be characterised using beam parameters in orthogonal directions x and y represented by the beam radius ω_x and ω_y. These variables will be used later to define ellipticity.

The beam parameters can be written as two independent functions as follows

$$\frac{1}{q_x} = \frac{1}{R_x} - \frac{j\lambda}{\pi\omega_x^2}, \tag{2.20}$$

and

$$\frac{1}{q_y} = \frac{1}{R_y} - \frac{j\lambda}{\pi\omega_y^2}. \tag{2.21}$$

In terms of x and y the beam parameters then become [Goldsmith, 1998]

$$R_x = z + \frac{1}{z}(\frac{\pi\omega_{0x}^2}{\lambda})^2, \tag{2.22}$$

$$R_y = z + \frac{1}{z}(\frac{\pi\omega_{0y}^2}{\lambda})^2, \tag{2.23}$$

$$\omega_x = \omega_{0x}[1 + (\frac{\lambda z}{\pi\omega_{0x}^2})]^{0.5}, \tag{2.24}$$

$$\omega_y = \omega_{0y}[1 + (\frac{\lambda z}{\pi\omega_{0y}^2})]^{0.5}. \tag{2.25}$$

2.1.3 Confocal Distance

The confocal distance (or Rayleigh range) z_c of a Gaussian beam of waist radius ω_0 is defined as [Goldsmith, 1998, p 22-23]

$$z_c = \frac{\pi\omega_0^2}{\lambda}. \tag{2.26}$$

A Gaussian beam is considered quasi colliamted (ω has not increased by a factor of $\sqrt{2}$) within a distance z_c of the waist (Figure 2.2). So z_c represents a quasi-optical depth of focus. Using this definition for the confocal distance, the Gaussian beam parameters can now be written in terms of z_c:

$$\begin{aligned} w(z) &= w_0\left[1+\left(\tfrac{z}{z_c}\right)\right]^{1/2}, \\ R(z) &= z + \tfrac{z_c^2}{z}, \\ \phi_0(z) &= \tan^{-1}\left(\tfrac{z}{z_c}\right). \end{aligned} \tag{2.27}$$

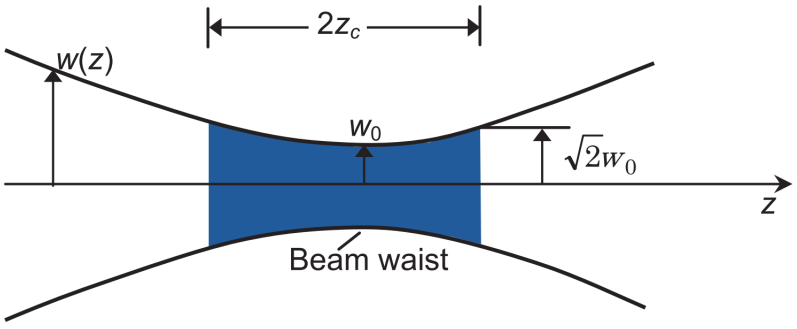

FIGURE 2.2: Confocal distance of well collimated beam [O'Sullivan and Murphy, 2012].

2.2 ABCD Matricies

In classical geometrical optics, a convenient way of representing the propagation of a beam is in matrix form. If we consider a beam propagating in free space, upon reflection or refraction from a surface, the beam will change its position and angle. The beam at the input plane can be described in terms of position y_0 and angle u_0. This position and angle will be operated on due to the interaction outlined.

This interaction can be characterised by a 2×2 matrix

$$\begin{bmatrix} y_1 \\ u_1 \end{bmatrix} = \begin{bmatrix} A & B \\ C & D \end{bmatrix} \begin{bmatrix} y_0 \\ u_0 \end{bmatrix}$$

.

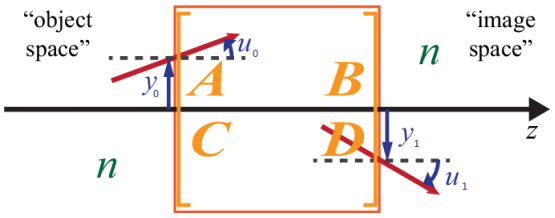

FIGURE 2.3: Representation of a beam propagation through a system, which is defined as an ABCD matrix. [Choi and Howell, 2014]

Now let's consider radiation emanating from a point source. If we have an input plane and an output plane, each perpendicular to the optical axis of the system, we can define the propagation using these reference planes. The radiation crosses the input plane at y_0 with an angle of u_0 from the optical axis. This ray will then propagate through some optical system (represented by the ABCD matrix) and eventually through to the output plane at (y_1, u_1).

$$A = \frac{y_1}{y_0}, B = \frac{y_1}{u_0}, C = \frac{u_0}{y_1}, D = \frac{u_1}{u_0}. \tag{2.28}$$

We can then take R_{in} to be the distance the beam travels from the source to the input plane $\frac{y_0}{u_0}$ and R_0 to be the distance from output plane to the new image plane $\frac{y_1}{u_1}$ [Trappe, 2002]. The desired output radius R_{out} can therefore be written as

$$R_{out} = \frac{AR_{in} + B}{CR_{in} + D}. \tag{2.29}$$

The above is for the paraxial case, but for a paraxial Gaussian beam, the R parameter is replaced by the complex beam parameter given in Equation 2.30

$$q_{out} = \frac{Aq_{in} + B}{Cq_{in} + D}, \tag{2.30}$$

where q is defined as the complex solution as [Goldsmith, 1998]

$$\frac{1}{q} = (\frac{1}{R}) + j(\frac{\lambda}{\pi\Phi(z)}). \tag{2.31}$$

If Equation 2.29 is subbed into Equation 2.31 and evaluated for the real part the equation becomes

$$\frac{1}{R_{out}} = \frac{C + \frac{D}{R_{in}} - \frac{jD\lambda}{\pi\Omega_{in}^2}}{A + \frac{B}{R_{in} - \frac{jB\lambda}{\pi\Omega_{in}^2}}}, \tag{2.32}$$

$$\omega_{out} = \frac{-\lambda}{\frac{C + \frac{D}{R_{in}} - \frac{jD\lambda}{\pi\Omega_{in}^2}}{A + \frac{B}{R_{in} - \frac{jB\lambda}{\pi\Omega_{in}^2}}}}. \tag{2.33}$$

It is convention to consider the beam as travelling from left to right, where each individual optical component has it own ABCD matrix. The overall ABCD matrix is found by multiplying each individual matrix in reverse order. Figure 2.4 shows each of the matrices for some relevant optical operations.

2.3 Commonly Used ABCD Matricies

Table 1. Ray Matrices for Various Simple Optical Elements[a]

Structure	Diagram	Matrix
Straight section (length L)	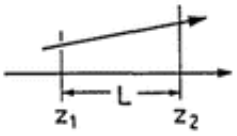	$\begin{bmatrix} 1 & L \\ 0 & 1 \end{bmatrix}$
Thin lens [focal length f: ($f > 0$, converging; $f < 0$, diverging)]		$\begin{bmatrix} 1 & 0 \\ -1/f & 1 \end{bmatrix}$
Flat dielectric interface (refractive indices n_1, n_2)	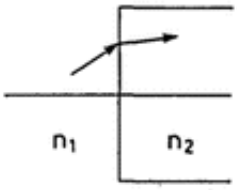	$\begin{bmatrix} 1 & 0 \\ 0 & n_1/n_2 \end{bmatrix}$
Curved dielectric interface (radius R)	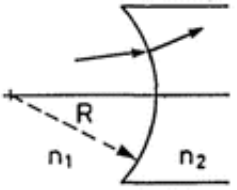	$\begin{bmatrix} 1 & 0 \\ \frac{n_2 - n_1}{n_2 R} & \frac{n_1}{n_2} \end{bmatrix}$
Curved mirror (radius of curvature R)	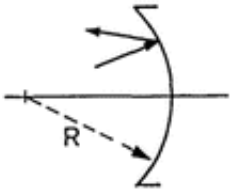	$\begin{bmatrix} 1 & 0 \\ -2/R & 1 \end{bmatrix}$
Thin lens (focal length f followed by a distance L)	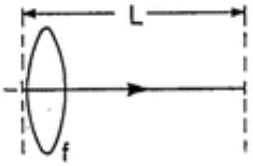	$\begin{bmatrix} 1 - \frac{L}{f} & L \\ -\frac{1}{f} & 1 \end{bmatrix}$

FIGURE 2.4: Table of ABCD matrices for a) free space, b) thin lens, c) dielectric, d) curved dielectric, e) curved mirror and f) thin lens [Hanson et al., 2016].

Figure 2.4 shows some of the most commonly used matrices in optical set ups. As the section suggests, the most commonly used matrices in this Thesis shall be discussed in detail. All of the equations used in in this section are from [Goldsmith, 1998, p 43-50]

2.3.1 Uniform Medium

The most simplistic case of an ABCD matrix is for propagation through a medium of homogeneous refractive index. Free space can be a simple example in this case. A ray with initial off-axis position of r_{in} and slope r'_{in} that is achieved, after propagating a distance of L, will have the same slope but a different off-axis distance equivalent to r'_{in}. From this we can find r_{out} and r'_{in}, making use of the small angle approximation

$$r_{out} = r_{in} + Lr'_{in}r'_{out} = r'_{in}, \tag{2.34}$$

which leads us to corresponding matrix in 2.4

$$\begin{pmatrix} 1 & L \\ 0 & 1 \end{pmatrix}. \tag{2.35}$$

2.3.2 Curved Surfaces

Another important matrix to study is that for the interaction of of a ray with a curved surface between media of two different refraction indexes n_1 and n_2:

$$M_{curved} = \begin{pmatrix} 1 & 0 \\ \frac{n_2 - n_1}{n_2 R} & \frac{n_1}{n_2} \end{pmatrix}. \tag{2.36}$$

If $R < 0$ the surface is considered to be concave to the left and if $R = \infty$ the surface is a plane.

2.3.3 Thin Lens

In geometric terms a thin lens occurs at the intersection of two curved lines with a certain radius of curvature R and thickness. In the case of a thin lens the thickness is assumed negligible. If the lens has a refractive index n_2 and is embedded in air n_1, the thin lens matrix can be calculated by multiplying both curved surface matrices from Equation 2.36.

$$M_{ThinLens} = \begin{pmatrix} 1 & 0 \\ \frac{n_2-n_1}{n_2R} & \frac{n_1}{n_2} \end{pmatrix} \begin{pmatrix} 1 & 0 \\ \frac{n_2-n_1}{n_2R} & \frac{n_1}{n_2} \end{pmatrix} = \begin{pmatrix} 1 & 0 \\ \frac{n_2-n_1}{n_1}(\frac{1}{R_2} - \frac{1}{R_1}) & \frac{n_1}{n_2} \end{pmatrix}. \tag{2.37}$$

Subbing the Lens Makers equation into 2.37 the matrix becomes:

$$\begin{pmatrix} 1 & 0 \\ -\frac{1}{f} & 1 \end{pmatrix}. \tag{2.38}$$

2.3.4 Thick Lens

Much like a thin lens, a thick lens makes use of Equation 2.36, the only difference being the lateral axial thickness d is taken into account. After the ray propagates through the first curve, it encounters a medium n_2 of thickness d and then exits at the curved surface of interface two. The appropriate matrix now needs an extra transfer matrix to describe the path the ray takes through the lens.

$$M_{ThinLens} = \begin{pmatrix} 1 & 0 \\ \frac{n_2-n_1}{n2R} & \frac{n_1}{n_2} \end{pmatrix} \begin{pmatrix} 1 & d \\ 0 & 1 \end{pmatrix} \begin{pmatrix} 1 & 0 \\ \frac{n_2-n_1}{n2R} & \frac{n_1}{n_2} \end{pmatrix} = \begin{pmatrix} 1 & 0 \\ \frac{n_2-n_1}{n1}(\frac{1}{R_2} - \frac{1}{R_1}) & 1 \end{pmatrix}. \tag{2.39}$$

2.3.5 Elliptical and Spherical Mirrors

It is useful to use mirrors to focus beams, even though they arrive with distortions under certain conditions, with fast focal ratios or off-axis configurations. Since mirrors have the same properties as a thin lens, their matrix can be approximated by using Equation 2.37. Here $2/R$ is substituted in for f.

$$\begin{pmatrix} 1 & 0 \\ -\frac{1}{f} & 1 \end{pmatrix} = \begin{pmatrix} 1 & 0 \\ -\frac{2}{R} & 1 \end{pmatrix}. \tag{2.40}$$

2.4 Gaussian Beam Telescopes

A Gaussian beam telescope is defined as a pair of focusing elements separated by the sum of their focal lengths. From [Goldsmith, 1998, p. 53] the output beam waist w_0 :

$$\omega_{0out} = \frac{f_2}{f_1}\omega_{0in}, \tag{2.41}$$

is independent of the λ and d_{in}. This is a very useful characteristic, which will later be used to design optical systems in this thesis. The magnification is therefore given by

$$M = \frac{f_2}{f_1}, \tag{2.42}$$

d_{out} does however depend on d_{in}

$$d_{out} = \frac{f_2}{f_1}(f_1 + f_2 - \frac{f_2}{f_1}d_{in}), \tag{2.43}$$

and must be equal to f_2 for $d_{in} = f_1$. This means the output beam waist is also independent of wavelength.

2.5 GRASP 10.5

2.5.1 Introduction

GRASP *10.5* predicts the electromagnetic (EM) radiation patterns of reflector telescopes by calculating the field from a source such as a horn, then propagating this through a reflector system to a detection plane in the near field or far field of the telescope. By using PO and PTD (Physical Theory of Diffraction), a full vector optical analysis of the system, such as PRISTINE, can be achieved. It is essential to understand what is meant by PO and PTD. PO calculates the EM fields induced on a surface. PTD deals with the interaction of EM fields at the edges of components e.g., edge diffraction [Ufimtsev, 2014].

GRASP 10.5 uses two main object classes: *geometric objects* (GO) and *electrical objects* (EO). GO are the physical objects used to guide the radiation to its required destination. Within these classes there are objects such as scatters, surfaces and rims. To position these objects in 3-D space there is also a *coordinate system*. The EO class contains all the objects required to store and analyse EM field information. These objects include but are not limited to *Frequency*, *Feeds* (such as horns), *PO analysis* and *Field Storage*.

2.5.2 Geometrical Objects

A full description of the main objects used in this thesis will be described in this section.

2.5.2.1 Surfaces

GRASP 10.5 offers a whole array of different surface definitions to suit the user's preference.

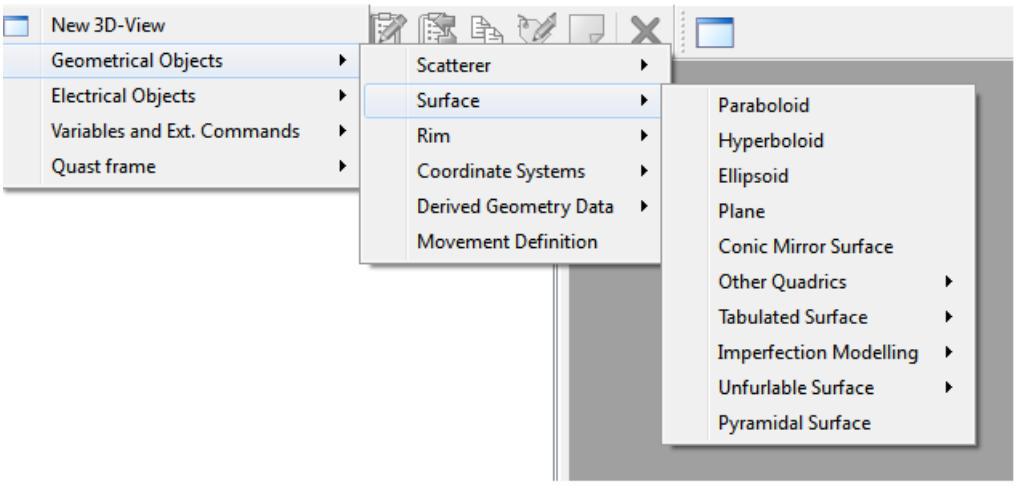

FIGURE 2.5: Different option available to define a desired surface for a scatterer.

Equation 2.5 shows the multiple surface options available for the user to define. In particular the *Second Order Polynomial* was used to define conic mirror surfaces. In *GRASP 10.5* a 2nd order equation is defined using Equation 2.44

$$A_{xx}x^2 + A_{xy}xy + A_{yy}y^2 + A_x x + A_y y + A_c = A_{zz}z^2 + A_z z + A_{xz}xz + A_{yz}yz. \quad (2.44)$$

Figure 2.44 can generate any kind of quadratic surface, such as the common reflector surfaces : parabolic, hyperbolic and ellipsoid which are defined below

$$a\ flat\ surface, z = ax + cy + c, \quad (2.45)$$

$$a\ circular\ cone, z^2 = a(x^2 + y^2), \quad (2.46)$$

$$a\ circular\ cylinder, z^2 = r^2 - y^2, \quad (2.47)$$

$$a\ sperical\ reflector, z^2 = r^2 - x^2 - y^2. \quad (2.48)$$

If the shape is one of the classic conics, which is the case for this thesis the ellipsoidal equation can be used

$$z = \frac{x^2}{4f_x} + \frac{y^2}{4f_y}. \tag{2.49}$$

To create a polynomial equation for a ellipsoidal, the appropriate coefficients must be found as shown in Figure 2.6

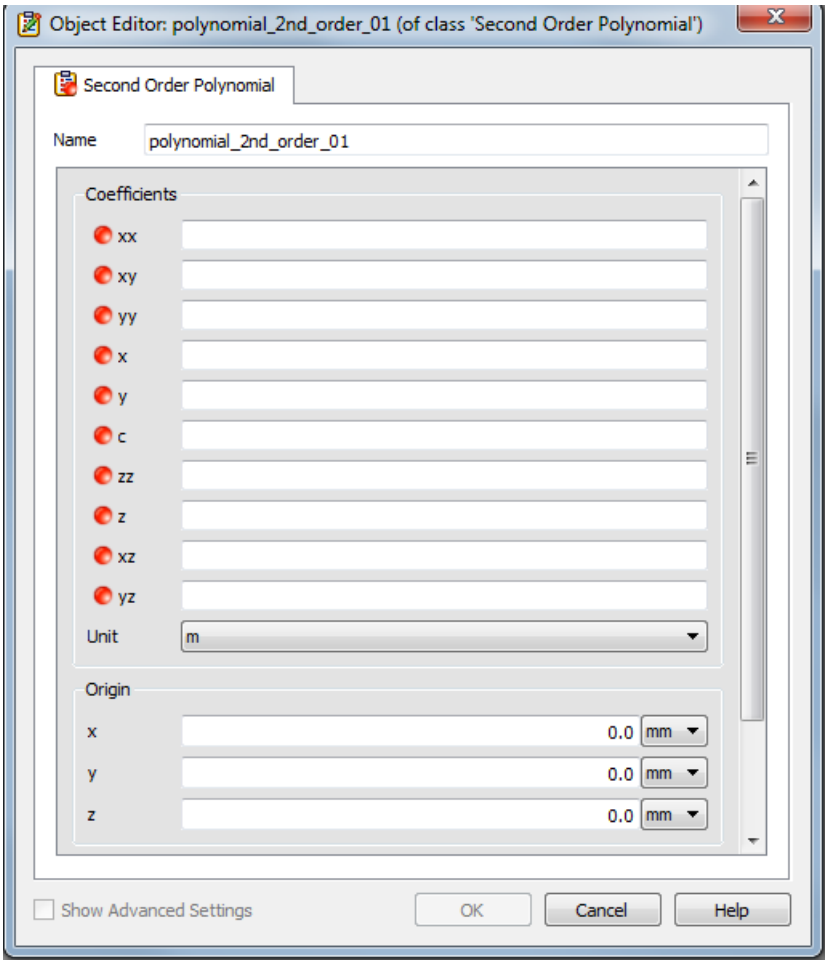

FIGURE 2.6: 2^{nd} Order polynomial surface coeifficients class in *GRASP*

The *Second Order Polynomial* class always defines the source as propagating from the focus f_1 towards a reflector (defined as a section of the surface using the *rim* class), then focusing towards the other focus point f_2 after the surface. So the initial conditions required to calculate the required coefficients are f_1, f_2 and the

angle of throw θ_0. The angle of throw is defined as $2\theta_i$, where θ_i is the angle of incidence of the beam.

Name	Symbol	Equation
Semi-major axis	a	$\frac{R1+R2}{2}$
Semi-minor axis	b	$\sqrt{R1R2\cos\theta}$
Ellipticity	ϵ	$\sqrt{1+\frac{a^2}{b^2}}$
Radius Of Curvature	Rad	$a(1-\epsilon^2)$
Conic Constant	C	$-\epsilon^2$

TABLE 2.1: Ellipse variables

To determine the requirements for the 2^{nd} order polynomial class in *GRASP 10.5* a piece of *PYTHON* code was written which takes the following user inputs; R1 the distance from the source to the reflector, θ_0 the angle of reflection of the beam and R2 the distance from the reflector to the focus. From these inputs all of the variables from Table 2.1 were used to calculate the variables from Figure 2.6 . The code was designed to output all of the parameters needed to describe an elliptical surface in *GRASP10.5* (seen in Figure 2.7) .

1. **Focus distance**: Distance between the focii f_1 and f_2 of the ellipse.
2. **Major Axis**: a (the major axis of the ellipse).
3. **Poly**: Surface polynomial equation.
4. **Vertex Coordinates without intercept parameters**: These are the vertex location of the ellipse in an undefined coordinate system.
5. **Origin x-point**: This is the transformation variable needed to transform the x coordinate of the f_1 onto the vertex of the ellipse.

6. **Origin z-point**: This is the transformation variable needed to transform the z coordinate of the f_1 onto the vertex of the ellipse (+ the z position of the reflector coordinate system).

7. **Axis Angle**: This determines the rotation of the ellipse axis, which will give the user-defined angle of throw to the surface.

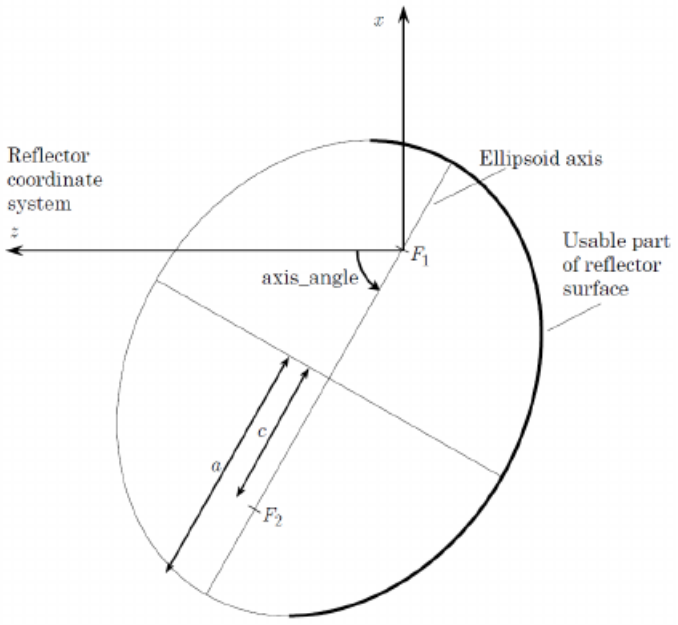

FIGURE 2.7: Sketch of Ellipsoid [TRICA, 2015].

For example if the user wanted to focus a collimated source to a collector horn 100 mm from the mirror with an angle of throw 90°, the parameters illustrated in Figure 2.8, polynomial coefficients, position of the ellipse origin and ellipse rotation would be outputted. Finally when the user inputs these values into *Grasp 10.5*, the setup illustrated in Figure 2.8 is obtained.

2.5.2.2 Rims

Once the surface has been defined, the section of the surface which is required by the user must be defined. To do this the *Rim* class must be defined. This class can be specified through the reflector object. Through the course of this thesis only

(a) Ray diagram imaged on GRASP textit10.5 of the beam described above.

```
Focii distance =  2500000000.000002
Major Axis       =  2500000100.0

The distance between the foci and the vertex =   50.00

Poly: 0.0050000001912098605 x^2 + 0.0050000001912098605 y^2 + 3.999999840000006e-10 z^2

Vertex Coordinates w/o Intercept parameter: ( 49.99999905934665 , 0.0 )

Origin x-point = 50.0 Origin z-point= -100.0

Rotation value is  ('r1<r2', 90.0)
```

(b) Output from *Second Order Class*

FIGURE 2.8: Example of the *Second Order Class* used to define a reflector positioned 100 mm from a source and reflected 90°. The reflector's input values are : $f_1 = 100$ mm, $f_2 = 25$ km, *angle of throw* $= 90°$ and the mirror is positioned 100 mm from the source.

elliptical rims were used. The user must define the ellipse centre (x_c, y_c) (default is (0,0)) and the half axes lengths (a and b).

$$(\frac{x - x_c}{a}) + (\frac{y - y_c}{b}) = 1. \tag{2.50}$$

2.5.3 Electrical Objects

In *GRASP 10.5*, Electrical Objects (EOs) are a class of objects that define and analyse the EM radiation propagating through the system.

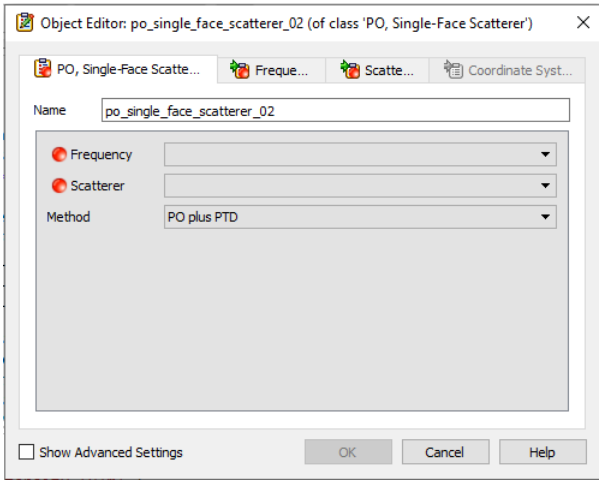

FIGURE 2.9: Image of the required user inputs to create PO class

2.5.3.1 PO (Physical Optics)

In the PO class, the user defines how the PO and PTD currents shall be calculated on a specific reflector. The currents originate in the form of a field from a predefined source and the newly calculated field values are saved as the new user defined PO analysis. These currents can serve as a source for later calculations either for determining a field or new induced currents on another scatter.

2.5.3.2 Feed

Simple and general sources, as well as pattern descriptions are described in the Feed menu. Different feeds are required to illuminate the reflector in question, but for the purpose of this thesis only the *Gaussian Beam, Near Field Def* was used. This class defines a feed which radiates a Gaussian beam using near-field parameters of the Gaussian beam. The class requires the user to input the Gaussian beam waist, phase front radius, polarisation and frequency which can be seen in Figure 2.10.

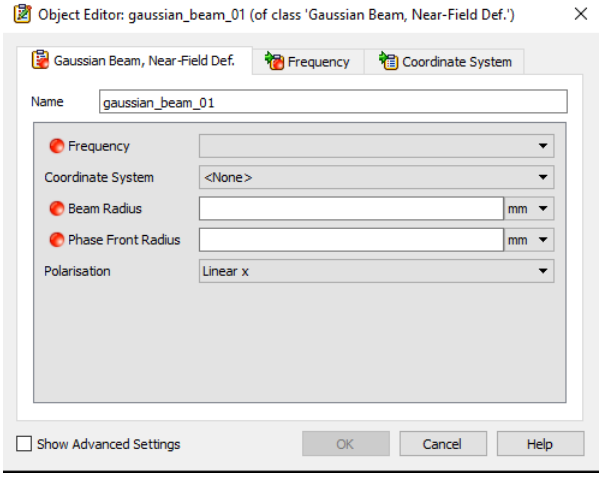

FIGURE 2.10: Input requirements to define a near field Gaussian field source.

2.5.3.3 Planar Cut

In *GRASP 10.5* to calculate the output field of a system, a user defined class known as *Field Storage* must be defined. For example a planar cut defines the field points in cuts on a plane, at a defined distance from the reference coordinate system. The user must define the near distance, cut type (radial or circular), rho range which defines the range of the radial coordinate, phi range, which defines the range of the azimuthal angle, E/H field and polarisation.

A planar cut can be defined using the following equation:

$$\hat{r}(\rho, \phi) = \hat{x}\rho\cos\phi + \hat{y}\rho\sin(\phi) + \hat{z}z, \tag{2.51}$$

where z_d is the distance to the near field plane defined by the *Near Dist.* For a radial cut, ϕ is fixed and ρ runs through the values using Equation 2.52

$$\rho_i = \rho_{\text{start}} + \Delta\rho \cdot (i-1), \quad i = 1, 2, \ldots, n_\rho \tag{2.52}$$

with

$$\Delta\rho = (\rho_{end} - \rho_{start}) \,/\, (n_\rho - 1)\,, \tag{2.53}$$

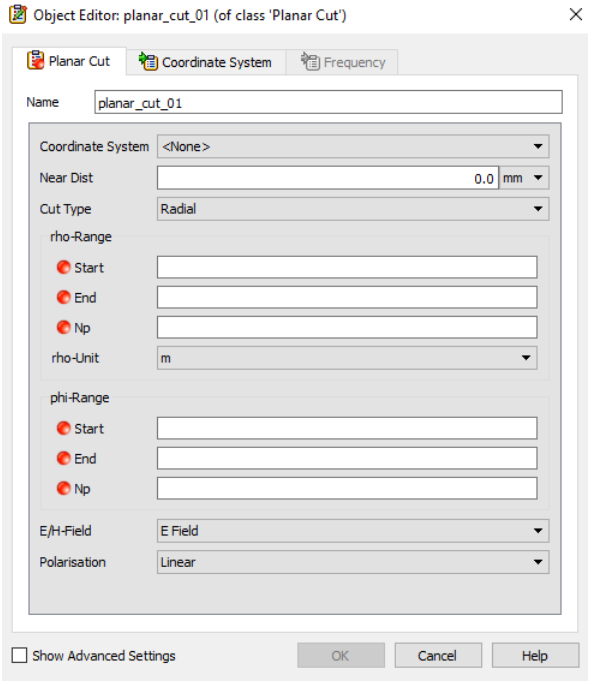

FIGURE 2.11: Input requirements for Planar cut

where rho_{start}, rho_{end} and rho_{np} are the user defined values from figure 2.12 rho_{end} (Start, Stop and number of points).

The ϕ angle is increased from equidistantly from one point using the equation below :

$$\phi_j = \phi_{start} + \Delta\phi \cdot (j-1), \quad j = 1, 2, \ldots, n_\phi, \tag{2.54}$$

where

$$\Delta\phi = (\phi_{end} - \phi_{start}) \,/\, (n_\phi - 1)\,. \tag{2.55}$$

ϕ_{start}, ϕ_{end} and n_ρ are the user defined start, end and number of points seen in Figure 2.12.

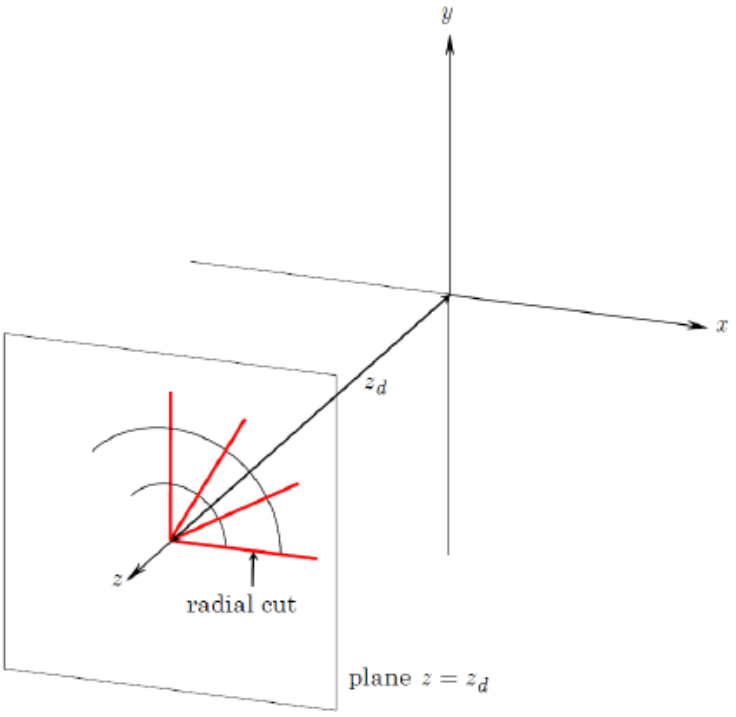

FIGURE 2.12: Planar cut in *GRASP 10.5* at a plane at a distance z_d =8 m, with 4 radial cuts between 0=< ρ => 2.6 m and $\phi = 0°, 30°$,30° and 90° [TRICA, 2015]

2.5.3.4 Planar Grid

The class planar grid defines a set of field points in a 2D grid on a plane whose position is defined by the user. This 2D grid is defined by the variables X-Range and Y-range seen in Figure 2.13. These variables take in a user defined start position, end position and number of points which define the extent of the grid. X and Y are defined as :

$$\begin{aligned} X &= X_s + \Delta X(i-1), \\ Y &= Y_s + \Delta Y(j-1), \end{aligned} \tag{2.56}$$

where i and j are defined as:

$$\begin{aligned} i &= 1, 2, ...N_x, \\ j &= 1, 2, ...N_y. \end{aligned} \quad . \tag{2.57}$$

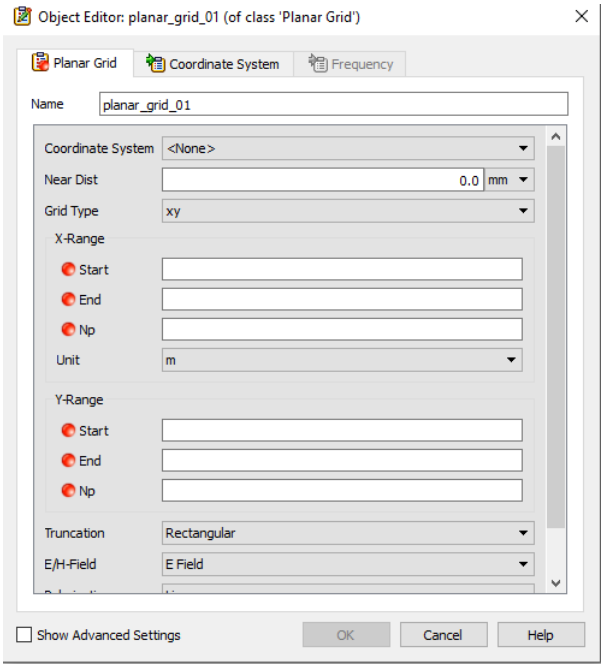

FIGURE 2.13: Parameters for planar grid

Xs and Ys are the start values and N_x and N_y are the number of points np which have been defined in X Range and Y Range, $\Delta\ X$ and $\Delta\ Y$ are the spacing's in the grid.

$$\begin{aligned} \Delta X &= (X_e - X_s) / (N_x - 1), \\ \Delta Y &= (Y_e - Y_s) / (N_y - 1). \end{aligned} \tag{2.58}$$

For an xy grid, the output grid is shown below in Figure 2.14.

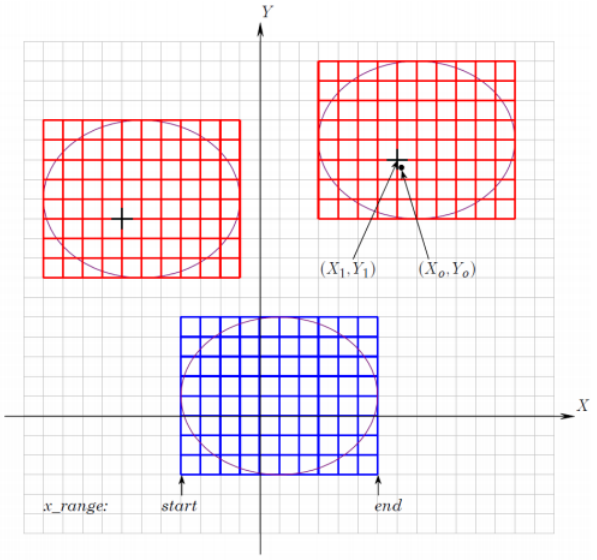

FIGURE 2.14: Planar grid in *GRASP 10.5* at a plane at some distance $z_0 = z_d$. The xy is drawn for -0.5 m $\leq x \leq$ 0.5 m, 0 m $\leq y \leq$ 0.5 m with a grid spaing of 0.1 m in both x and y

Other variables such as polarisation, truncation and E field /H-field can also be defined.

2.5.4 Dual Reflector Wizard

The dual reflector wizard is a user interface in *GRASP 10.5* which makes use all of the object functions (scatterers, surfaces, Rims, coordinate systems etc.) and EOs (frequencies, feeds, field source etc.) to create a telescope with two mirrors in a standard configuration. It is ideal for implementing different telescope designs if the optical design parameters are known. Figure 2.15 shows the different optical design parameters needed to create a dual reflector system. The wizard will generate all of the required GOs, EOs and Commands needed to design and analyse a specific optical setup. The Wizard also satisfies the Mizuguchi condition (explained below). Alongside this a spherical cut is placed in the farfield of the primary of the mirror to analyse the performance of the telescope design.

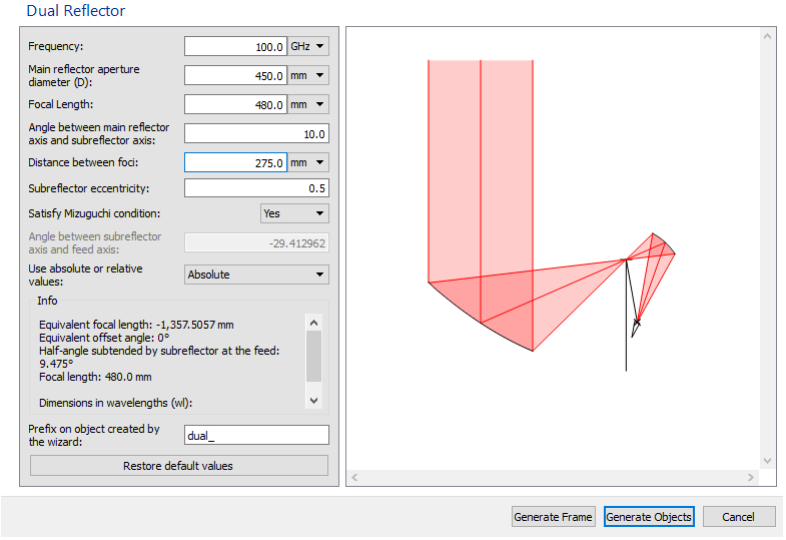

FIGURE 2.15: The user must input the frequency, primary reflector diameter, focal length, angle between the main reflector axis and sub reflector axis, distance between the focii and sub reflector eccentricity to generate the required dual reflector system

2.5.4.1 Mizuguchi Condition

The Mizuguchi Dragone condition refers to the tilt element introduced to a decentered telescope to eliminate cross polarisation caused by the asymmetrical configuration of the two reflectors. This means a decentered optical system such as a Cassegrain or Gregorian will have a tilt between the axes of symmetry of the primary and secondary which eliminates cross polarisation. This is known as a "Mizuguchi-Dragone telescope" [Shauly et al., 2013, p 22].

2.5.5 Commands

Once the optical system has been designed, *GRASP 10.5* carries out calculations via the Commands interface. The Command window accesses all of the PO and field storage that the user has previously defined as an EO. To carry out a PO analysis two commands are necessary : "*Get currents*" and "*Get Fields*". "*Get Currents*" calculates the induced currents on a reflector. It requires a feed and a

PO Analysis object. Currents are generated in succession, modelling the propagation of a real beam through an optical system. The "*Get Field*" command is used to get the EM filed stored in the filed storage object and computes the field by integrating over those currents. The projected grid or planar cut would then appear in the results, showing the E field the user specified.

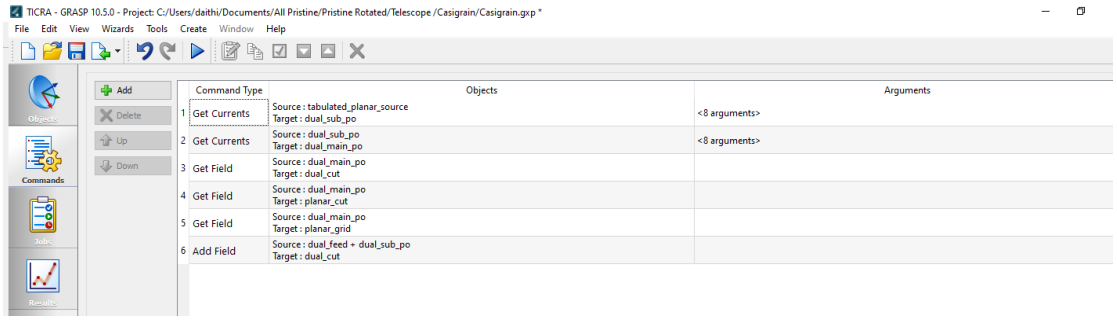

FIGURE 2.16: Commands window in *GRASP 10.5*. The list position defines where the command will be executed.

2.6 CST

The commercial package CST was used extensively throughout this thesis, especially in Chapter 4 for the modelling and analysis of the GRIN lenses. CST Studio Suite [CST] is a 3D EM analysis and design software package used for analysing and optimising EM components and systems. CST uses the Finite Integration Technique (FIT) which discretises Maxwells equations (integral from) which can be solved numerically [Clemens and Weiland, 2001].

$$\oint_{\partial A} \vec{E} \cdot d\vec{s} = -\int_{A} \frac{\partial \vec{B}}{\partial t} \cdot d\vec{A}, \tag{2.59}$$

$$\oint_{BA} \vec{H} \cdot d\vec{s} = \int_{A} \left(\frac{\partial \vec{D}}{\partial t} + \vec{J} \right) \cdot d\vec{A}, \tag{2.60}$$

$$\oint_{BV} \vec{D} \cdot d\vec{A} = \int_{V} \rho dV, \tag{2.61}$$

$$\oint_{\partial V} \vec{B} \cdot d\vec{A} = 0. \tag{2.62}$$

To solve these equations numerically, a finite domain must first be calculated which encloses the application or element in question.

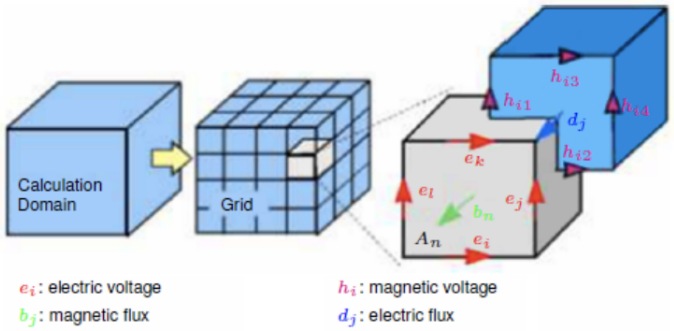

FIGURE 2.17: Illustraion of meshing in CST [CST, 2019].

A mesh is created and divides the domain into many smaller grid cells. This primary mesh can then be visualised in CST using the *mesh view*. Internally, a second secondary mesh is created which is orthogonal to the first mesh grid. Then spatial discretisation is performed on both of the grid systems. To illustrate the FIT technique, let us consider Figure 2.17. For each of the cells, Maxwell's equations are formulated for each cell facet. Now let us consider Equation 2.63. $E \cdot dS$ in Faraday's law (Equation 2.59) can be written as a sum of the 4 grid voltages $(e_i + e_j - e_k - e_l)$. The magnetic flux of the enclosed cell facet (b_n) is equal to $\iint B \cdot \overline{dA}.$, which leads to Equation 2.63

$$(e_i + e_j - e_k - e_l) = -\frac{\partial}{\partial t} b_n. \tag{2.63}$$

If this is repeated for all of the facets we obtain the matrix formulation of Equation 2.64 which can be expressed using an operator $\mathbf{C}$

$$\underbrace{\begin{pmatrix} . & . & . & . \\ 1 & 1 & -1 & -1 \\ . & . & . & . \end{pmatrix}}_{\mathbf{C}} \underbrace{\begin{pmatrix} e_i \\ . \\ e_j \\ . \\ e_k \\ . \\ e_l \end{pmatrix}}_{\mathbf{e}} = -\frac{\partial}{\partial t} \underbrace{\begin{pmatrix} . \\ b_n \\ . \end{pmatrix}}_{\mathbf{b}}. \tag{2.64}$$

Which gives is the following equation

$$\mathrm{Ce} = -\frac{\partial}{\partial \mathrm{t}} \mathrm{b}. \tag{2.65}$$

Then if Ampere's law is applied to the dual grid we can define the corresponding dual discrete curl operator as $\tilde{C}$. Similarly, if Equation 2.60, 2.61 and 2.62 are discretised a complete set of equations known as *Maxwell's Grid Equations* are obtained:

$$\begin{aligned} \mathrm{Ce} &= -\tfrac{\mathrm{d}}{\mathrm{dt}} \mathrm{b}, \\ \tilde{\mathrm{C}}\mathrm{h} &= \tfrac{\mathrm{d}}{\mathrm{dt}} \mathrm{d} + \mathrm{j}, \\ \tilde{\mathrm{S}}\mathrm{d} &= \mathrm{q}, \\ \mathrm{Sb} &= 0. \end{aligned} \tag{2.66}$$

The continuous gradient, curl and divergence operator proprieties are all maintained in grid space [Weiland, 1996]. In addition to orthogonal hexahedral grids described here, FIT can also be applied to more general mesh types such as tetrahedral and irregular grids which can be seen in Figure 2.18.

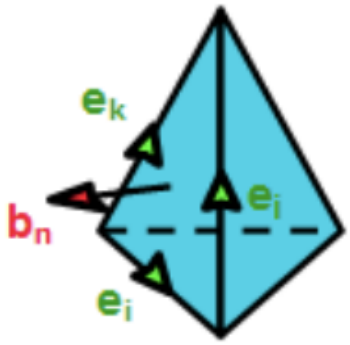

FIGURE 2.18: CST tetrahedral mesh cell,showing electrical voltage and magnetic flux vectors [CST, 2019].

2.6.1 CST Solvers

The CST Suite offers a number of different solvers, however within the Microwave studios there are only three solvers available:

1. Transient Solver
2. Frequency Domain Solver
3. Eigenmode Solver

The Transieint Solver is based on MGE (Maxwell's Grid Equations). To solve the time derivatives the central differences [Uddin et al., 2019] interpolation method is used. Substituting the time derivatives with the central differences yields the following equation.

$$\mathbf{e}^{n+1/2} = \mathbf{e}^{n-1/2} + \Delta t \mathbf{M}_z^{-1} \left[\widetilde{\mathbf{C}} \mathbf{M}_\mu^{-1} \mathbf{b}^n + \mathbf{j}_S^n \right], \tag{2.67}$$

$$\mathbf{b}^{n+1} = \mathbf{b}^n - \Delta t \mathbf{C} \mathbf{e}^{n+1/2}. \tag{2.68}$$

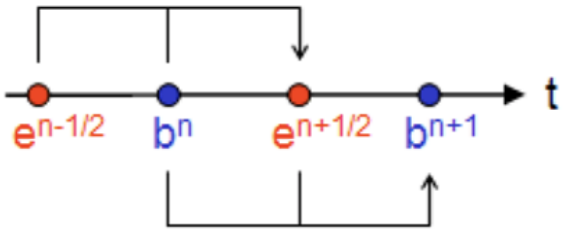

FIGURE 2.19: Leapfrog method implemented by the transient solver in CST

where $e^{n+1/2}$ and $e^{n-1/2}$ are past and future electrical voltages and $b^{n+1/2}$ and $b^{n-1/2}$ are past and future magnetic fluxes. Both of these unknowns are located in time and are demonstrated in the leap frog scheme shown in Figure 2.19

2.6.2 Gaussian Beam Solver

CST allows the user to define the EM source in many (trivial) ways for each individual system. To simulate EM radiation within the W band (75-110 GHz) the *Gaussian Beam source* was primarily used to generate the input EM fields $\|E_{input}\|$.

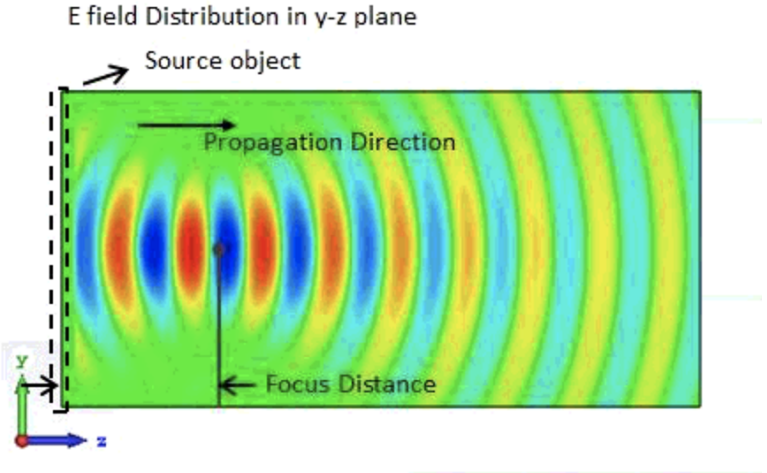

FIGURE 2.20: Distance of the defined Gaussian beam with respect to the minimum beam radius and the source object in question.[CST, 2019]

To define a source the user needs several input variables which have been highlighted in Figure 2.21, available as a macro in CST. The minimum beam radius, frequency and position of the source must be supplied to simulate the beam. The position of the object with respect to the source is shown in Figure 2.20.

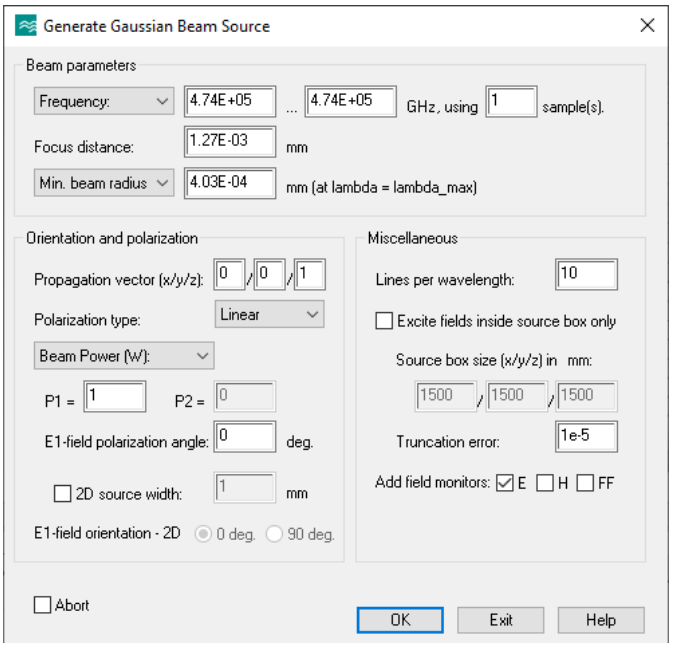

FIGURE 2.21: Shown above are the different criteria required to define a Gaussian beam source in CST [CST, 2019]

Chapter 3

Pristine

3.1 Introduction

In this chapter the different techniques used to model and analyse PRISTINE (Primordial Radiation Interferometer for Spectral Distortion and Inflation) are presented. PRISTINE is a mission proposal for the ESA fast (F) mission call in 2018. The criteria for this call were for a fast, cheap mission - details at https://sci.esa.int/web/cosmic-vision/-/60498-call-for-a-fast-f-mission-opportunity-in-esa-s-science-programme. To analyse PRISTINE's optical train two approaches were taken: namely Gaussian beam mode analysis and a full physical optics approach using commercial software *GRASP 10.5*. The aim when modelling a quasi-optical system such as PRISTINE is to efficiently couple the radiation of the source through the optical train to a set of detectors.

PRINSITNE is a space mission concept designed to map the CMB anisotropies in temperature and polarisation, hence allowing the measurement of the large scale polarisation patterns caused by relic gravitational waves produced during inflation. It will also measure the CMB spectrum with two orders of magnitude improvement over the limits of COBE/FIRAS [Nabila et al., 2018].

To achieve these daunting feats, this chapter will deal with the testing and design for the pFTS (polarisation Fourier Transfrom Spectrometer) and main telescope. The instrument itself includes two focal planes, each including a multi-moded horn-coupled dual-polarisation boltmeter, cooled down to 100 mK. The optical inputs for the two arms of the pFTS are two co-aligned telescopes in the adjacent double barrel baffles. Each telescope with 360 mm primary mirror diameter is designed to be as compact as possible.

Two modes of operation are planned to be implemented: a polarisation mode where the two detectors are looking simultaneously at the sky and the spectral distortion mode where a source is compared to a well calibrated blackbody calibration load. The onboard blackbody itself will be calibrated to a temperature of 2.73 K to match that of the CMB to limit the noise floor. This requires that the detectors also observe the on board calibration source to accurately characterise observed temperature of the CMB.

3.2 Primary Science Goals

The two main goals of the PRISTINE science mission are to measure the CMB B-mode polarisation and spectral distortions. More details on B-mode polarisation Chapter 1, Section 1.3.4 and Section 1.3.3. At the largest angular scales (above 10°), photons that re-scattered during cosmic reionisation are imprinted with both an E-mode and B-mode signal. The E-modes allow researchers to constrain the Thomson optical depth which is vital in understanding the CMB damping tail (seen in Figure 1.7). Thomson optical depth τ, in the context of CMB observations, is a unitless quantity which provides a measure of the line-of-sight-free-electron opacity to the CMB radiation. Using the assumption that reionisation is instant at redshift z_{reion}, τ is calculated as an integral of the electron density times the Thomson cross section over the geometrical path length calculated between z = 0

and z_{reion} [Griffiths et al., 1999]. B-modes gives researchers access to the scalar-to-tensor-ratio r. This parameter is related to the energy scale of inflation models, which can also be geometrically interpreted as the expansion of the Universe during inflation.

With a unique combination of resolution, sky coverage, sensitivity and continuous frequency coverage from 90-3000 GHz, PRISTINE aims to measure dust properties at peak emissions. These emissions are needed for foreground subtraction in order to reach a scalar to tensor ratio of r = 10^{-2}, which will lead to a more confident measurement of B-modes, while also providing a low resolution mapping of the dust polarisation, which will help ground based astronomy assess dust contamination and residuals in results. Pristine will [Nabila et al., 2018]:

- Provide frequency coverage and spatial resolution which enables researchers to characterise the Spectral Energy Distribution (SED) of the polarised dust emissions.
- Measure B-mode CMB polarisation patterns and achieve a 3 sigma measure of r$\approx 10^{-2}$.
- Measure τ from large scale E-mode polarisation allowing for more accurate estimations of the neutrino masses at recombination.

PRISTINE aims to measure two types of spectral distortions: Compton y distortion from energy release in the optically thin regime at redshifts $z < 5 \times 10^4$ and the chemical potential μ distortions in the optically thick regime at z > 5×10^4. PRISITNE will improve the current distortion measurements (measured by COBE/FIRAS) by a factor of 20 on μ and 300 on y. After decoupling at z $\sim 10^3$ the matter perturbations created evolved into the first stars and galaxies. These galaxies evolved in filaments and clusters. The inverse Compton scattering of the CMB photons with the thermal electrons of the ionised gas during reionisation

generated a y distortion of order 2×10^{-6}. Combining the E-mode polarisation angular spectrum and the spectral distortion researchers will be able to measure the reionisation process. PRISTINE intends to measure :

- The complete hot gas content and hidden baryons in the Large Scale Structures (LSS) through measurement of Compton y distortion 2×10^{-6} at 80σ.
- The relativistic corrections to the y-distortions allowing researchers to measure electron temperatures of hot gas down to $kT_eSZ \approx 1.3keV$ at 3σ.
- Chemical potential μ, 4 $\times 10^{-6}$ at 95 CL% [Nabila et al., 2018].

3.2.1 Secondary Science Goals

The secondary science goals of PRISTINE characterised by [Nabila et al., 2018] aim to :

- Discover the polarisation of Galactic line emission from C, CII, CI and NII and OI and CO polarisations over the whole sky.
- Measure the Cosmic Infrared Background to previously unattained accuracy. PRISTINE will uniquely probe the link between dark-matter density at redshifts 1-4 by measuring the SED of the power spectrum of CIB fluctuations.
- Measure low resolution maps in the far infared (CII and CO) from galaxies at redshift $5 < z < 9$.
- Measure the monopoles, dipoles and the diffuse background emissions of the CMB, with factors 1000 and 100 improvement on the monopole and on the dipole.

3.3 Requirements

Frequency range and resolution: [Nabila et al., 2018] states that the frequency range required to achieve the scientific goals are from 90 GHz - 3 THz. To monitor the dust SED, measurements of up to 3 THz are needed. The observation of y distortion requires measurements down to at least 100 GHz. Below this threshold, the signal is mainly made up of synchrotron emission. To measure some of these synchrotron emission signals, lower frequencies are needed. The lower end of the frequency range was set 90 GHz to allow for these synchrotron emission observations, whilst still allowing for a compact instrument. PRISTINE's baseline spectral resolution, 5 GHz, allows for detection of spectral lines in distant galaxies or in the MilkyWay.

Angular resolution: PRISITNE will have an equivalent Gaussian beam-width of 0.75° at 90 GHz enabling determination of inflationary signal at both the recombination peak as well as the rionisation peak.

Sky Coverage: Full sky coverage, which is only possible from space, is needed to detect CMB E-and B-mode polarisations at the largest scales of the reionisation peaks.

Sensitivity: A sensitivity of in the order of 2.6 $\mu\mathrm{K}_{CMB}$ at 90 GHz (0.46 $\mu\mathrm{K}_{CMB}$ integrated over all the frequencies). PRISITNE's baseline will be optimised to reach the μK°_{CMB} sensitivity needed to ensure a 3σ detection. This will allow researchers to reach a y accuracy of 10^{-6} at 80 σ.

PRISTINE aims to map the sky through a continuous scanning pattern, spinning around its axis while performing spectroscopic measurements in the 90 GHz - 3 THz range with a polarised Fourier Transform Spectrometer (pFTS).

3.4 GRASP Output Beam Characterisation

3.4.1 Beam Fitting

Beam fitting refers to a method of fitting a perfect equivalent Gaussian function (shape only) to an output radiation field. This allows for the retrieval of vital parameters from the output field such as beam Gaussicity and determines if the system in question has significant levels of optical aberrations.

To fit an equivalent Gaussian to an output field Equation 2.9 from Section 2.1 was used.

$$f(x) = \exp\left(\frac{x^2}{w_x^2}\right)^2, \tag{3.1}$$

$$f(y) = \exp\left(\frac{y^2}{w_y^2}\right)^2. \tag{3.2}$$

The above equations are in their one-dimensional form. Using Equation 3.1 and 3.2, the beam radius and the closeness or match (Gaussicity) of the beam to an ideal Gaussian at a distance z away from the source can be calculated. The model can also be expanded to include a lateral amplitude displacement of size x_0 in one direction:

$$f(x) = \exp\left(\frac{(x - x_0)^2}{w_x^2}\right)^2, \tag{3.3}$$

$$f(y) = \exp\left(\frac{(y - y_0)^2}{w_y^2}\right)^2. \tag{3.4}$$

3.4.1.1 Verification of a Predefined Gaussian Function

Before any fitting algorithm can used with *GRASP 10.5* simulation data must first be tested and verified. The fitting code was written in a *Jupyter Notebook*, which has a large library of data analysis and fitting modules. For this particular fitting algorithm, the *lmfit* package was used, which has useful modeling functions such as *lmfit.Model().fit*. This function requires the user to pass a predefined function (e.g an equivalent Gaussian Equation 3.3) into the *Model()* class. Once the model is defined, an estimated fit to the model using the simulated data can be calculated. Using the *Model.fit* function and passing the normalised data, an initial beam radius estimation ω and an initial offset value x_0 are returned.

To test the function, a simple test example was calculated. Using the function below with predefined beam radius and offset values, a fit estimation was made with Equation 3.3, including the x_0 offset variable:

$$f(x) = \exp\left((x - 2.5)^2/(12^2)\right)^2. \tag{3.5}$$

Once the cut in *GRASP 10.5* has been produced, both it and the model function are passed to *limfit.Model.fit*. The function will then calculate the variable parameters of the model parameters such that analysis data set will be reproduced. The fitted values can then be retrieved and plotted against the original data set. The fitted variables can be accessed by using the *.fit report* command or the *.params* command. Table 3.1 demonstrates the fitted variables the analysis data.

Variable Name	**Predicted Value**	**Relative Error**	**Initial Guess**
Beam waist w_x	12 mm	0 mm	12 mm
Lateral displacement in X x_0	2.5 mm	0 mm	2.5 mm

TABLE 3.1: Returned parameters from the fitting code using a predefined Gaussian as the data set

3.4.1.2 Example of *GRASP 10.5* Data Fitted to Gaussian Model

Correctly fitting the predefined function with the fitting algorithm is only the first step to ensure it is fully functional and operational. Actual verifiable data, with a well known beam radius value and offset from *GRASP 10.5* must be used to ensure the algorithm is working as intended. To verify the beams are being fitted correctly, a Gaussian beam source with a predefined waist of 10 mm was defined and the frequency was set to 150 GHz in *GRASP 10.5*. To do this the Gaussian beam pattern was created using a near-field beam pattern definition object in *GRASP 10.5*. A planar cut (-20 mm to 20 mm) was placed at the source. Using the same fitting process as from Section 3.4.1.1, except using *GRASP 10.5* data as the data being analysed. Table 3.2 below represents the fitting data.

Variable Name	**Predicted Value**	**Relative Error**	**Initial Guess**
Beam waist w_0	10 mm	0 mm	10 mm
Lateral displacement in X x_0	0 mm	0 mm	0 mm

TABLE 3.2: Returned parameters from the fitting code using GRASP 10.5 data as the data set

3.4.2 Gaussicity & Ellipticity

3.4.2.1 Gaussicity

In order to characterise the optical quality we define the term Gaussicity. Gaussicity of a beam is its power coupling to a pure Gaussian field. e.g., [O'Sullivan and Murphy, 2012]. It is usually expressed as a percentage of the coupling of the identical Gaussian beam. Using the normalised overlap integral of the output field and the equivalent Gaussian for a linear Gaussicity in the x or y direction: [Byrne, 2017]

$$\eta_{\text{Gaussicity x}} = \frac{\iint E_{\text{Gauss}} E^*_{\text{x,out}} dx}{\iint E_{\text{Gauss}} E^*_{\text{Gauss}} dx \iint E_{\text{x,out}} E^*_{\text{x,out}} dx}, \tag{3.6}$$

$$\eta_{\text{Gaussicity y}} = \frac{\iint E_{\text{Gauss}} E^*_{\text{y,out}} dy}{\iint E_{\text{Gauss}} E^*_{\text{Gauss}} dy \iint E_{\text{y,out}} E^*_{\text{y,out}} dy}. \tag{3.7}$$

Gaussicity is suitable to characterise the optical performance of a system like PRISTINE. A high Gaussicity after propagation though the optical system suggests the beam shape is still symmetric and therefore indicating low level aberrations. A system with perfect coupling will have a Gaussicity of 100%. A high Guassicity indicates that optical train is achieving optimal radiation transfer through all the components in the system (assuming a Gaussian beam input). A low Gaussicity indicates optical aberrations are present in the system and affecting beam quality.

3.4.2.2 Ellipticity

The ellipticity of a beam is its deviation away from the circularly symmetric (Gaussian) profile:

$$e = 1 - \frac{b}{a}, \tag{3.8}$$

where a and b are the major and minor axis length of the ellipsoid. Ellipticity is a useful parameter to use in the analysis of optical systems. The shape of a beam will be affected by each off-axis optical component in the system as it propagates to the receiver plane. This could potentially cause the beam to become distorted. It is therefore useful to have a parameter such as ellipticity to see how well the system conserves beam symmetry. For a system such as PRISITNE which aims to produce a well collimated beam on the sky, the ellipticity can be used as a

standard measure. An ellipticity of less then 5% is usually a requirement for CMB measurement systems.

PRISITNE's ellipticity will be calculated for output beams in both the vertical and horizontal directions cut, to characterise if any aberrations are present in the output beam.

3.5 Optical Design

To detect the aforementioned B and E-modes, PRISITINE will combine multi-moded detectors with the pFTS to provide the sensitivity needed for the CMB polarisation detection. This pFTS design is vital for separation of the CMB from the Galactic foreground emission. This is vital for flagging false B-mode detection which in the past have been misinterpreted. For PRSITNINE a Martin-Puplett pFTS [Martin and Puplett, 1970] has been chosen due to its reliability in the field and success in characterisation of spectral responses of instruments such as the Keck Array [Karkare et al., 2014], BICEP3 and the Atacama Cosmology Telescope (ACT) [Datta et al., 2016]. Figure 3.1 shows a schematic diagram of the PRISITNE instrument layout and pFTS design, with the secondary and primary mirrors used for the telescope.

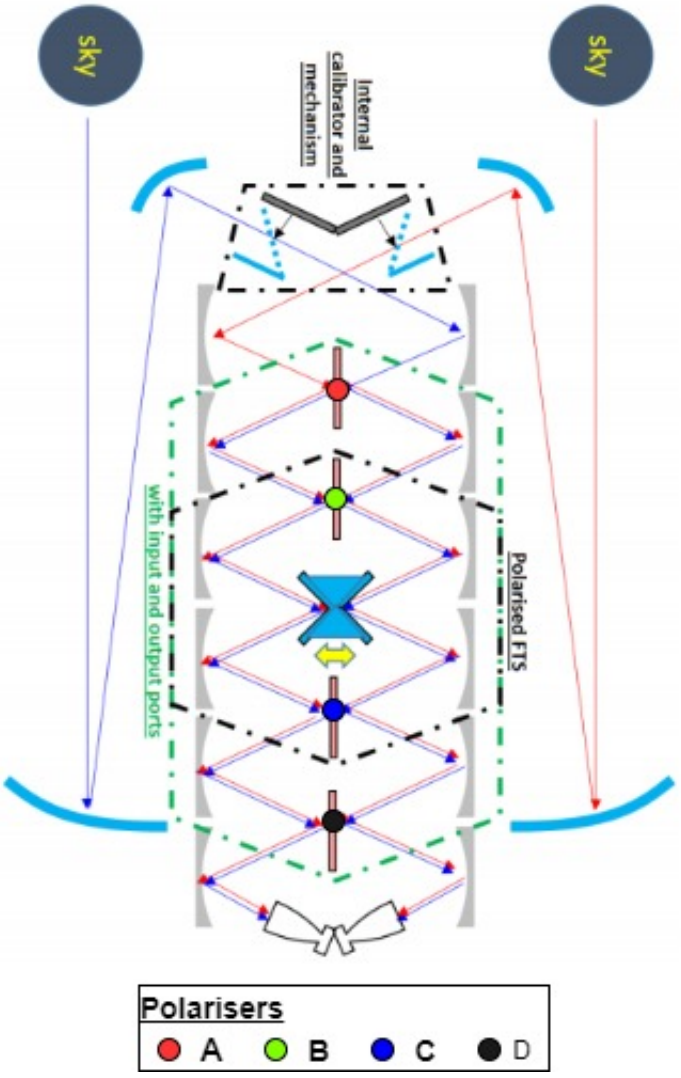

FIGURE 3.1: Schematic diagram of PRISTINE's 12 mirror optical array (Mirror 1-10, pFTS), secondary mirror and primary [Nabila et al., 2018, p. 6].

The pFTS design is known as a Martin Puplett design which is based on a Michelson interferometer, however it has some notable differences. Figure 3.1 shows the instrument concept. There are two identical paths for the two beams from each of the two telescopes. Two off-axis primary mirrors, which produce twin co-aligned beams with the space craft spin axis. The primary and secondary mirrors guide the beam into the FST. Two sets of six transfer mirrors, reflect the radiation through a series of wire polarising grids. Polariser A splits the beam into two output beams. This is achieved using a wire grid polariser which transmits vertical polarisation

and reflects horizontal polarisation separating the beams into their corresponding orthogonal states. Using this wire grid also allows the beam splitter to be frequency independent. The second polariser (B) has wires angled at 45° relative to polariser A, which then mixes the polarisation states. Then a mirror transport mechanism moves the diehedral mirrors as to shorten or lengthen the optical path causing a phase delay. These mirrors also rotate the beam polarisation by 90°. After the phase delay the beams recombine at polariser C, which has wires angled at 45°. Polarisers B and C essentially modulate the polarisation of the input beam which can be used to suppress spurious noise in the input beam and unpolarised sources. Then polariser D (which has the same polarisation state as A), splits the beams again, and we end up with 4 different output signals (two orthogonal polarisations and two angled at 45°), effectively separating the Stoke's parameters (Q,-Q,U,-U).

3.5.1 12 Mirror Array

Each reflector in the 12 reflector array had a diameter of 77 mm allowing for a space of 3 mm in between each mirror in the array. Reflectors 1-10 are part of the pFTS, reflectors 3-10 having identical design parameters due to the symmetry of the system. Reflector one and two have slightly different design parameters due to the position of the detector horns. The mouths of the horns are positioned 100 mm horizontally and 40 mm vertically away from the first reflector. This means the ellipsoid f_1 focus would be positioned 107.7 mm from the reflector. f_2 was set to 25 km, effectively creating a paraboloid (an elliptical mirror equivalent to a parabolic) which collimates the output radiation. The angle of throw of the beam was set as 33.72°. The incoming radiation approaches with an incident angle of 16.86°.

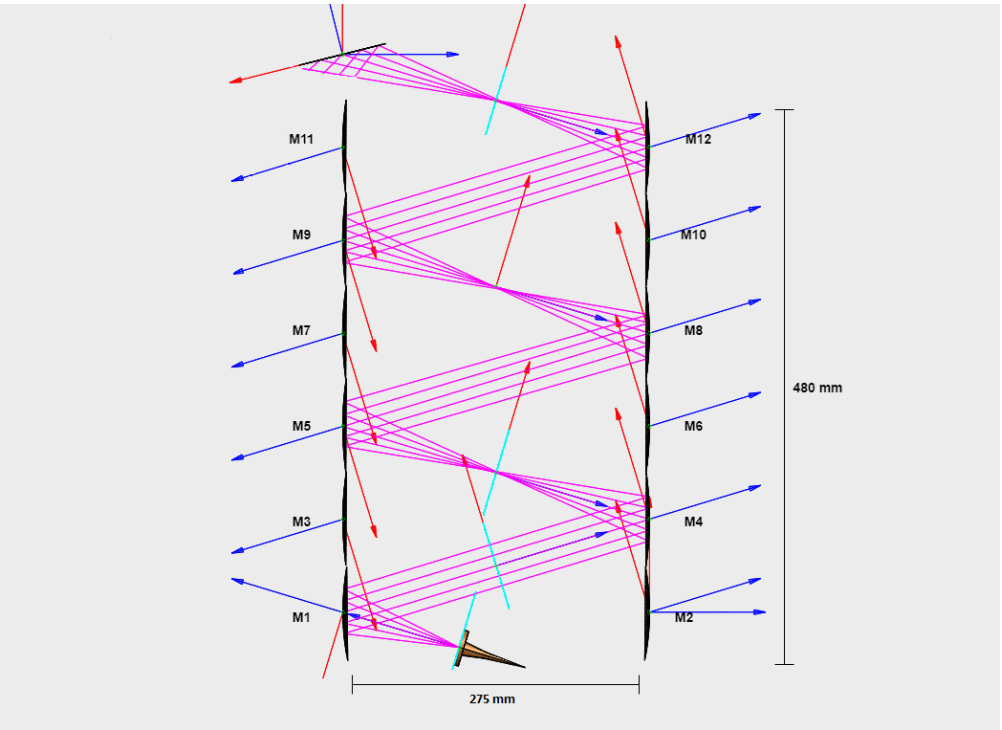

FIGURE 3.2: Schematic diagram of the 12 mirror array in *GRASP 10.5*

Using the variables above, the elliptical parameters for M1 and M2 where defined. These parameters where calculated using the *Second Order* class written in python (as described in Section 2.5.2.1). These parameters are recorded in Table 3.3.

Mirror Parameters	
Mirror	M1 & M2
Semi-Major axis	12500054 mm
Semi-Minor axis	24829 mm
Interfocal Distance	24999910 mm
F1	107.7 mm
F2	25 km
Radius of Curvature	215.4 mm
Eccentricity	0.99
Conic Constant	-0.99
Characteristic Polynomial	$2.61 \times 10^{-3}x^2 + 2.61 \times 10^{-3}y^2 + 4 \times 10^{-8}z^2$=0

TABLE 3.3: Geometric parameters of elliptical surface for M1&M2

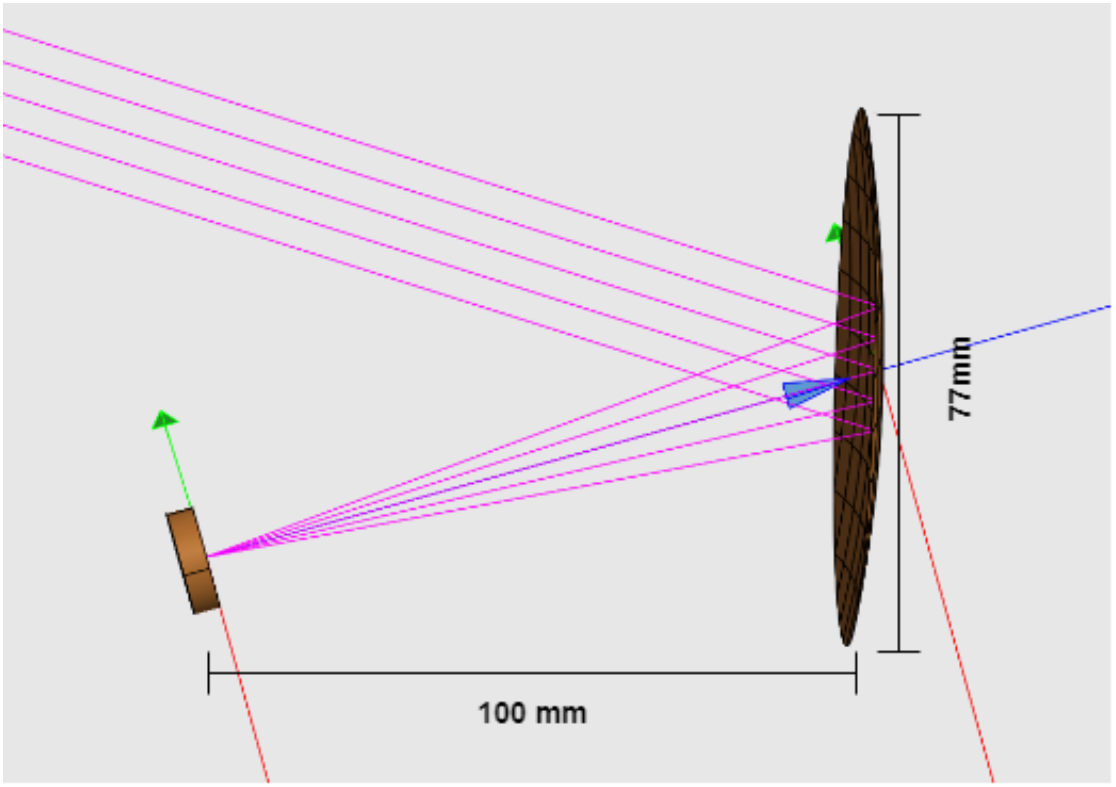

FIGURE 3.3: Mirror 1 of the FTS modeled in GRSAP. The incoming radiation has an angle of incidence of 16.86°. The mirror has an angle of throw of 33.72°. The mirror is positioned 100 mm from the source (in the horizontal axis), making the the radiation path length R_1 107.7 mm.

Reflector M3-M12 have the same ellipse parameters and focal length of 137.93 mm and angle of throw 33.72°, with the second focus being placed at 25 km to make an elliptical mirror effectively equivalent to a parabola. All of the ellipse parameters from M3-M10 are presented in Table 3.4.

Mirror Parameters	
Mirror	M3-M12
Semi-Major axis	12500069 mm
Semi-Minor axis	28099 mm
Interfocal Distance	24999885 mm
F1	137. 93 mm
F2	25 km
Radius of Curvature	275.4 mm
Eccentricity	0.99
Conic Constant	-0.99
Characteristic Polynomial	$1.98 \times 10^{-3}x^2 + 1.98 \times 10^{-3}y^2 + 4 \times 10^{-8}z^2$=0

TABLE 3.4: Elliptical parameters for M3-M12

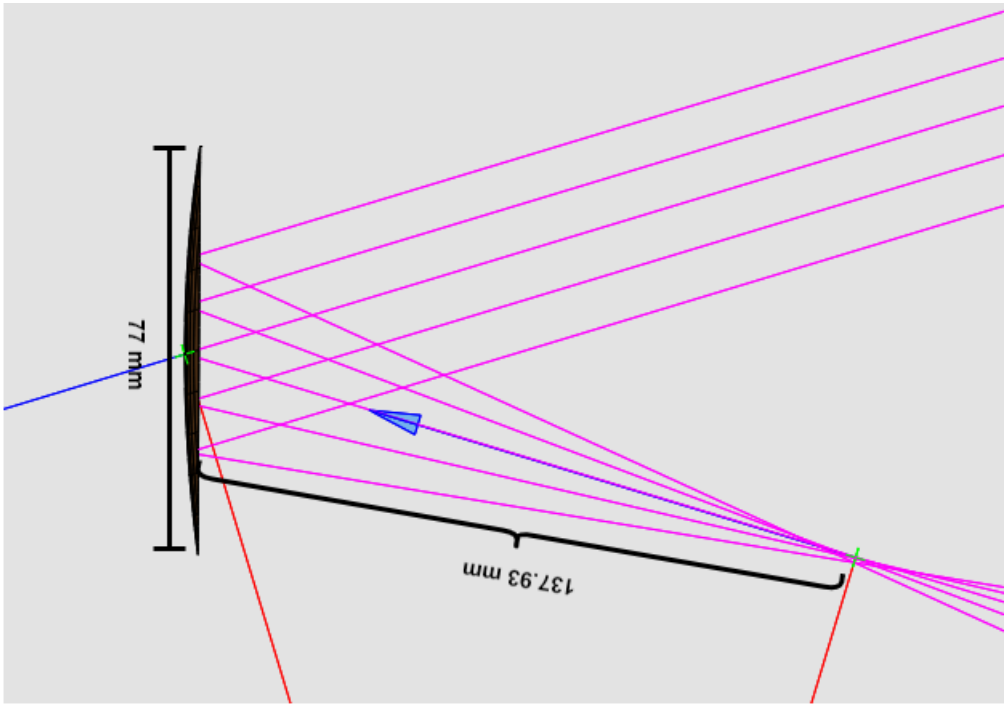

FIGURE 3.4: Mirror 3 of the FTS modeled in GRSAP. The incoming radiation has an angle of incidence of 16.86°. The mirror has an angle of throw of 33.72°. The radiation path length R_1 is 137.93 mm to the focus

3.6 Analysis of the pFTS Array

This section will discuss the GBMA of the six mirror array (i.e. one path through the symmetric system of 12 mirrors in total) carried out for 150 GHz. The specific design of the two different mirrors used in the array has been discussed in the Section 3.5 and analysis of the two mirrors, and the whole six mirror array will be investigated here. The beam was a Gaussian source in the *GRASP 10.5* menu. This is a coherent beam at a single frequency rather than actually representing the multi-moded detector which will be used ultimately. It is a good preliminary analysis and will allow us to characterise the optical performance of the system in a general way. The Gaussian source had a beam waist of 10 mm with a phase front radius equal to infinity, unless stated otherwise. A fundamental Gaussian beam was used as the equivalent Gaussian to fit the *GRASP 10.5* data, its beam radus being calculated using Equations 2.33, 2.32 and an appropriate ABCD matrix written in *Mathematica* to represent the optical train in question.

A full linear Gaussicity calculation of the x and y cuts along the horizontal and vertical axes of each output plane from *GRASP 10.5* was performed using the beam fitting routine. The ellipticity was also calculated then from the fitted Gaussian beams.

3.6.1 Mirror 1 & 2

In *GRASP 10.5* a flat 30×30 mm^2 planar grid and planar cut between -30 mm and 30 mm were placed 137 mm away from M1. The E field generated in *GRASP 10.5* was exported and fitted with an equivalent Gaussian using the *Jupyter Notebook* fitting function at 150 GHz. The results are shown below in Figure 3.5(a), 3.5(b), 3.6 and Table 3.5.

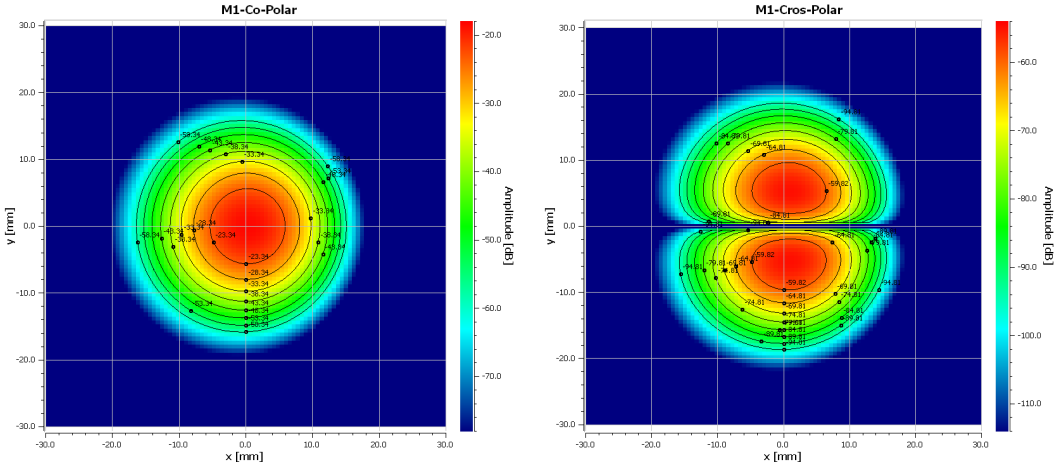

(a) Co-polar beam

(b) Cross polar beam

FIGURE 3.5: 30×30 mm contour map of 150 GHz co and cross polar beam taken 137.93 mm away from M1

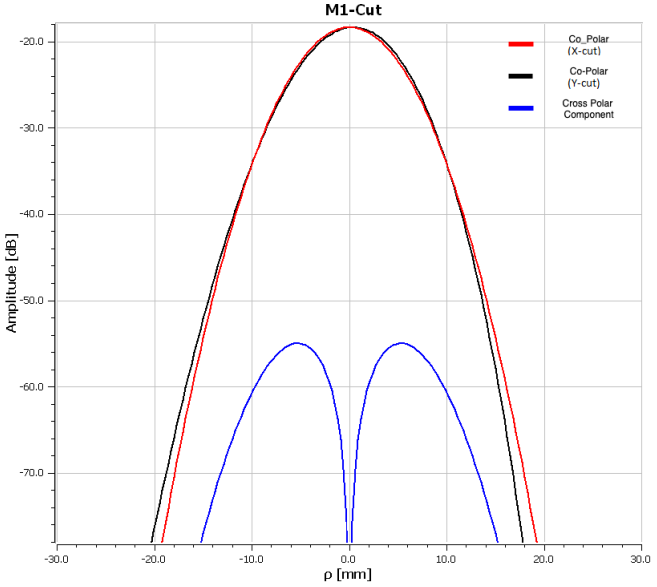

FIGURE 3.6: 30×30 mm^2 planar cut of 150 GHz co and cross polar beam taken 137.93 mm away from M1

Gaussian Beam Parameters	
ω_x (mm)	7.44
ω_y (mm)	7.42
GBMA ω (mm)	7.41
Offset x (mm)	-0.31
Offset y (mm)	0
Gaussicity x (mm)	99.98%
Gaussicity y (mm)	100%
Ellipticity	0.3%

TABLE 3.5: Gaussian beam parameters for a beam reflected from M1 using an initial ω_x and ω_y of 10 mm

An initial estimation of the beam radius is needed in the fitting code, so to calculate this value a 12 mirror ABCD matrix was written in *Mathematica* using Equations 2.2 2.32 and 2.33 and beam radius values where found at different locations along the optical train. From this, ω_x and ω_y were calculated, and used as the initial value for the fitting function. The initial and best fit could also be used to compare GBMA theory against PO and PTD (*GRASP 10.5*). Figure 3.7 shows the initial and best fit plotted against the *GRASP 10.5* data. (Note the initially fitted data is a perfect Gaussian field created using ω value from the aforementioned ABCD matrix and equations)

Table 3.5 shows the estimated beam radius values after mirror 1. The GBMA predicts the beam to have a radius (symmetric x and y) of 7.41 mm. If we compare this to the fitted waists for the x and y direction cuts of simulated data, we see that the beams have agreement in the first two terms but differ in the last significant figure. This is further backed up by the fact that the y-direction cut is 100% Gaussian meaning there is no optical distortion in the y-direction cut. However when we consider the x-direction cut of the beam radius, the GBMA waist is experiencing some minor optical distortion in this direction as expected due to the off axis nature of the mirror. Figure 3.7 shows this displacement from

the ideal on-axis Gaussian. This small offset is introduced into the system due to the off axis illumination of the mirror (16.86°). This off axis illumination also introduces a small amount of ellipticity into the beam. This ellipticity is rather small at this point. Overall the beam quality is very high which is demonstrated in Figure 3.5(a) and 3.6. We can see the main co-polor component has a maximum amplitude of -18 dB and a much lower cross-polarisation of -56 dB. This means that the majority of the power is in the co-polar component with minimal power leakage into the cross polar.

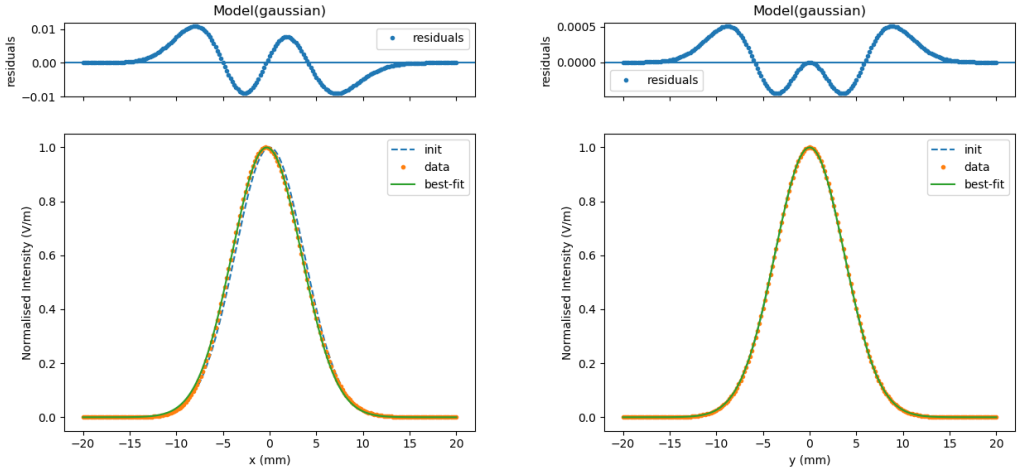

(a) X-component

(b) y component

FIGURE 3.7: Initial and best fit data plotted against M1 *GRASP 10.5* data

3.6.2 Mirrors 3-12

The remaining mirrors in the array were all designed using the surface coefficients seen in Table 3.4. In *GRASP 10.5* the surface design was first tested in isolation using an off axis Gaussian beam illumination with an incidence angle of 16.86° and a waist of 10 mm. The waist was positioned at the mirror's focus $R_1 = 137.93$ mm from away from the mirror. A planar grid (30 × 30 mm^2) and a planar cut (30 × 30 mm^2) where then taken at $R_2 = 137.93$ to get the output field of the optical

system. The E fields generated in the cuts were then exported to the Gaussian fitting algorithm for further analysis.

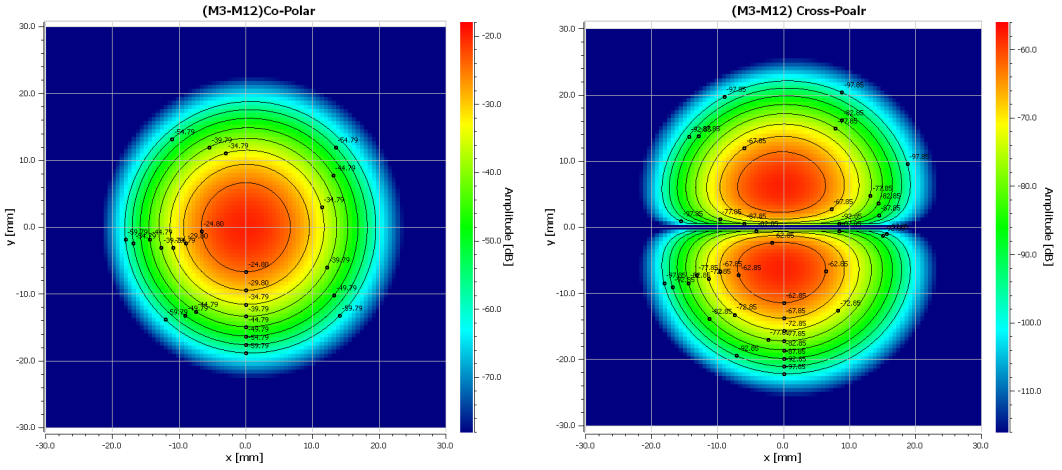

(a) Co-polar (b) Cross-polar

FIGURE 3.8: 30×30 mm^2 contour map of 150 GHz co and cross polar beam taken 137.93 mm away from M3

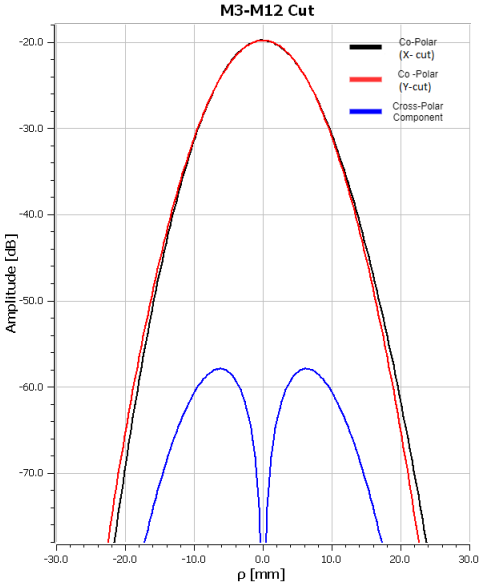

FIGURE 3.9: 30×30 mm^2 planar cut of 150 GHz co and cross polar beam taken 137.93 mm away from M3

Gaussian Beam Parameters	
ω_{x0} (mm)	8.80
ω_{y0} (mm)	8.79
GBMA ω_{xy} (mm)	8.78
Offset x (mm)	-0.04
Offset y (mm)	0
Gaussicity x (mm)	100%
Gaussicity y (mm)	100%
Ellipticity	0.02%

TABLE 3.6: Gaussian beam parameters for M3 - M12

An initial fit estimation from the GBMA preformed before fitting the beam radius, estimates the beam should have beam radius of 8.78 mm. Much like mirror 1 and 2, the design for mirror 3-12 has an optimal surface seen in Table 3.4, with minimal optical aberrations.

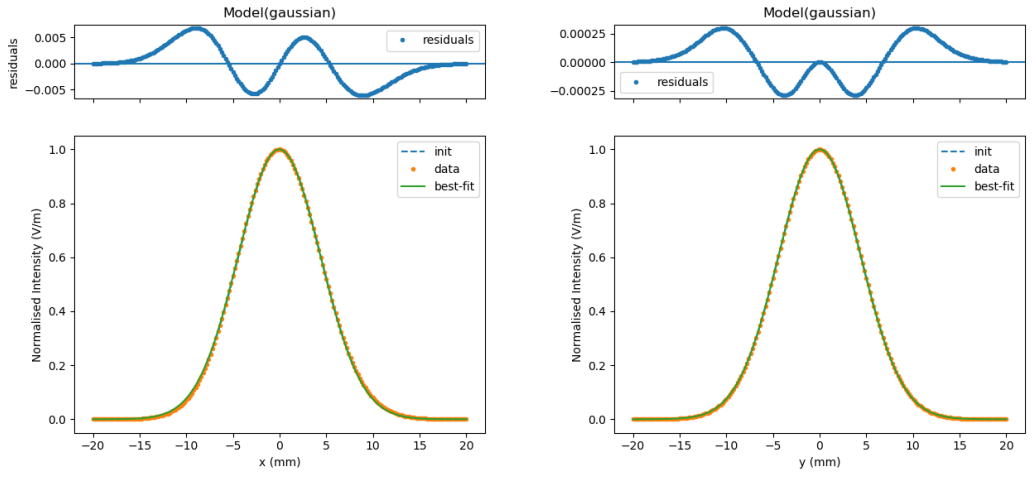

(a) X-component

(b) Y-component

FIGURE 3.10: Initial and best fit data plotted against M3-M12 *GRASP 10.5* data

.

We see small aberrations in the x direction cut of the beam which is due to the off axis illumination of the mirrors. There is a very minor ellpiticity in the beam. The x and y direction are in good agreement as seen in Figure 3.9. Below -35 dB the two components begin to deviate from each other. Again nearly all of the power of the beam is contained within the co-polar component, with a maximum E field of -20 dB, a much smaller proportion of the power being in the cross-polar component.

3.6.3 Beam Exiting the Array

To get an idea of the E field as the beam leaves the pFTS and enters the telescope, a Gaussian source (waist=10 mm, incidence angle of 16.86°) was placed 100 mm away from mirror one. An output grid and planar cut was then placed at the focus of M12, to calculate the E field of the beam as it exits the array of mirrors. These fields where then exported to *Jupyter Notebook* for further Gaussian beam fitting and analysis.

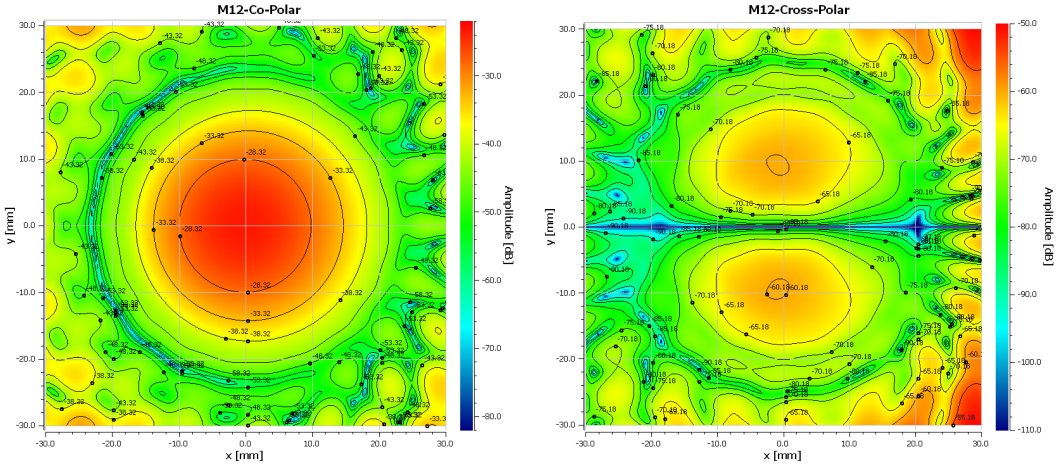

(a) Co-polar (b) Cross polar

FIGURE 3.11: 30×30 mm^2 contour map of the 150 GHz co and cross-polar beam taken 137.93 mm (at the focus) away from M12

.

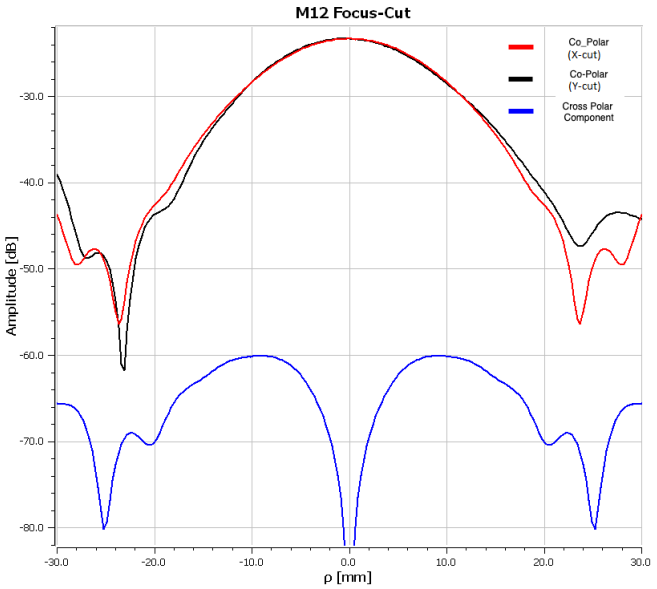

FIGURE 3.12: 30×30 mm^2 planar cut of 150 GHz co-polar beam taken 137.93 mm away from M12

.

Gaussian Beam Parameters	
ω_x (mm)	13.06
ω_y (mm)	13.14
GBMA ω (mm)	13.03
Offset x (mm)	-0.19
Offset y (mm)	0
Gaussicity x (mm)	99.94%
Gaussicity y (mm)	100%
Ellipticity	0.7%

TABLE 3.7: Gaussian beam parameters for M12 beam exit

The overall beam structure as it leaves the pFTS is mostly symmetric, but still contains a slight offset and small optical aberrations. The ellipticity has increased, compared to its values from Table 3.5 and 3.7 to 0.7%. Although this has increased,

it is still low so it is not significant. The Gaussian fit to the beam can be seen in Figure 3.13.

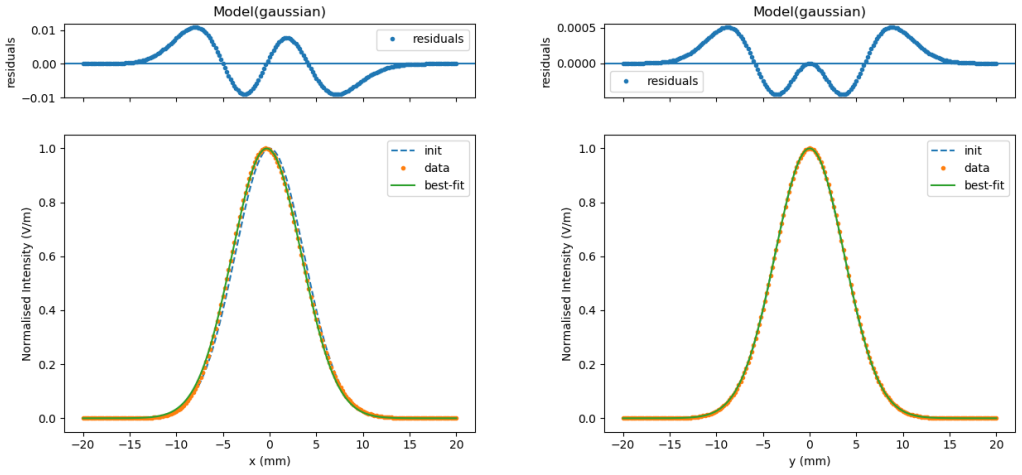

(a) X-component

(b) Y-component

FIGURE 3.13: Initial and best fit data plotted against M12 *GRASP 10.5* data

3.6.4 Cassegrain Telescope Design

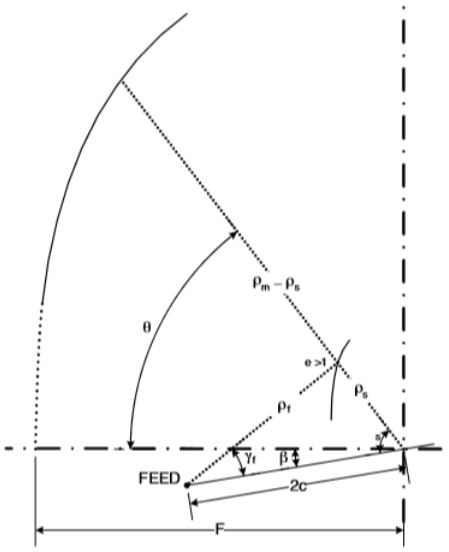

FIGURE 3.14: Cassegrain schematic and design parameters needed for *Reflector Wizard* [TRICA, 2015]

Finally to relay the beam from the pFTS to the sky, an appropriate telescope must be chosen. A simple Cassegrain design was chosen and designed using *GRASP 10.5 Reflector Wizard*. Using the parameters in Table 3.8 a hyperbolic secondary was designed to collect the incoming radiation and focus the beam 137.90 mm from M12 in the pFTS optical train. Figure 3.14 shows a schematic diagram of the parameters needed to design Cassegrain telescope in the *Reflector Wizard*.

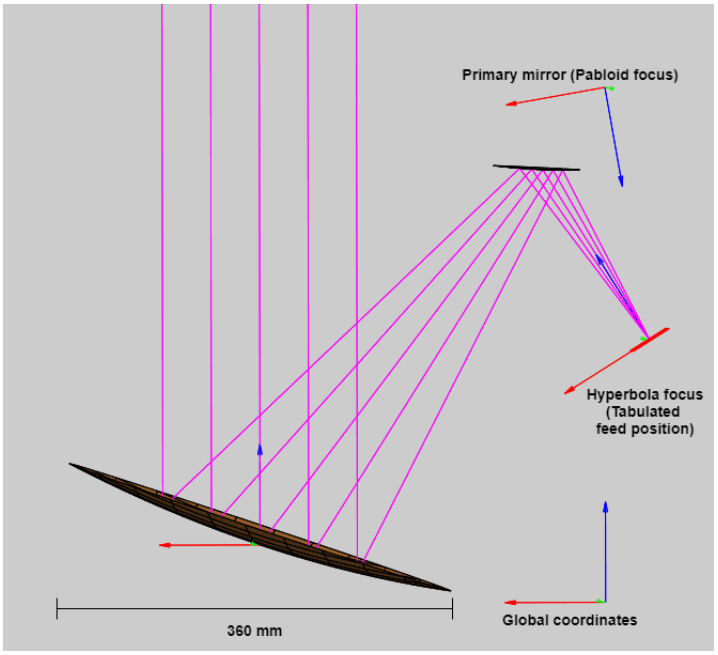

FIGURE 3.15: Telescope design in GRASP 10.5

Cassegrain Telescope		
Geometric Parameters	**Secondary**	**Primary**
Semi-Major axis (mm)	92.366	Infinity
Interfocal Distance (mm)	242.0	Infinity
Focal length (mm)	-578.37	486.0
Radius of Curvature (mm)	-1156.74	972
Eccentricity	2.62	1
Conic Constant	-6.8644	-1

TABLE 3.8: Geometric parameters for the primary and secondary mirrors of the Cassegrain telescope

To measure the projected beam profile of from PRISITNE's telescope, an output planar cut and planar grid were placed 850 mm away from the primary mirror of the Cassegrain system. Then using *Tabulated Planar Source*, the output field from Figure 3.11(a) was used as the source. The source was positioned 137.93 mm away, to emulate the position of the secondary mirror in Figure 3.2. The source was then propagated through the telescope to a grid and planar cut positioned 850 mm from the primary mirror. These fields where then exported to *Jupyter Notebook* for further Gaussian beam fitting and analysis.

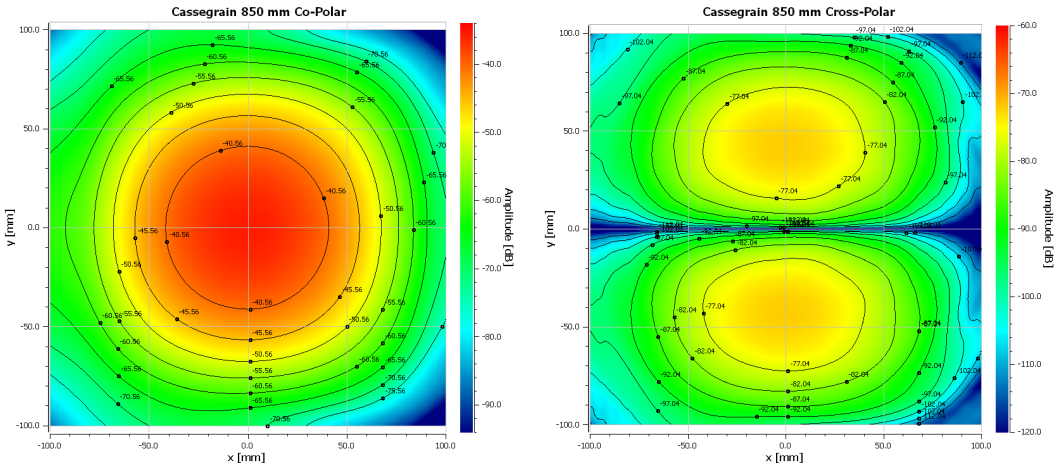

(a) Co-polar

(b) Cross polar

FIGURE 3.16: 100×100 mm^2 contour map of 150 GHz co and cross polar beam taken 850 mm away the primary mirror.

The final planar farfield cut (seen in Figure 3.16(a) and 3.17) is behaving very well and has very high beam quality overall. Due to the offsets and tilts of the secondary and primary mirror in the telescope system and pFTS, there are some minor aberrations in the system. The x and y directions have a Gaussicity of 99.96% and 99.95% corresponding to a very high quality beam on the sky. With an ellipticity of 2%, we can see that the original elliptcicty in the x direction and the y direction of the beam has propagated though the optical train additivly. For CMB missions such as PRISITNE an ellipticity of under 5% is required to

Gaussian Beam Parameters	
ω_x (mm)	54.80
ω_y (mm)	53.68
GBMA ω (mm)	53.58
Offset x (mm)	-0.22
Offset y (mm)	0
Gaussicity x	99.96%
Gaussicity y	99.95%
Ellipticity	2%

Gaussian Beam Parameters	
ω_x (mm)	0.71°
ω_y (mm)	0.71°
ω (mm)	0.75°
Offset x (mm)	0.01
Offset y (mm)	0
Gaussicity x	99.85%
Gaussicity y	99.95%
Ellipticity	1.1%

TABLE 3.9: Left: Gaussian beam parameters for a cut taken 850 mm from the Cassegrain primary mirror. Rigth: Gaussian beam parameters for spherical farfield cut.

achieve highly calibrated results. So even with this ellipiticity, the system will still perform well.

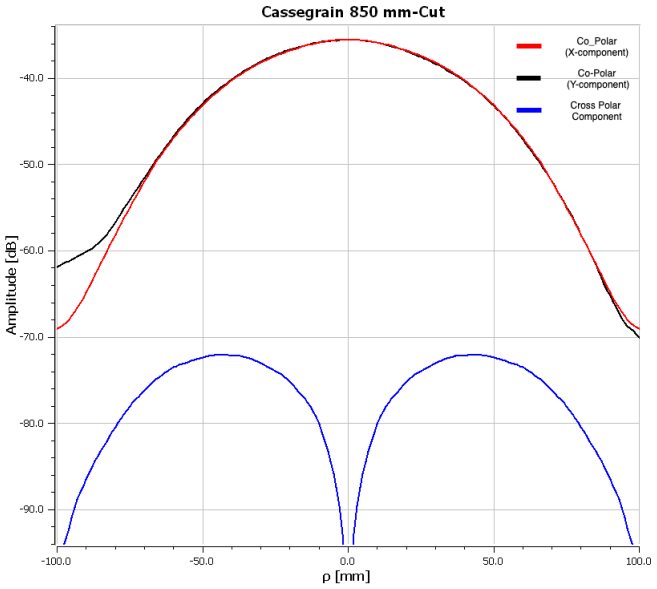

FIGURE 3.17: 100×100 mm^2 contour planar cut taken 850 mm away the primary mirror

Finally if we consider a cut of the farfield of the beam between $-1.5° \rightarrow 1.5°$ in the sky we can see how well the beam will be projected onto the sky. From Figure 3.18 below, we can see the x and y cuts of the beam are very similar to one another, albeit the x component has a slight offset. Figure 3.18 also shows there is no on-axis cross polar component, which is the ideal scenario. The on-axis co polar

component has a peak at 47.12 dB, whilst the off-axis cross polar components have much lower peaks at 10.85 dB and 8.30 dB.

If we consider the fit of the data from Table 3.9, we see both the x and y cuts have the same value of 0.71°.

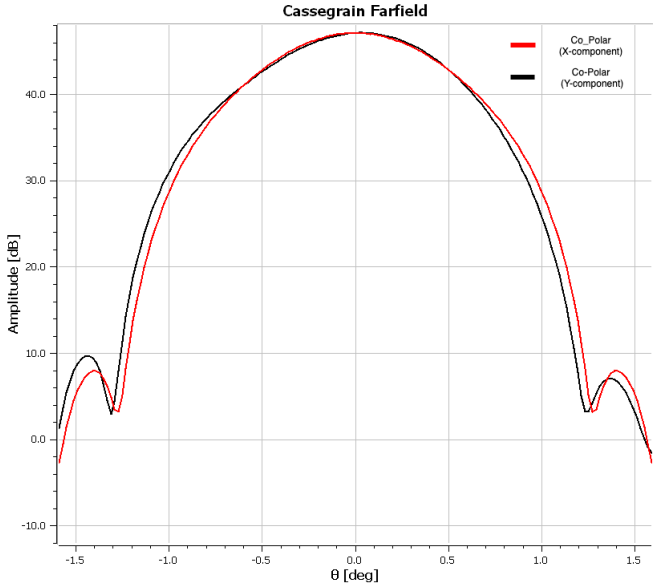

FIGURE 3.18: Far field cut of the Cassegrain telescope beam taken at 150 GHz

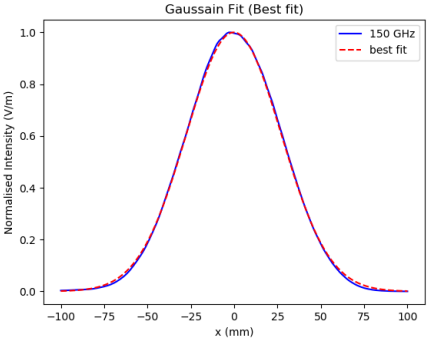

(a) Full beam (X-cut)

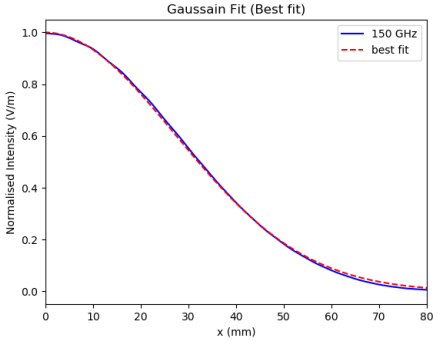

(b) (Close up of fit from 0-80 mm on the x-axis)

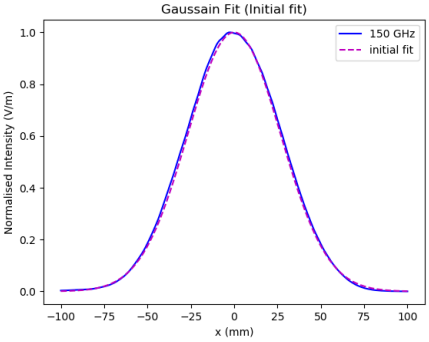

(c) Full beam (X-cut)

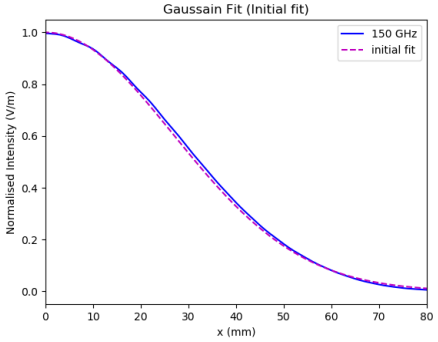

(d) (Close up of fit from 0-80 mm on the x-axis)

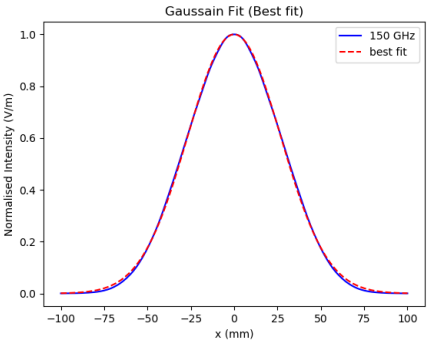

(e) Full beam (Y-cut)

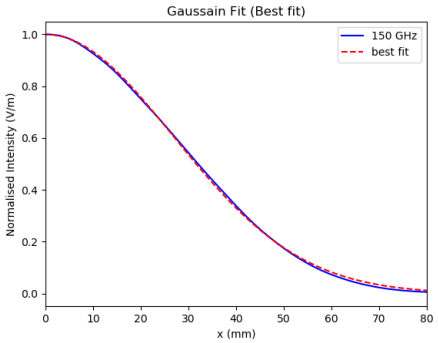

(f) (Close up of fit from 0-80 mm on the axis)

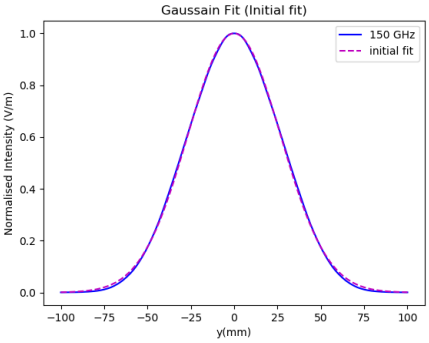

(g) Full beam (Y-cut)

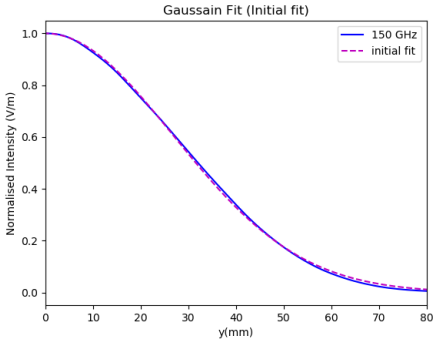

(h) (Close up of fit from 0-80 mm on the x-axis)

FIGURE 3.19: x and y cut of the initial and best fitted data plotted against *GRASP 10.5* data (planar cut at 850 mm from primary.

3.7 Conclusion

The goal of this chapter was to fully design and analyse an optical train for PRISNTINE's pFTS and telescope using a single mode Gaussian source. To do so, two different mirror designs were chosen to guide the radiation to the array exit. To design the specific mirror surface geometries a class of functions was written and verified using an example in *GRASP 10.5*. The output for the class can be seen in Figure 2.8(b) and its implemented design in Figure 2.8(a). Once verified, the two mirrors could be designed in *GRASP 10.5* using the outputted 2^{nd} order polynomial. Using the design specifications outlined in Section 3.5.1, the geometric parameters of each mirror are presented in Table 3.3 and 3.4, proceeding this they were implemented in *GRASP 10.5* (Figure 3.3, 3.10(a) and 3.10(b)). These elliptical mirrors were designed to have minimal optical aberrations and be within the dimension requirements of the mission mechanic constraints.

Once designed the *GRASP 10.5* results where fitted with equivalent Gaussian beam radius from the fitting code written in *Jupyter Notebook*. This code was tested against known Gaussian beam radii and then imported *GRASP 10.5* data to verify its operation and the results for this can be seen in Section 3.4.1.1, Table 3.1 and 3.2. For the first case, a Gaussian function was created using Equation 3.5. In this first example the fitted beam radius and offset in Table 3.1 matched the given beam radii values in Equation 3.5, verifying that the algorithm is capable of correctly fitting data from a predefined data set in *Jupyter Notebook*. For the second example, an example data set from *GRASP 10.5* was fitted to a Gaussian function. As seen in Table 3.2 both the fitting function and the *GRASP* 10.5 data are in agreement with each other.

To test how well these offset ellipitcal surfaces performed, they were compared with an equivalent Gaussian, whose input was determined by an ABCD matrix analysis written in *Mathematica*. The equivalent Gaussian represents the putput

from a perfect system with no with optical aberrations. This can then be fitted to the simulated data outputted from *GRASP 10.5* as a bench mark (initial) fit to the data. Both sections of the optical train (M1 & M2, M3-M12) performed excellently in isolation, showing no optical aberrations in the y direction of the beam (100% Gaussicity in both mirrors,see Table 3.5 and 3.7) and near perfect Gaussicity of 99.98% for the x-direction of M1 & M2 and 100% for M3-M12. The offset nature of the input horn caused some small optical distortion and ellipticity in the beam which also had a slight offset in the x-direction (-0.31 mm), which is mostly accounted for by design (e.g. the axis rotation of the ellipse).

Once both mirrors were analysed, the full optical array could be fully analysed. A cut at the focus of M12 provides us with insight into the beam profile as it leaves the array of mirrors e.g. Figure 3.11(a), 3.11(b), 3.12 and 3.13. The beam behaved as expected , except the ellipiticty of the beam had propagated and become higher.

Finally to verify the beam pattern on the sky, a two mirror Cassegrain telescope was designed in *GRASP 10.5* using the parameters in Table 3.8. A cut and grid were taken at 850 mm from the primary mirror and a spherical cut was taken on the sky. The far field shows a highly symmetrical beam which is offset from the centre by 0.01mm. Both the x and y directions have a beam radius of 0.71°. The final beam has very high Gaussicity of 99.85% and 99.95%, meaning that there are minimal power losses in the optical train, leading to a very efficient transfer of radiation energy.

If research were to continue on the optics of PRISTINE, optimisations of the two different elliptical surface designs could be explored. Mirror sag and other variables could be explored and optimised using optical software such as Zemax, which has a library of optical optimisation tools to minimise optical aberrations. Different telescope designs could also be implemented, to determine which design best matches the optical requirements of the system. A more complicated (but

compact) telescope design could be achieved if the secondary mirror reflected the beam out of the plane of the pFTS. This would required a specialized secondary mirror surface to offset the optical aberration from the tilting and offsetting of the beam to achieve this more complicated design.

Chapter 4

GRIN Lens - Gradient index lens

4.1 Introduction

This chapter examines the methods for the design and modelling of a GRIN (Gradient Index) lens using the Gaussian beam mode and finite element (CST) analysis techniques described in Chapter 2. Supplementary to this, some material analysis of the PLA (thermoplastic polylactic acid) used to print both a proto-lens and final lens design is included, as it is necessary to understand the focusing characteristics of the lens design.

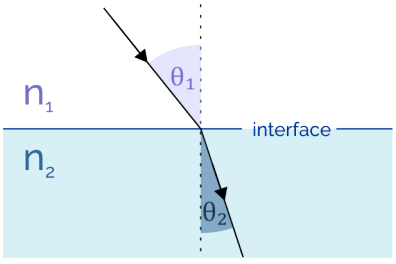

FIGURE 4.1: Illustration of Snell's law at a planar non-GRIN interface [Haponiuk, 2020]

In general, lenses are used to collimate beams and to transform planar wavefronts into spherical waves or vice versa. Incident rays at the interface of a traditional

isotropic lens change direction due to a change of refractive index in the new material. Then, the final path of the ray is usually dictated by the lens surface geometry and the relative refractive index (n_1) of the surrounding medium, as seen in Figure 4.1 (Snell's law).

The change in direction of the ray can be described using Snell's law [Haponiuk, 2020] equation 4.1.

$$n_1 \sin\theta_1 = n_2 \sin\theta_2. \tag{4.1}$$

In a GRIN lens, the index of refraction varies with distance from the centre of the lens. To focus any incoming EM radiation, one must try to mimic the phase delay caused by a curved lens. This phase delay is achieved by varying the refractive indices of planar material as a function of distance from the centre of the lens. A GRIN lens is in the form a disc, and its focal point is designed along its optical axis as seen in Figure 4.2. To focus the incident radiation after the lens, the refractive index should be largest at the centre of the lens and gradually decrease to the outermost ring [Kelleher and Goatley, 1955b]. To calculate the required refractive index, the phase delay of the radiation from the focal point can be used. θ is assumed to be the angle between the path where the rays enter the lens and the optical axis. Equation 4.2 shows the relationship between the radial permittivity ϵ_r and θ [Zhang et al., 2016]

$$\frac{T}{F}(\epsilon_r - \frac{2}{3}\sin^2\theta) = \sqrt{(\epsilon_r - \sin^2\theta)}(\sqrt{\epsilon_{r,max}}\frac{T}{F} - \sec\theta + 1), \tag{4.2}$$

where T is the thickness of the lens, F is the focal length of the lens and $\epsilon_{r,max}$ is the maximum permittivity at the center of the lens.

Beams being focused by GRIN lenses do not suffer from the spherical aberrations caused by spherical and convex lenses. Other advantages of GRIN lenses are their compact size and weight, and their low cost when compared with other lenses.

There have already been a number of studies on the applications and ability of GRIN lenses [Zhang et al., 2016][Imbert et al., 2015][Savini et al., 2012]. However, few experiments have been conducted in the 75–110 GHz range.

4.2 Lens Design

To manufacture a lens for the laboratory, the Anet A8+ 3D printer was used. This particular printer used thermoplastic polylactic acid (PLA). The process and printer specifications are described in Chapter 2, Section 1.4.1.

Due to the practicality of fabrication and the limited resolution of the 3D printer, an ideal smooth radial refractive index variation was approximated using a step function. This means that the lens can be made for a series of concentric rings with different relative permittivities. Figure 4.2 shows the basic design principle behind the lens geometry. Each ϵ_r was designed to focus the incoming radiation (plane wave moving from left to right) onto the focal point O in the diagram.

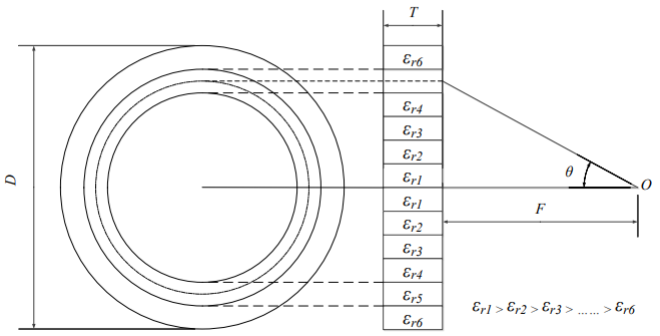

FIGURE 4.2: Geometry of GRIN lens [Zhang et al., 2016]

Several variables must first be known to apply Equation 4.2 to the lens design. θ_{max} is determined by the focal length and diameter of the lens. Due to the source and optical arrangement in the lab, which are discussed in detail in Section 4.4, the maximum beam radius entering the lens is 25 mm. Initially, an 80 mm diameter

prototype lens with a 150 mm focal length was designed, as this was the maximum size that could fit into an already designed lens holder in the laboratory. After the prototype was tested and the lens holder was updated, a second larger lens was then designed. Both lenses have a thickness of 10 mm. Once these values were known, the maximum permittivity could be found. To calculate the permittivity of different infill percentages of PLA, testing of different infill percentages was carried out using the VNA (vector network analyser) through precise measurement. The original prototype lens was designed assuming the 100% PLA infill had a permittivity $\epsilon_{r,max}$ of 2.72, originating from tests described in [Zhang et al., 2016]. The second lens was designed after PLA lab tests had determined the permittivity of PLA infills.

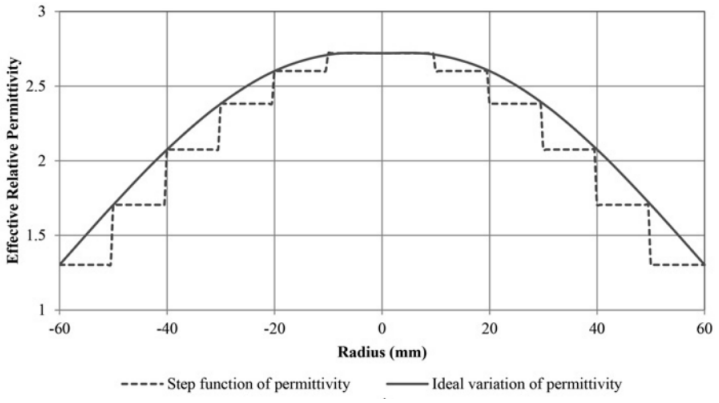

FIGURE 4.3: Illustration of step function plotted against the corresponding curved surface equivalent.[Zhang et al., 2016]

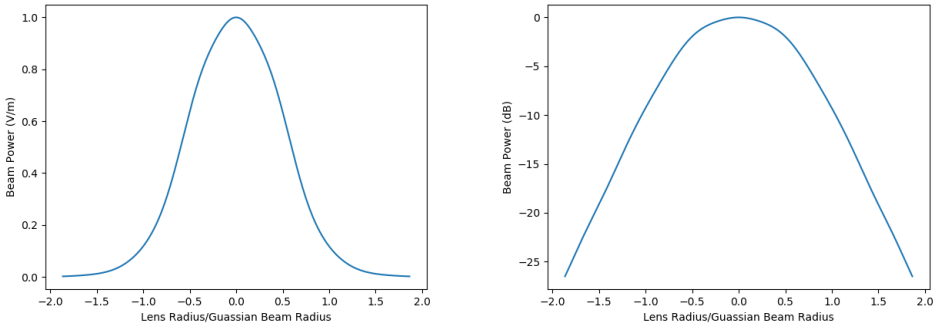

(a) Beam Intensity (V/m)

(b) Beam Intensity (dB)

FIGURE 4.4: Power distribution across the 100mm lens

4.2.1 Prototype Lens CST Simulation

Before measurements were taken in the lab, a full CST simulation was undertaken to characterise the response to the GRIN lens when illuminated with W-band frequency radiation. To simplify and reduce computational complexities, the GRIN lens was modelled as four concentric rings with homogeneous material. Each ring had a homogeneous dielectric constant (ϵ_r) which decreased from the centre to the outermost ring. A value of 2.72 was chosen for the centre ring based on a similar design from [Zhang et al., 2016]. Some early permittivity estimates performed by my colleague Joe Brennan calculated that an infill to air of 80% corresponded to a permittivity of 2.72. Since the beam focus is not completely dependent on the max ϵ_r, as seen in Equation 4.2, it is the gradient of ϵ_r from the lens that is most important when focusing the beam. This means the choice of ϵ is arbitrary. $\epsilon_{r,max}$ does however change the transmissions and reflection of the beam, and is frequency-dependent. Therefore, for the purpose of testing the beam-focusing properties of the lens, this estimation of $\epsilon_{r,max}$ was used.

Ring number	Relative Permitivity
1	2.72
2	2.33
3	1.95
4	1.56

TABLE 4.1: Permitivity profile of prototype lens

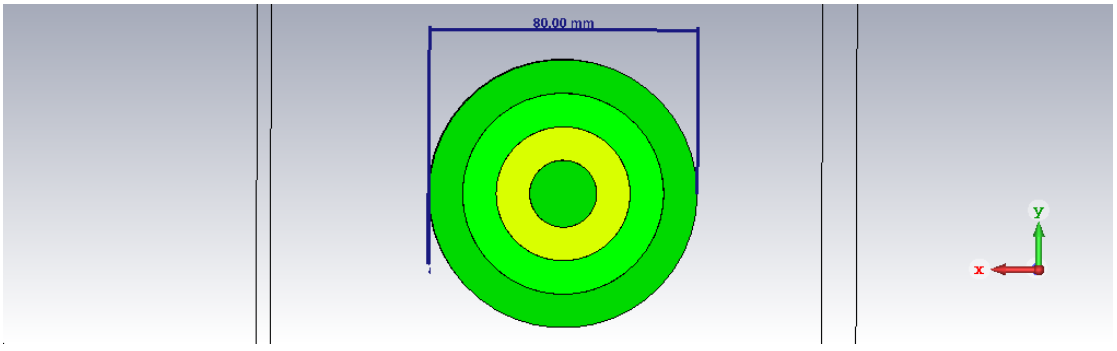

FIGURE 4.5: GRIN lens illustration in CST

As CST has its own field solvers and the beam in the lab is produced by the corrugated horn which is 98% Gaussian, a perfect Gaussian source was used (more details of the Gaussian beam definition in CST can be seen in Chapter 2, 2.6). A Gaussian beam was propagated 155 mm from the lens, to closely match the beam propagating from the corrugated horn in the lab arrangement. Figure 4.6 shows a yz-cut (±85 (mm),0→250 mm) taken of the $\|\mathbf{E}\|$ field.

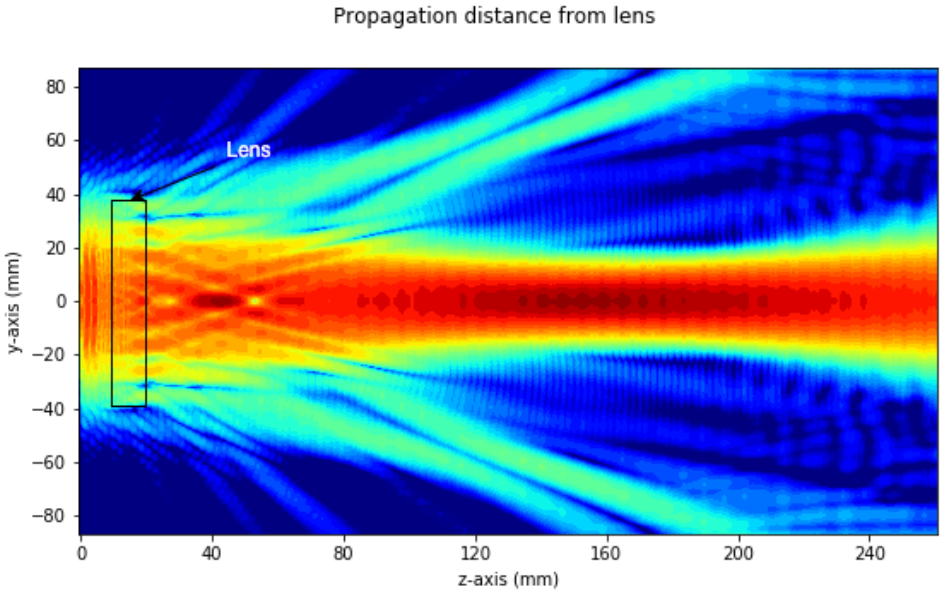

FIGURE 4.6: Beam propagation evaluation plot from CST of the prototype lens with the permittivity variation outlined in Table 4.1.

There is a clear collimation and focus of the beam around 150 mm from the lens, as expected. A transformation of the waves from a planar wavefront into a spherical wavefront can also been seen. The lens simulation in CST validated the design, bringing the collimated incident beam to a focus on the output side as designed. With this verification through simulation, the next step was to manufacture the lens for experimental validation.

4.3 Prototype Lens Manufacturing

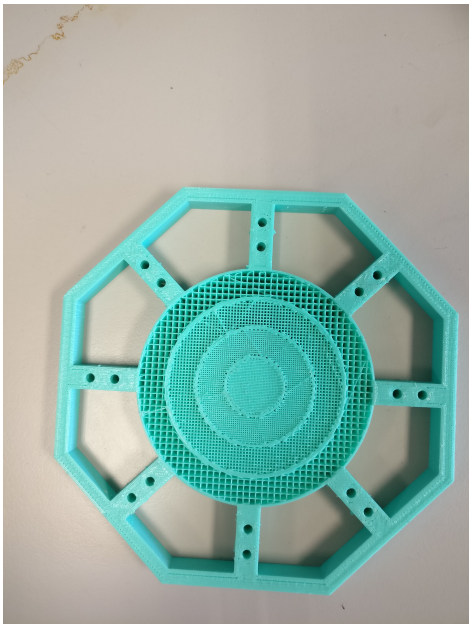

FIGURE 4.7: Image of the four-ring 3D-printed protolens.

To manufacture the lens, the Anet A8+ 3D printer was used. To emulate the permittivity gradient in Table 4.1, a certain PLA-to-air-volume percentage (v) is needed for each ring. The PLA volume percentage indicates the ratio of volume of PLA in the printed structure to the volume of the whole structure. If the maximum and relative permittivity ($\epsilon_{r,max}$ and ϵ_r) are known, the total volume percentage can be found using Equation 4.3 [Kelleher and Goatley, 1955a].

$$v = \frac{\epsilon_r - 1}{\epsilon_{r,max} + 1}. \tag{4.3}$$

The PLA lens has four different PLA-to-volume ratios, shown in Figure 4.7. Equation 4.3 was used to find the volume percentage for each ϵ_r. As the printer is a conventional 3D printer, it uses infill density to describe the ratio of PLA to the total volume. To account for the wall thickness of each ring, we make use of the approach outlined by Zhang [Zhang et al., 2016]. The percentage infill density of each ring is related to the dielectric constant through v. By substituting the

permittivities in Table 4.1 into Equation 4.3 and then using v, the infill density d of each ring can be calculated.

$$d = \frac{v\pi(R^2 - r^2) - 2\pi t(R + r)}{\pi(R^2 - r^2) - 2\pi t(R + r)}, \tag{4.4}$$

where v is the ratio of PLA to air from equation 4.3 and t is the exterior wall thickness set at 1 mm. R and r are the exterior and interior of the cylindrical rings. The infill percentages for the lens can be seen in Table 4.2, along with the other lens parameters.

Ring No.	ϵ_r	Infill percentages	Focal length	Thickness(mm)	Diameter(mm)
1	2.72	80%	100-150	10	80
2	2.34	60%			
3	1.95	40%			
4	1.56	20%			

TABLE 4.2: Test design parameters

4.4 VNA(Vector Network Analyser) Description & Mathematical Model

The VNA lab in Maynooth University has a Rohde and Schwarz ZVA 24 model VNA, which was used for the GRIN lens measurements. The VNA has a base unit frequency range of 10 MHz to 24 GHz. To step up the frequency into the W (75–110GHz) band needed for this project, two Rohde and Schwarz ZVA-Z110 converter model heads were used. All measurements were performed in the W band (75–110GHz).

FIGURE 4.8: Image of the Rohde & Schwarz ZVA –Z110 converter head used.

4.4.1 Measurement System

To test the focusing ability of our lens, a simple algorithm must first be devised in the laboratory. For a basic measurement of a device under test (DUT), there must be at least two components: a source emitter which produces the radiation, and a receiver to collect the radiation and measure the signal. The DUT is considered as any object placed between the emitter and receiver. Figure 4.9 demonstrates a basic emitter–DUT receiver system.

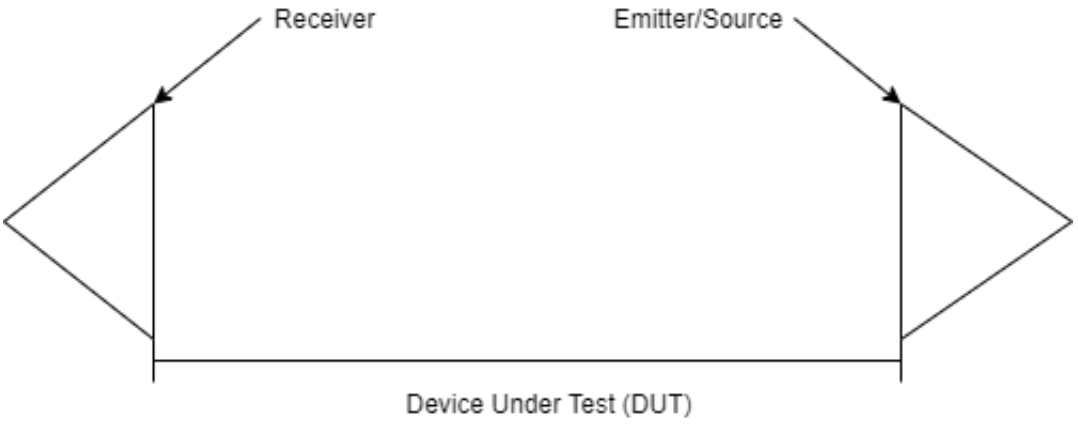

FIGURE 4.9: Schematic diagram of basic-emitter receiver system

4.4.2 Vector Analysis Analyser

The source and the receiver are controlled by a computerised controller that generates the input stimulus and analyses the response from the system.

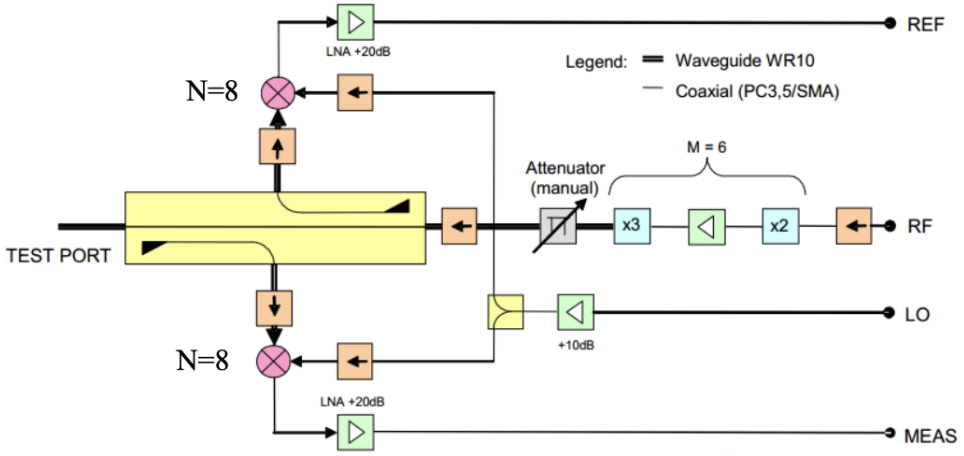

FIGURE 4.10: Internal electronics configuration for the VNA converter head [McLoughlin, 2012]

To use the converter heads, four connections from the VNA are required. Two input signals are needed, a local oscillator (LO) and a radio frequency (RF) signal. The RF signal is the source which will be emitted by the converter head. To increase the frequency so that it is in the W band (75–110GHz), the signal goes through a multiplier network to increase the frequency by a factor of six relative to the original value. There are two output signals from the head back to the VNA, known as the reference out (REF) and the measurement out (Meas). The LO input is used to lower the measurement frequency and the reference signal down to a lower frequency so that they can be analysed by the VNA. This provides the VNA with both a reference signal and a measurement for comparison. For these results to be accurate, they must also be calibrated before measurements are taken. Calibration must be done prior to measurements to ensure that the VNA can accurately measure the loss in signal through the system. The phase of the wavefront can also be measured by the VNA. The calibration also allows the

system to measure the phase and magnitude through reflection via the emitter head. Any port can act as an emitter or receiver. This means that the magnitude and phase can be measured for both reflections and transmissions.

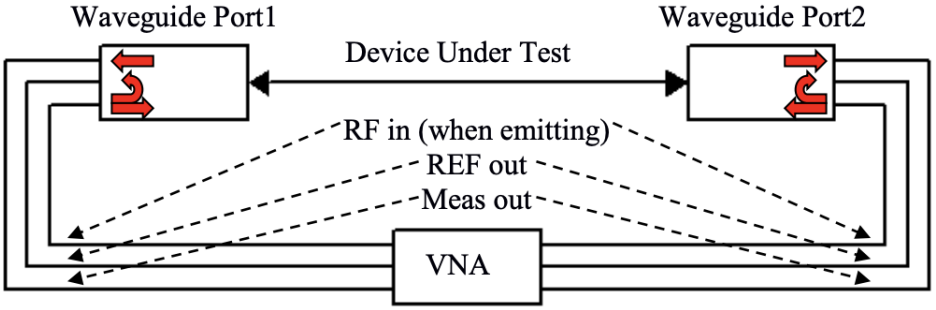

FIGURE 4.11: Schematic of the emitter and receiver connected to the Vector Network Analyser (VNA). [Tynan, 2016]

4.4.3 Feed Horn

In order to launch a signal in free space, an antenna is needed to guide the radiation to its source. To collimate the output field E and to match to the impedance of free space, a horn is best suited. The feed horn chosen is a corrugated horn optimised for 94 GHz manufactured by Thomas Keating Ltd, which is fed by a WR-10 waveguide port on head 1. This waveguide has a rectangular aperture, 2.54×1.27 mm, which allows the fundamental TE_{10} mode to propagate only in this frequency range. The horn operates across the whole W-band frequency (75–110 GHz) containing the fundamental TE_{10} mode (single moded). The rectangular waveguide transitions into a circular corrugated horn structure.

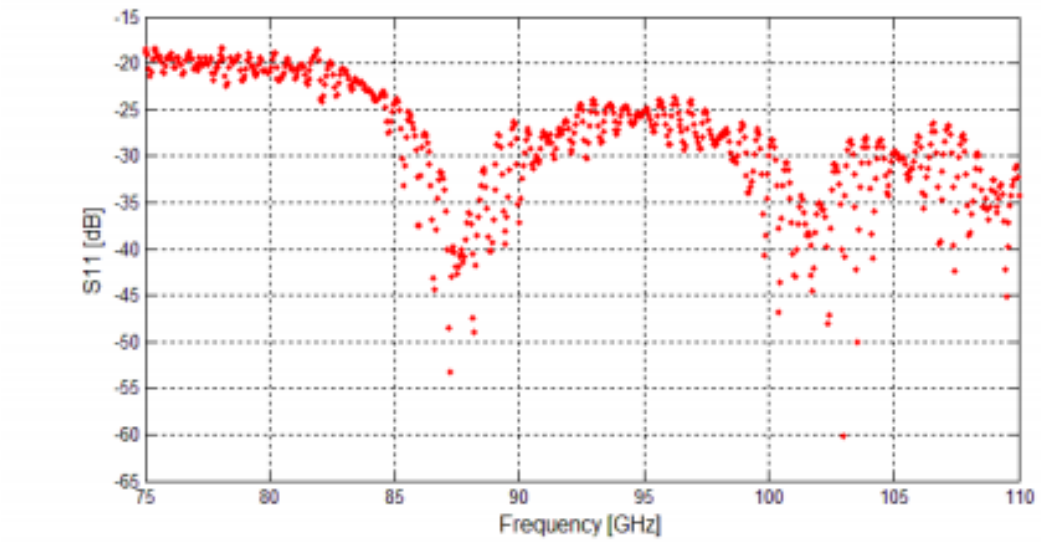

FIGURE 4.12: Plot of S_{11} power received by the horn from internal reflections. The horn performs best at higher frequencies.[Tynan, 2016]

4.4.4 Receiver Port

To couple the output signal to the receiver a truncated WR-10 waveguide with 1 mm wall thickness was used as a receiver probe. The length of probe including the flange was 12.5 mm. Once the receiver port aperture and the feed horn waveguide aperture are aligned the measurement is 100% co-polar. This achieves maximum coupling between the receiver and the emitter. Figure 4.13 shows the new schematic diagram with the receiver port and emitter horn now in the system. Both of these components were added post-calibration, so they are considered DUTs. This means that their effects must be tested and calibrated out in post-analysis.

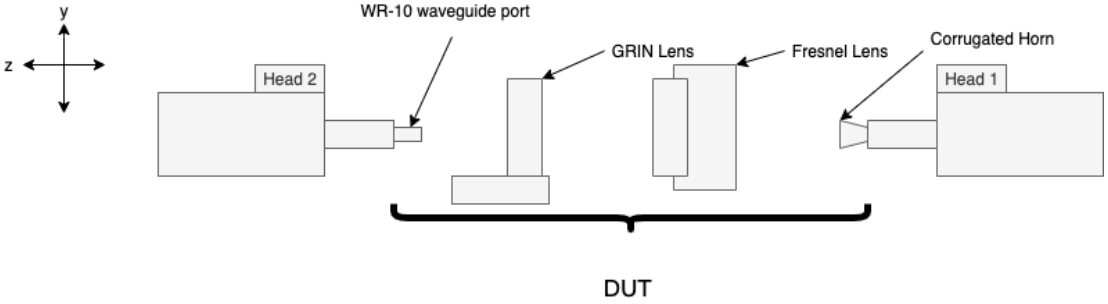

FIGURE 4.13: Schematic of the emitter and receiver with all of the DUT components to be tested.

4.4.5 Device Under Test

For our setup, the main component was the GRIN lens, but as previously stated the emitter horn, receiver port, and Fresnel lens must also be accounted for in our measurements. The GRIN lens was mounted on a rotational stage to allow for rotation and alignment with the phase front of the emitter horn. Moreover, in order to achieve proper alignment of the GRIN lens with the system, the lens holder was fitted with two transitional Zaber stages, which allow for movement on the horizontal and vertical axes. This allowed full movement of the lens for precise alignment with the emitter and receiver.

4.4.6 Lens Mounting

The lens was mounted on a custom 3D-printed circular mount, which can be seen in Figure 4.14. This same mount was also used to hold the PLA samples for Section 4.5.2. The lenses/samples were fixed in place with four small bolts screwed into the corners of the holder.

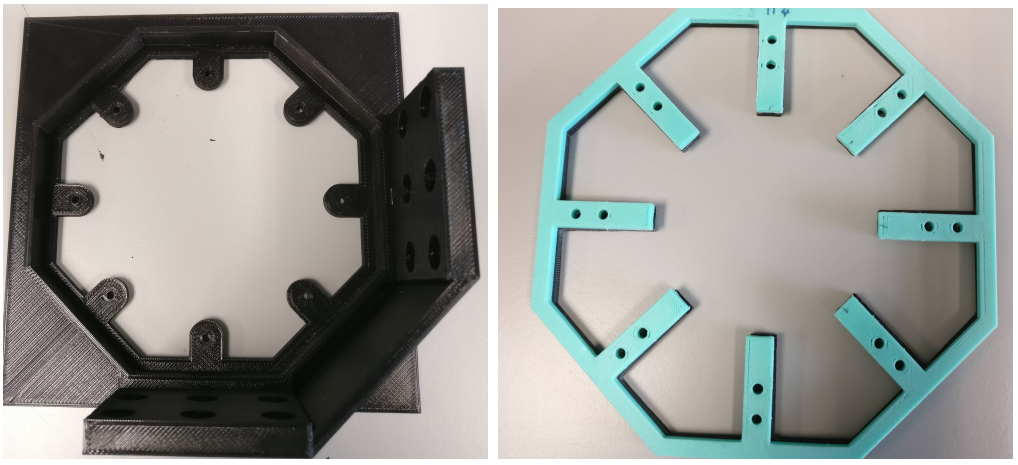

(a) 3D printed lens holder (b) PLA sample holder

FIGURE 4.14: Images of the 3D printed lens holder and sample holder.

4.4.7 VNA Interface

All the measurements in the laboratory used a four-axis NIPCI-7334 motion controller as the control communication point in order to provide commands and collect responses between the computer and motors which controlled the motion stages. The main motion controls were operated through the Zaber console program. To control the scanning patterns, a program written by Dr Gradziel in Labview was used. This allowed for control of the four different axes through communication with the VNA. It also allowed for automated measurements with the VNA over a number of different frequencies. The range and step size for each axis can be specified independently. The user specifies the bandwidth and calibration file, along with other variables such as the extension head type. The user must also identify positions and offsets of each axis in the system and define their axis number. All of this information is available to the user live on the Zaber console. Once the axes are assigned, the scanning pattern start and stop position and number of steps are chosen. This is done using the 'Sweep repeats' and 'Sweep core' settings seen in Figure 4.15. These settings are used to determine the exact

scanning to be defined by the user. At the end of the scan results are saved in user defined file and save-path.

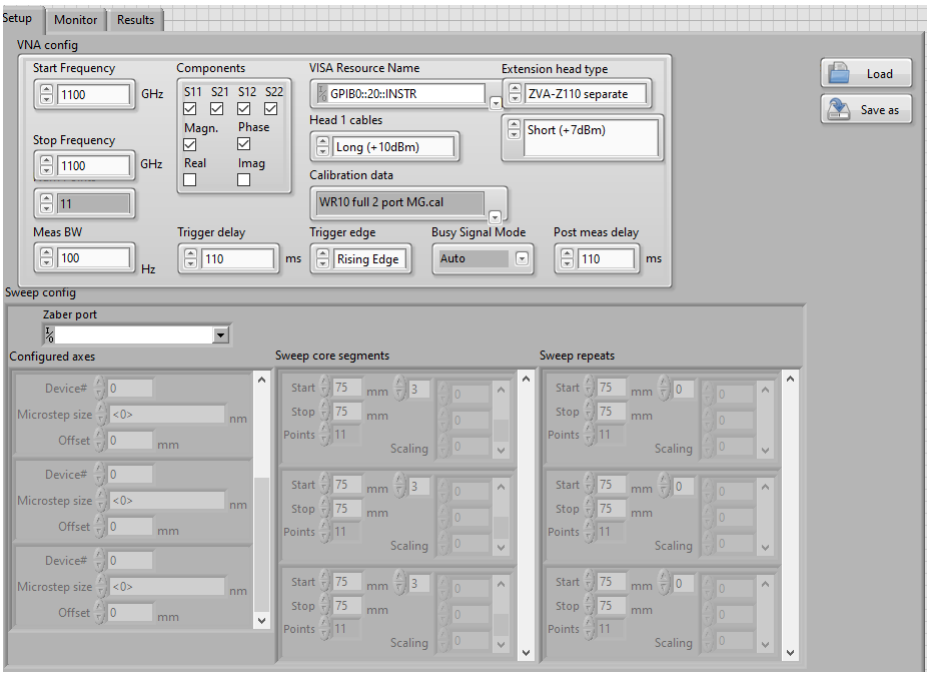

FIGURE 4.15: The main setup view for measurements in the Labview program. A start and stop frequency are set, along with a number of points to take between these two values for our range of frequencies. The measurement bandwidth is set and a calibration file chosen. The S parameters for the measurement are selected. Finally the scan pattern, number of axes, and range and step size for each axis are set.

4.4.8 Scanning Control System

Depending on the DUT and the measurement in question, several scanning patterns were employed, which will be outlined below. Each of these scanning patterns had an additional SW (standing wave [Gradziel and Trappe, 2018]) filter applied to it, which required each component to scan concurrently on the z-axis over a range of ±4 mm in steps of 0.4 mm and the DUT and head 2 to scan concurrently over the x-axis over a range of ±4 mm in steps of 0.4 mm:

1. Scanning pattern 1 : This scanning pattern was developed to locate the focus of the GRIN lens (as described in Section 4.4.11.1). The receiver port was

mounted on three different Zaber tracks with freedom of movement on all three axes. To find the focus, a 'zigzag' scanning pattern in the xz-plane was implemented. On top of this scanning pattern, an additional SW filter scan was employed. This required an additional linear scanning pattern, which employed motion in all three z-axes of the lens holder, receiver port, and horn concurrently. The effective range of the Zaber console mounted on the z-axis was 150 mm, on the y-axis 450 mm, and the x-axis 450 mm. These were the tracking constraints of the probe. The z-stage of the lens holder had a range of 14 mm.

2. Scanning pattern 2 : This pattern was used to take x-cuts at the focus of the lens, once it had been found. Only a linear cut ± 30 mm, in steps of 3 mm, was employed here. The same SW pattern was also implemented here.

3. Scanning pattern 3 : To test the PLA samples, only the reflection coefficients were needed, so a simple linear pattern was chosen. This meant the effective range on the z-axis was 450 mm for the receiver and port. This scanning patten only used the SW scan pattern outlined to calculate the scatter coefficients.

4.4.9 Scatter Matrix

Each parameter below represents a different variable that can be measured from the port or horn:

- S_{11} is the reflection measured at the waveguide probe.
- S_{22} is the reflection measured at the input feed horn.
- S_{12} is the transmission from the feed horn input to the waveguide probe. 0 dB represents a perfect throughput and coupling.

- S_{21} is the transmission from the waveguide probe to the feed horn input. Again 0 dB represents perfect coupling.

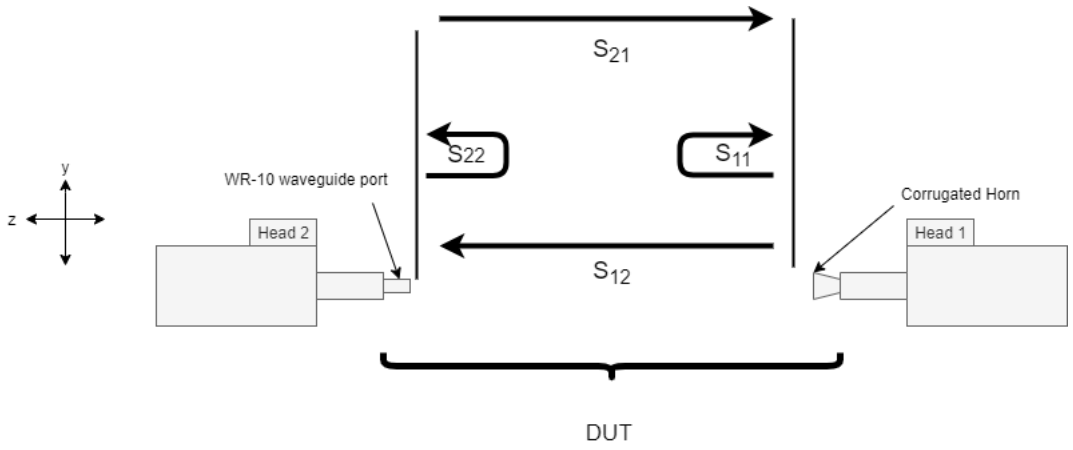

FIGURE 4.16: Demonstration of the four scattering coefficients in a two-port system with an emission horn aperture, DUT, and receiver.

4.4.10 Calibration

FIGURE 4.17: Image of the R&S ZV-WR10 calibration kit used to calibrate the two ZVA-Z110 heads

The VNA was calibrated explicitly for each frequency in the W band in steps of 100 MHz, which is the standard range and step size used for calibration. This sampling rate was chosen for good accuracy in our measurements. The system was calibrated using the standard UOSM (unknown, offset, short, match [Wong, 2004]) technique, which used the commercial WR-10 calibration kit in the lab. Through measurements compared the emitted beam to the signal received from head 2. The short measurement compared the reflection from heads 1 and 2 separately with a short attached. The emitter horn and receiver port are not included in this system calibration, as they are part of the DUT.

4.4.11 Alignment

To minimise any offsets and tilts with respect to the stationary horn, an optical alignment process was employed. Firstly, the components were geometrically aligned by eye, ensuring any residual tilts and offsets would be small. Once this had been achieved, a more precise approach was taken. This process is outlined below.

4.4.11.1 Initial Alignment & Transitional Stage Setup

Scanning patterns 1, 2, and 3 needed three different optical arrangements and mounting designs on the bench. Each component outlined below was mounted and levelled using a T-square with a level attached to it.

Scanning patterns 1 and 2 required movement in the z- and x-axis for the receiver probe, so only two stages were needed. The z-stage was mounted to the bench first. To the z-stage, a second Zaber stage was mounted in the x-axis. This allowed for scanning in the x-axis. To this x-stage, a y-axis stage was added. To this stage, head 2 and the receiver were mounted. The DUT was mounted on top of two

FIGURE 4.18: Image depicting the different stages and optical bench setup for scans 1 and 2. Here we see the emitter mounted on three Zaber stages (x-, y-, z-axis), the DUT mounted to a rotational stage, and the two Zaber stages described in the text.

smaller range stages for movement in the x- and z-axis, as well as a rotational stage to account for any tilting seen during calibration. Finally, the emitter horn was mounted to one stage on the z-plane which had been mounted to the optical bench. The head and horn were screwed into a custom 3D-printed holder, which fit the head precisely. This z-stage is required for scanning in the z-axis for the SW filter. Scanning pattern 3 required z-stages only for the receiver and emitter. The receiver no longer used the same probe from scanning patterns 1 and 2. It was switched out and fitted with a horn identical to the emitter horn. The lens holder had the same setup as described above. However, an additional 3D-printed skeleton was printed to hold the PLA samples in place, which can be seen in Figure 4.14.

4.4.11.2 Alignment Procedure

To ensure the receiver, samples (or lenses), and emitter horn were all fully aligned, a scan using scanning pattern 1 was taken. To perform the scan, the lenses (or

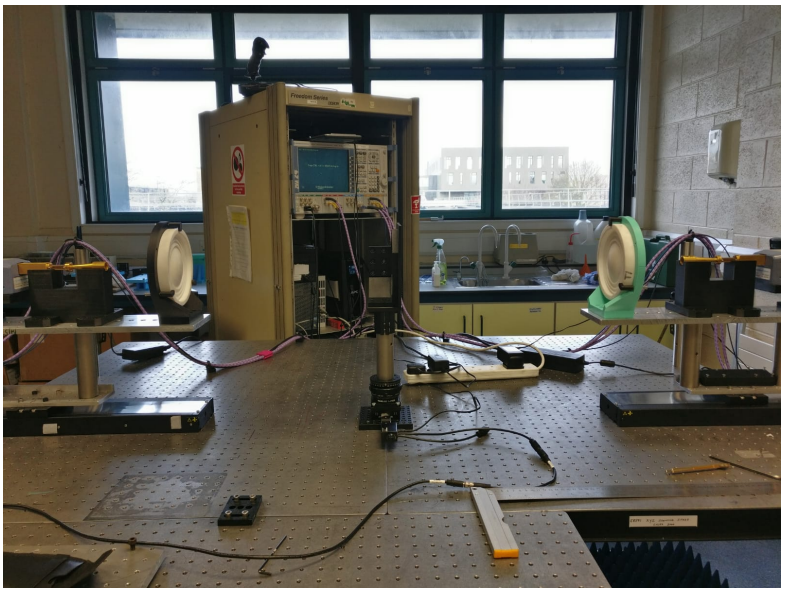

FIGURE 4.19: Image depicting the different stages and optical bench setup for scan 3. Here we see the emitter and receiver mounted on two Zaber stages, the DUT mounted to a rotational stage, and the two Zaber stages described in the text.

samples) were replaced with an aluminium plate, 130 mm in diameter, with a 10 mm diameter hole at the centre. A scan was run using scanning pattern 1, and the results were analysed using a script written in a *Jupyter Notebook* by Dr Marcin Gradziel. Using this program, the S_{12} intensity was checked for offsets (beam off-axis). The beam pattern should be centred around 0 if no offset is seen. If the beam pattern is not symmetrical around 0, the DUT is misaligned. An example of this can be seen in Figure 4.20.

The offset was recorded and accounted for thereafter by moving the Zaber console mounted to the DUT to correct for the misalignment. The phase of the S_{12} was also used to check whether the DUT was tilted. If the phase is flat with no gradient, the DUT has no tilt with respect to the heads. If there is a negative gradient, the DUT is rotated clockwise. If the gradient is positive, the DUT is rotated anticlockwise. Once the phase was flat and the beam pattern offset was centred, the system was considered optically aligned.

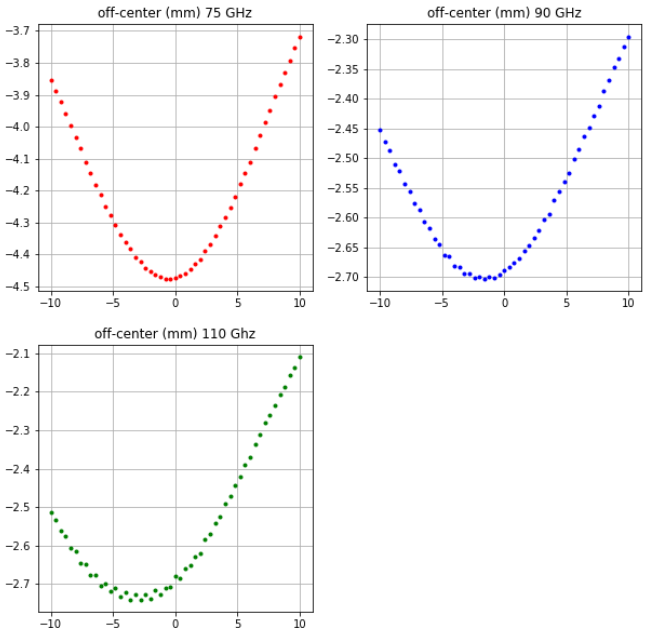

FIGURE 4.20: S_{12} values for 75GHz,100GHz and 110GHz. Here we see each beam misaligned by 2–3 mm from the central axis

4.4.11.3 Through & Reflection Standard

Once calibration was complete, a reflection and through standard were taken. These standards are needed for normalisation of the scatter parameters post-measurement if required. To measure the reflection standards, a polished aluminium plate was placed in the lens holder, and scanning pattern 3 was run. The S_{11} and S_{22} scattering parameters were then used for normalisation of later results. For the through standard, the same scanning was employed, except that the aluminium plate was removed. The S_{12} and S_{21} scatter parameters were then used for normalisation in the post-measurement stage.

FIGURE 4.21: Circular aluminium plate with a diameter of 130 mm and a 10 mm hole in the centre, used for beam alignment

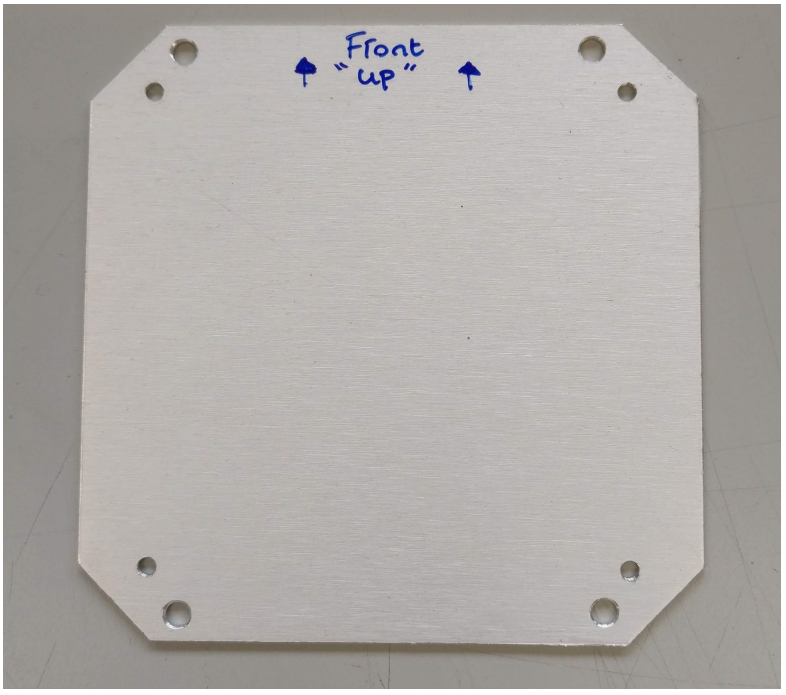

FIGURE 4.22: Image of the polished aluminium reflection plate used for through standard.

4.4.12 GBMA of GRIN Lens

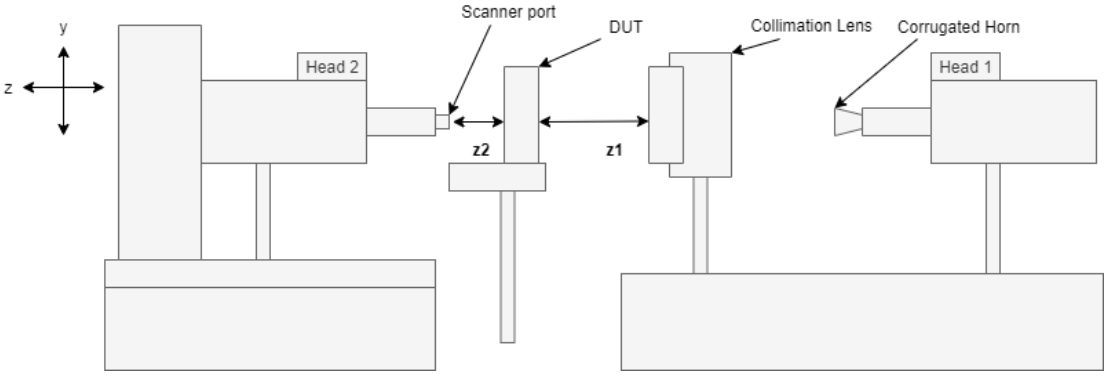

FIGURE 4.23: Schematic diagram of the full optical bench used to measure the lens outputs.

The emitter horn on head 1 creates an EM field at the aperture of the horn, which ideally (this may not be achieved over the full frequency band) is in the following form [Goldsmith, 1998]:

$$E(r) = J_0(\frac{2.405r}{a}) \exp{(\frac{-j\pi r^2}{\lambda R_h})}\hat{y}, \tag{4.5}$$

where J_0 is the Bessel function of zeroth order, 2.405 is the first zero of J_0, r is the radial distance in the horn, R_h is the horn slant length and a is the radius of the horn aperture 7.14mm (for the corrugated horn used).

Situated 125 mm from the horn is a lens holder which was designed in-house, with a Fresnel lens, also designed in Maynooth, placed here to collimate the incoming beam from the horn. To simulate this lens mathematically, the thin lens approximation was used here. From the lens to the GRIN lens, there is a distance of z_1, as seen in Figure 4.23; this distance is set at 471 mm. The distance z_2 is the distance from the centre of the GRIN lens to the scanning probe on head 2. This distance varied throughout the experiment. Finally, if we model all of the optical components in an ABCD matrix using Equations 2.37 and 2.35, we achieve the following equation:

$$JJ = dz_2 \cdot refr_2 \cdot dz_1 \cdot refr_1 \cdot dz, \tag{4.6}$$

where dz, dz_1 and dz_2 are ABCD matrices corresponding to propagation by all free space distances of the beam between the horn and Fresnel lens, the Fresnel lens and the GRIN lens and the GRIN lens and the probe, respectively. $refr_1$ and $refr_2$ are ABCD matrices corresponding to the focal lengths caused by the Fresnel lens and the GRIN lens.

Gaussian beam analysis can be used to accurately predict the behaviour of the beam within the optical train. Due to the fact that the system is cylindrically symmetric, Laguerre-Gaussian (LG) modes can be used to describe the beam from the corrugated horn. Through the manipulation of various permittivity distributions, a GRIN lens takes the original spherical waveform and transforms it into a collimated beam within a maximum distance z_R, the confocal distance [Qi et al., 2015].

To achieve a good description of the evolution of the beam, an evaluation of a diffraction integral with a large number of points would be required. However, as mentioned previously, this is computationally intensive, and is unstable when z $\rightarrow$ 0. To describe an accurate model of the beam propagation, a GMBA approach was taken, as this requires less computational power and is stable as z $\rightarrow$ 0. To describe the $\|E\|$ field at the corrugated horn aperture, we rewrite the electric field in terms of a Gaussian beam mode set given as:

$$\Psi_n(r,z) = \frac{1}{w(z)}\sqrt{\frac{2}{\pi}} L_n\left(\frac{2r^2}{w(z)^2}\right) \exp\left(-\frac{r^2}{w(z)^2}\right) \exp\left(-jk\left(\frac{r^2}{2R(z)}\right)\right) \times \exp(-jkz)\exp(j(2n+1))\Delta\phi_{00}(z)$$

All of the above terms have been described in Section 2.1 of Chapter 2. The mode coefficients to represent the horn field are calculated using the overlap integral of E; the field value (electric field from horn aperture) is seen in Equation 4.7. To represent the full electric field, the wave function must be integrated over the entire aperture of the horn, between $a = 0$ and $a =$ horn aperture radius.

$$A_n = \iint \Psi_n \left(r, z_0\right), w\left(z_0\right), R\left(z_0\right)\right) E\left(r, z_0\right) r dr d\phi, \tag{4.7}$$

$$A_n = \frac{\int_0^{ap} J_0(\exp^{\frac{-j\pi r^2}{\lambda R_n}}) L_0 exp^{\frac{-r^2}{w^2}} \exp^{\frac{j\pi r^2}{\lambda R}} 2\pi r}{(\int_0^{ap}\int_0^{ap} J_0^2 L_0 exp^{\frac{-r^2}{w^2}})^{0.5}}. \tag{4.8}$$

The value of ω was chosen to maximise power in the fundamental mode, in that $\omega = 0.6435a$, where a is the horn aperture. This can be seen in Table 4.3, where 98% of the power is in the fundamental mode which can be seen in the second column (A^2).

Mode number	$\|A_n\|$	$\|A_n^2\|$
0	0.99	0.98
1	0	0
2	0.12	0.01
3	0.04	0
4	0.02	0
5	0.03	0
6	0.02	0
7	0	0
8	0.01	0
9	0.02	0
10	0.01	0
11	0	0
12	0	0
13	0.01	0
14	0.01	0
15	0.01	0
16	0	0
17	0	0
18	0	0
19	0.01	0

TABLE 4.3: Table of mode coefficients for the first 20 Laguerre-Gaussian

This GBMA approach gives a reproduction of the horn aperture field model which couples efficiently (98%) to the equivalent Gaussian beam. Then, using these coefficients, the electric field from the horn aperture can be calculated with Equation 4.9, by summing over all of the mode coefficients at any other xy planes in the system. The scale of the beam evolves according to ω_z, R, and phase slippage ϕ.

$$E(r) = \sum_{i=0}^{modenumber-1} \sqrt{\frac{2}{\pi\omega_{out}^2}} A_{nn}(i) L_i(x) \exp\left(i((2i+1)\phi) - \frac{ikr^2}{2R(z)}\right), \quad (4.9)$$

where $x = 2(\frac{r}{\omega_{out}})^2 \exp^{-(\frac{r}{\omega_{out}})^2}$.

To more accurately describe r, a reasonable number of modes are needed. Table 4.3 lists the first 20 mode coefficients which are being summed over to model the aperture field. Figure 4.24 shows the number of beam modes that will best represent the aperture field. 20 modes best describe the propagation of the scalar horn field in this analysis. With the aperture field defined, the corresponding ABCD matrix could now be set up to analyse the beam launched from the corrugated horn through the GRIN lens and simulate the lab measurement facility. Any lens in the optical system was considered a 'thin lens', the thin lens approximation was used, and Equation 4.6 was formed.

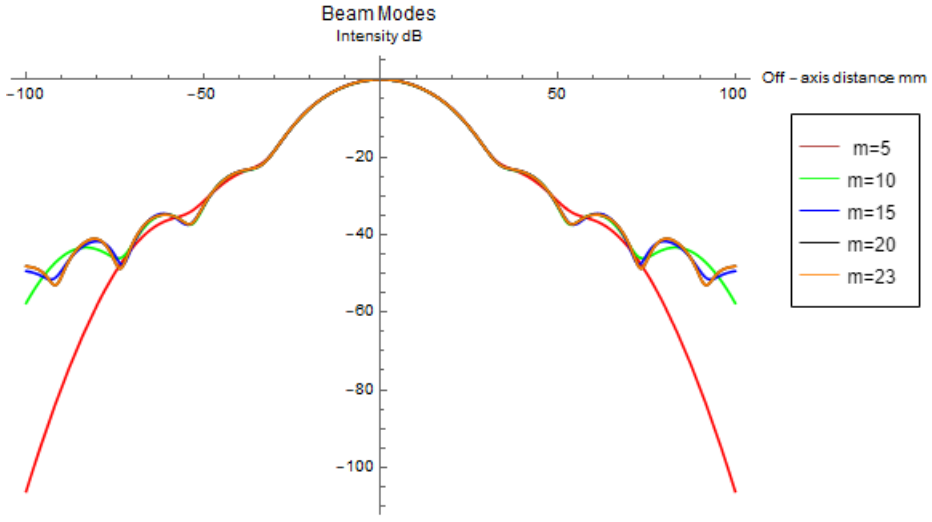

FIGURE 4.24: Summation of 5,10,15 and 20 beam modes to represent the electric field at the horn aperture

Using equations 2.33 and 2.32 the output beam radius at a desired distance could be calculated and inserted into Equation 4.9 to calculate the desired field profile at this point.

A script was written on *Mathematica* to model the lab arrangement (100 GHz example here), with the following variables: $\lambda = \frac{2.99710^{11}}{100\times10^{9}}$, $Radius = 78$, $k = \frac{2\pi}{\lambda}$, $aper = 7.1345$, $modenum = 20$ (units of mm assumed). For a corrugated horn a beam radius is calculated from

$$\omega = 0.6435 \times a, \tag{4.10}$$

where a is the aperture radius, ω maximises power in the fundamental mode and requires the lowest number of modes to accurately describe the field. Therefore the input beam radius of the horn is $7.1345 \times 0.6435a$.

4.5 Protolens Lab Measurements

To test the theory that a 3D-printed lens could actually have the desired effect and focus a beam within the laboratory setup outlined in Section 4.4.12, a prototype lens was designed and printed as a benchmark test case, as described in Section 4.2. A prototype was designed to test the operation of a GRIN lens with a simple refractive index gradient. In Table 4.2, the design parameters of this lens can be seen.

Once the optical components described in Figure 4.23 were centred, the prototype lens was placed in the lens holder. This optical arrangement was then measured as a proof of concept to see if a GRIN lens could focus a 100 GHz beam. The lens in question was 80 mm in diameter and 10 mm in thickness, as shown in Figure 4.2.

4.5.1 Measurements

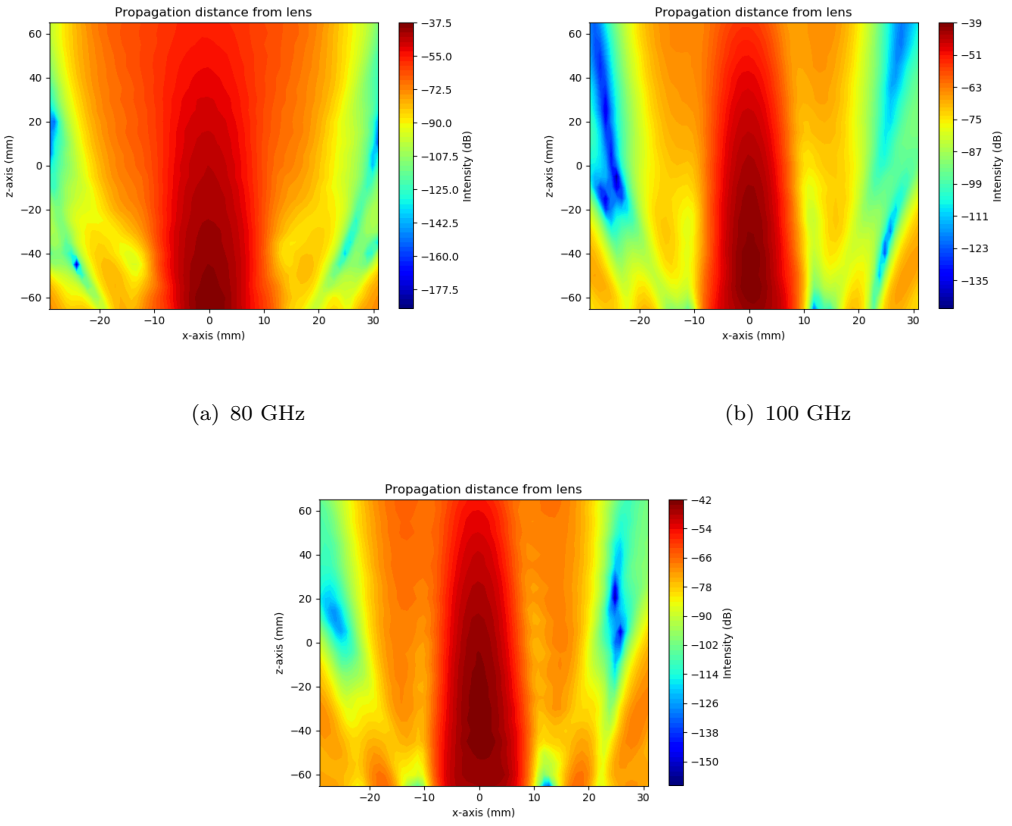

(a) 80 GHz

(b) 100 GHz

(c) 110GHz

FIGURE 4.25: Preliminary focus of the proto-type lens. The nominal position of (0,0) is set at 150 mm from the GRIN lens

To find the focus of the beam, scanning pattern 1 was used. The nominal position of the probe z_2 was set at 150 mm. Figure 4.25 shows the beam as it propagated from the lens. The nominal position at (0,0) was 150 mm from the GRIN lens. At 80 GHz the beam waist was -60 mm from the nominal position. At 100 GHz the focus of the beam was -50 mm from the nominal position. Finally, at 110 GHz the beam was -30 mm from the nominal position. The prototype lens demonstrated the focusing effect of the lens, which showed some variations across the different frequencies. This variation was expected; however, the beam did not focus 150 mm from the lens as expected. Some assumptions were made in the design of the lens (e.g. the relative permittivity of 100% infill PLA) that were tested further.

4.5.2 PLA Testing

To design a better, more accurate GRIN lens, the relationship between infill percentage and permittivity was tested to estimate the actual dielectric constant values at 100 GHz of the 3D printed infill fractions. To do this, four PLA samples of varying infill percentages were printed, as seen in Figure 4.26. These PLA samples had an average thickness of 3 mm. To measure the thickness of each infill, a micrometer with a precision of ±0.001 mm was used to measure each sample in eight evenly spaced steps around the perimeter of the lens. These values were then averaged. The precision of ±0.001 mm was needed because permittivity has an exponential dependence on the thickness $T^2 \approx \epsilon_r$. The average thickness of each sample is outlined in Table 4.4.

Infill Percentage %	**Average Thickness** (±.001 **mm**)
100	2.997
75	2.797
50	2.762
25	2.634

TABLE 4.4: Infill percentages and sample thickness

The thickness in Table 4.4 shows a small difference from sample to sample. This directly relates to the precision achieved by the extrusion head of the 3D printer, which is 0.4 mm, as seen in Section 1 of Chapter 1.4.1. In addition to the variations across different samples, there were also thickness variations across the samples themselves. These differences could be attributed to slight variations in cooling rates across the printing bed during the printing process.

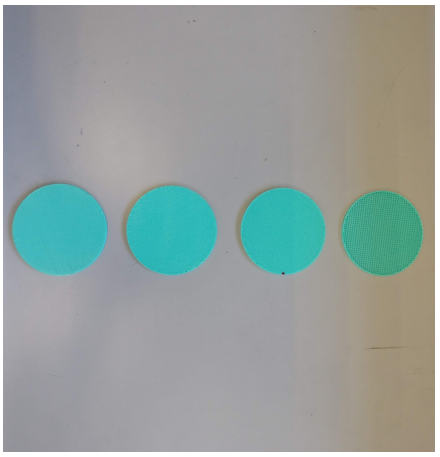

FIGURE 4.26: From left to right: 100%, 75%, 50% and 25% infill samples

It is also interesting to note that the 'back' and 'front' of each sample have some minor surface defects due to the nature of the printing. As one of the faces sits on the glass printer bed, it is more homogeneous when compared with the face of the sample that faces the extruder. With this in mind, two separate scans were taken for each sample.

4.5.3 PLA Measurements

To determine the permittivity of a sample, several variables must first be defined. The reflection coefficients S_{11} and S_{22} are not directly related to permittivity. The propagation factor tells us how a wave propagates through the defined material [Weir, 1974]:

$$P = \exp^{\gamma t} = \exp -(\alpha + i\beta)t, \tag{4.11}$$

where γ is the propagation constant, α is the attenuation constant and β is the phase constant. The reflection coefficient Γ at the interface between the air and the DUT can be found using S_{11} and S_{22} for a sample of thickness t.

$$\Gamma = \chi \pm \sqrt{\chi^2 - 1}, \tag{4.12}$$

where

$$\chi = \frac{S_{11}^2 - S_{21}^2 + 1}{2S_{11}}. \tag{4.13}$$

The propagation factor can then be found from P:

$$P = \frac{(S_{11} + S_{21}) - \Gamma}{1 - (S_{11} + S_{21})\,\Gamma}. \tag{4.14}$$

Using Equation 4.15 from [Kim and Baker-Jarvis, 2014], a fitting function was designed to determine the permittivity of each sample :

$$\epsilon_r = \frac{\lambda_0^2}{\mu_r}(\frac{1}{\Lambda^2} + \frac{1}{\Lambda_c^2}), \tag{4.15}$$

$$\frac{1}{\Lambda^2} = -[\frac{1}{2\pi t} ln(\frac{1}{P})]^2, \tag{4.16}$$

where Λ_0 is the free-space wavelength, t is the thickness of the sample, μ_r is the relative permeability and Λ_c is the cutoff wavelength of the horn. ϵ_r was the only variable in the equation, the other parameters were kept constant.

To measure the permittivity, the Nicolson–Ross–Weir (NRW) method [Kim and Baker-Jarvis, 2014] was used. The optical bench had a similar setup to the proto-lens measurements, except that the waveguide probe antenna on head 2 was replaced with another horn. An image of the lab setup was included as part of scanning pattern 3, from Section 4.4.8, and can be seen in Figure 4.19. Figure 4.27 shows a schematic diagram of the optical bench. To find the permittivity of the samples, only the S_{11} and S_{22} scattering parameters were needed, so a simpler 1D scanning pattern in the z direction would suffice. Scanning pattern 3 was used.

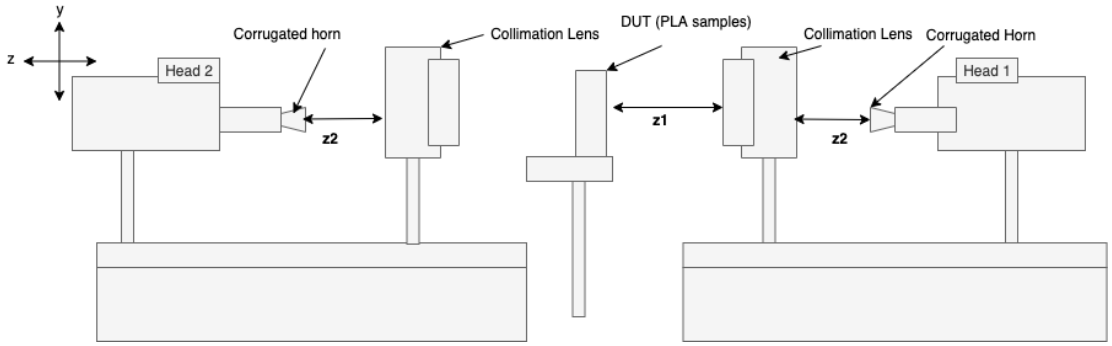

FIGURE 4.27: Schematic diagram of the laboratory stages and optical components. z_1 represents the constant distance between the colliamtions and both horns (125 mm). z_2 represents the scanning distance between the sample and the collimation lens, which is varied for the scan.

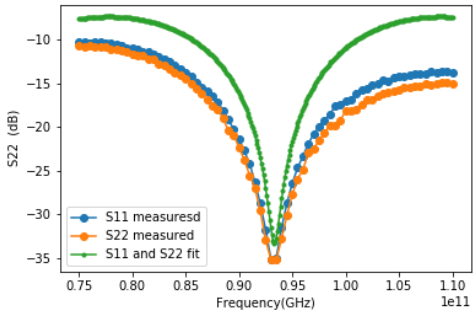

(a) 100% (Front)

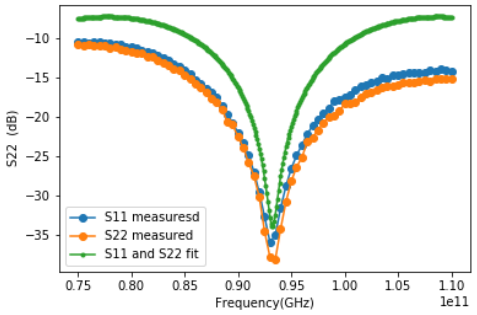

(b) 100% (Back)

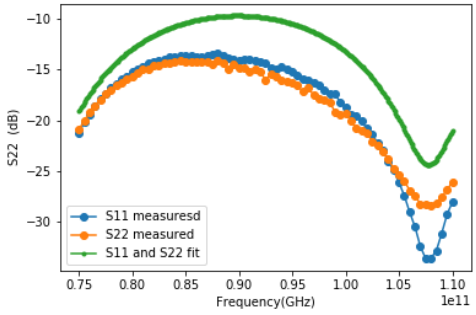

(c) 75% (Front)

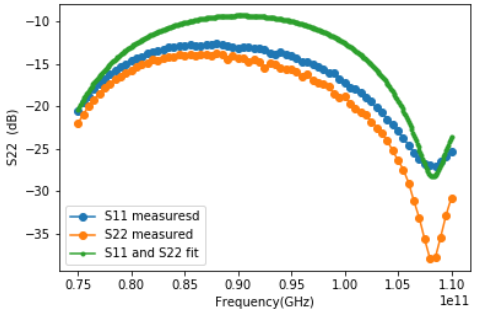

(d) 75% (Back)

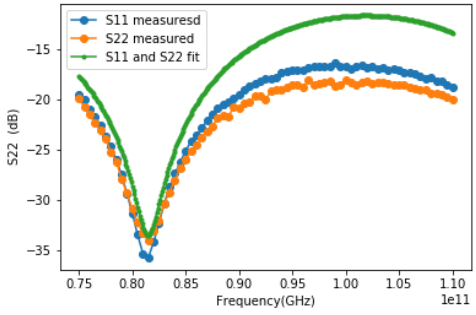

(e) 50% (Front)

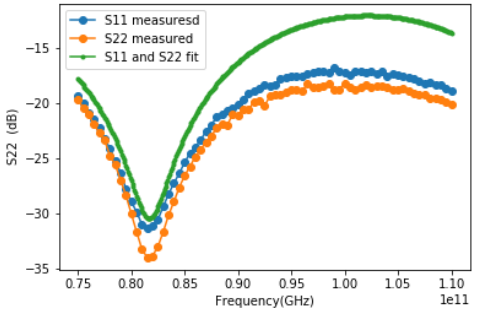

(f) 50% (Back)

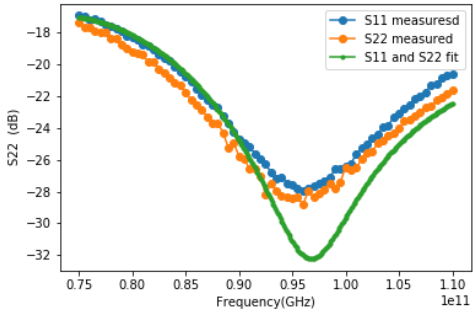

(g) 25% (Front)

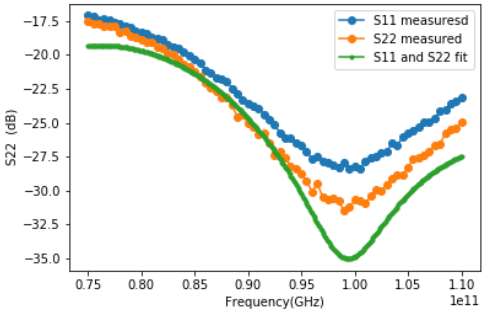

(h) 25% (Back)

FIGURE 4.28: Measured S_{11} and S_{22} data plotted against a fitted function which varies with permittivity(equation 4.15)

To find the permittivity of each sample, S_{11} and S_{22} were plotted as a function of frequency. The measured S values were compared with different ϵ_r from Equation 4.15 to find the best fit with the S_{11} and S_{22} values. Figure 4.28 shows the fits for each sample. Table 4.5 shows the corresponding dielectric permittivity for each infill, derived from these fits. For 100% and 75%, the uncertainty of the thickness was taken as the main error. For 50% to 25% infill, the range across the front and back face of the samples was taken as the uncertainty.

Sample Infill Percentage	**Relative Permittivity**
100%	2.62±.005
75%	2.24±.01
50%	1.73±.025
25%	1.4±.025

TABLE 4.5: Table of improved ϵ_r measurements for different infill percentages at 100 GHz

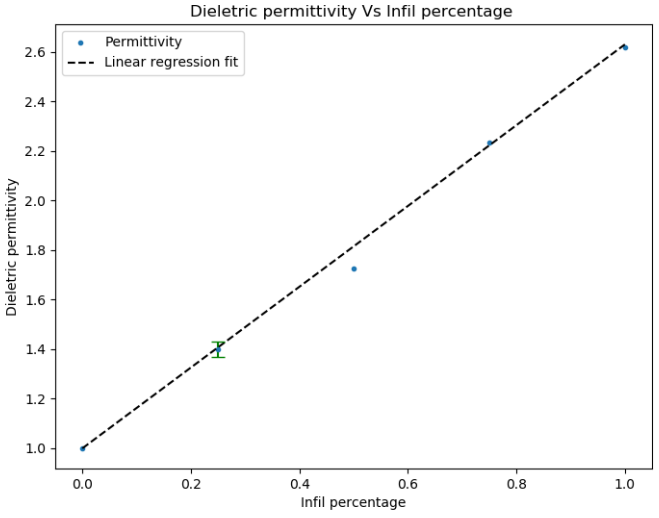

FIGURE 4.29: A linearly fitted graph showing the relationship between the infill of individual samples and their relative permittivities

The infills from Table 4.28 were then plotted against their respective permittivities. From this linear relation, the dielectric permitivities for each infill can be

calculated. Using the estimation above, a new and improved permittivity could be used to the design the final lens in CST.

4.6 Final Lens Design & Manufacturing

For the second design, the lens diameter was larger to receive all incident power with no spill over to make sure the full extent of the beam was received. A diameter of 100 mm and a focal length of 250 mm were chosen, a typical W Band lens design. Like the proto-lens, this lens had a thickness of 10 mm. Once these values where known, the relative permittivities could be found. The final lens was designed after PLA lab tests had determined the PLA infill percentages and the permittivity at 100% PLA. Therefore, $\epsilon_{r,max}$ was a known quantity when designing this lens. The two main differences between the proto-lens and the final design is the diameter and number of annular rings. Figure 4.4 (from Section 4.2) shows how the beam intensity is distributed as a percentage of beam radius. It also shows that 99.997% of the beam is captured if the lens has a radius of $2w$. With the maximum beam radius incident on the GRIN lens known to be 25 mm, a 100 mm diameter should focus all of the incident beam power. Changing the number of rings from four to six should also help focus the beam. In theory, this should improve the focusing capabilities of the lens, due to its closer proximity to a continuous curved surface. An ideal case would be to have a continuous change in permittivity for the entire radius of the lens. However, this is not achievable, so due to external factors such as structural integrity and wavelength size (4 – 2.7mm), a ring radius of 8mm was chosen for this lens design. This also assumes that the entire lens is illuminated and that the beam fills the lens.

To manufacture the lens, much like the prototype lens, Equations 4.3 and 4.4 were used to determine the appropriate infill percentages to focus the beam at 250 mm. The ϵ_r values required to focus the beam are listed in Table 4.6 alongside their

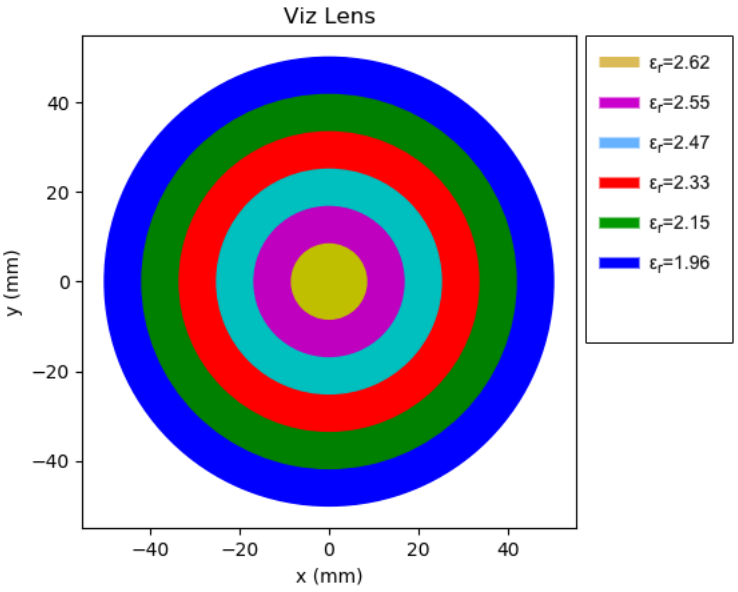

FIGURE 4.30: Visualisation of lens created using *Python*

percentage infills. From Section 4.2, a series of ϵ_r and their corresponding infill percentages were calculated using code written in Python.

Relative permitivity	**Infill percentage**
2.62	100%
2.55	96%
2.47	89%
2.33	80%
2.15	68%
1.96	55%

TABLE 4.6: Table of relative permitivities and their corresponding percentage infills

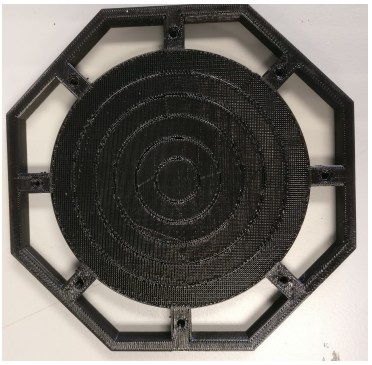

FIGURE 4.31: Image of the final 3D printed lens. The PLA was changed from a green filament to black (same PLA material). This does not affect the dielectric proprieties of the lens.

4.7 Final Lens CST and ABCD Simulations

Cuts were taken at 0 mm, 200 mm, 250 mm, and 500 mm to examine the propagation of the beam profile. Figure 4.32 shows the different beam intensities along the axis of propagation of the beam, predicted using the ABCD matrix. Figure 4.32(c) shows the intensity of the beam at the focus. It has a waist value of 10.4 mm and a radius of curvature of 17.9 m, which is predicted from GBMA. With such a large R value, the phase front can be considered flat at this point. This is the expected behaviour of the beam at focus according to Goldsmith [Goldsmith, 1998]. The beam stays collimated ± 113mm from the focus, which was calculated using Equation 2.1.3, until finally it hits z_c, where its radius of curvature is at a minimum of 226 mm. At this point ω has grown to 14.7 mm. Figure 4.32 (c) is another cut taken from inside z_c; as expected, the beam radius has not diverged much from ω_0 at this point (ω= 11.38 mm, R = 303 mm). Figure 4.32 (a) and (d) were both taken in the far-field of the beam where $z > z_c$. Here the beam is no longer collimated and side lobes become more prominent.

4.7.1 Beam Normalisation

To compare the CST data, lab data and ABCD adata, the on-axis intensities where all normalised to 1. The CST data which represents a Gaussian field source has already been normalised to unity in CST. When we compare this to the horn field represented by a truncated Bessel field, we see a difference in beam widths between the Gaussian beam and truncated Bessel. This discrepancy is represented in Figure 4.34 below. The Gaussian beam and the truncated Bessel field both are normalised to contain unity power in Figure 4.33 and the on axis values vary by a factor of ≈ 1.3. Here the beam widths agree closely. When both on axis beams are normalised to 1, the beam widths are seen to differ with the Gaussian being more narrow. In Figure 4.33 both beams contain unity power and so have different on-axis values.

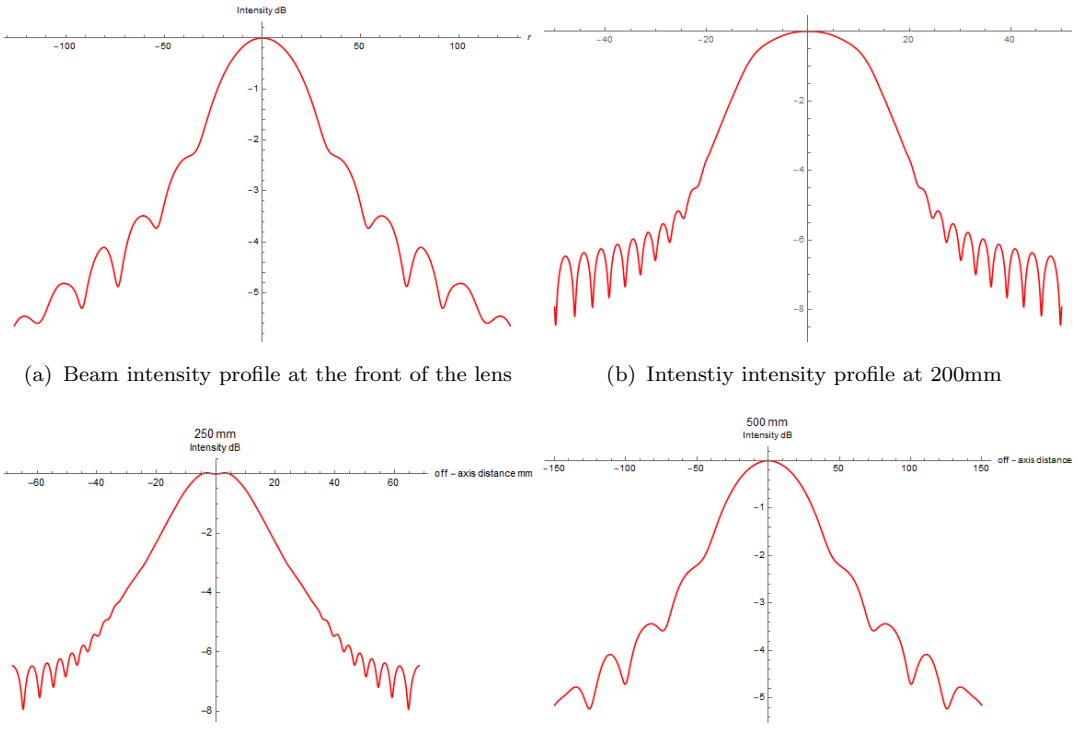

(a) Beam intensity profile at the front of the lens

(b) Intenstiy intensity profile at 200mm

(c) Beam intensity profile at 250mm

(d) Beam Intenstiy profile at 500 mm

FIGURE 4.32: Beam Intensity profiles of the beam as it leaves the GRIN lens predicted by the ABCD matrix

In this plot the beam widths are comparable but if both beams are normalised on-axis to 1 the Gaussian looks thinner than the truncated Bessel intensity. This is an artefact of the normalisation as opposed to the beams not having equal beam radii. This is important to consider when comparing subsequent plots.

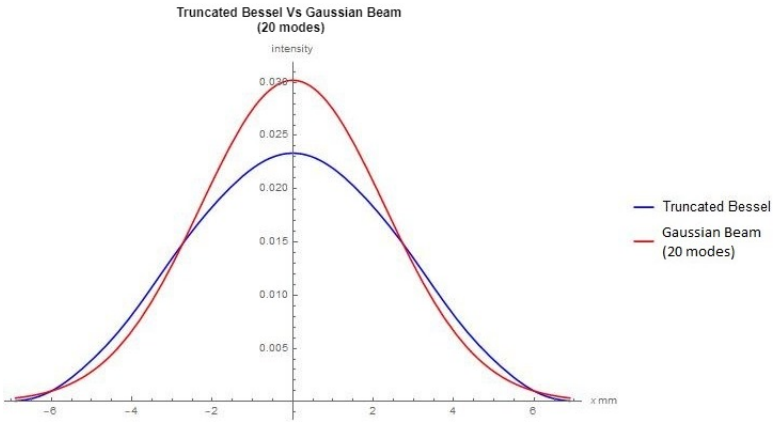

FIGURE 4.33: The power difference between a truncated Bessel beam and a Gaussian beam. The Gaussian beam has been normalised to unity, and the peak intensities of the beams differ by a factor of 1.3.

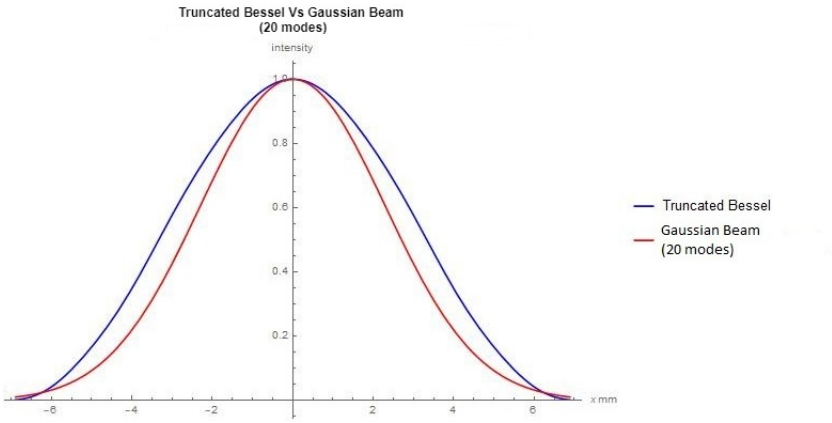

FIGURE 4.34: The truncated Bessel and the Gaussian beam have been normalised to one. This figure shows how the Gaussian beam profile becomes more narrow once its intensity has been normalised.

4.7.2 CST Modeling

CST allows us to enter a beam waist and model a perfect Gaussian source at a user-defined distance. Since the position and beam waists with respect to the GRIN lens were known in the lab, this was realised to be the most efficient way of modelling the lab setup with finite element analysis (i.e. in CST). In Section 2.6, the required parameters to simulate a Gaussian waist are shown. From the Mathematica script written for Section 4.4.12, which was used to describe the laboratory setup, an estimation of the Gaussian beam waist of the Fresnel lens and its focus position can be taken across the band of the horn. The equivalent Gaussian can be entered in CST in front of the GRIN lens that actually represents the beam produced by the horn and is collimated by the Fresnel lens in the lab setup. Table 4.7 below shows the estimated Gaussian waists and their corresponding positions with respect to the GRIN lens.

Frequency (GHz)	w_0**(mm)**	**Distance from lens (mm)**
80	25.5	-2
90	23	-11
95	22	-26
100	21	-44
110	19.5	-69

TABLE 4.7: Beam waists and distances from GRIN lens

Once the Gaussian source was created, the output **E** field was generated in a 100 mm × 100 mm × 300 mm box originating from the GRIN lens. Figure 1.36 shows an image of an x-plane cut taken from the centre of the lens so that the evaluation of the beam can be observed along the z-axis. The beam is collimated from 100 mm → 300 mm centred around 250 mm.

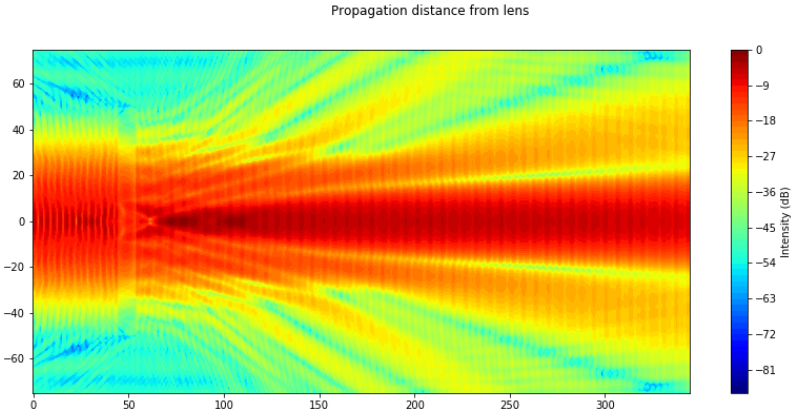

FIGURE 4.35: The GRIN lens is centered at (0,0), so the image shows the propagation of the beam leaving the lens.

As discussed in Section 4.4.12, to represent the E^2 of the horn in the laboratory, 20 mode coefficients were chosen, as they best represented the truncated Bessel profile of the field at the aperture of the horn. However, the CST simulations created a perfect Gaussian source, which would be better represented by the fundamental mode (a perfect Gaussian). Figure 4.36 shows the E^2 field at the aperture of the

horn run for one mode and 20 modes. The 20 - moded beam has a much wider beam profile, which represents the lab horn in Section 4.8. However, to compare the CST results, it is best to use the narrower fundamental mode shown below.

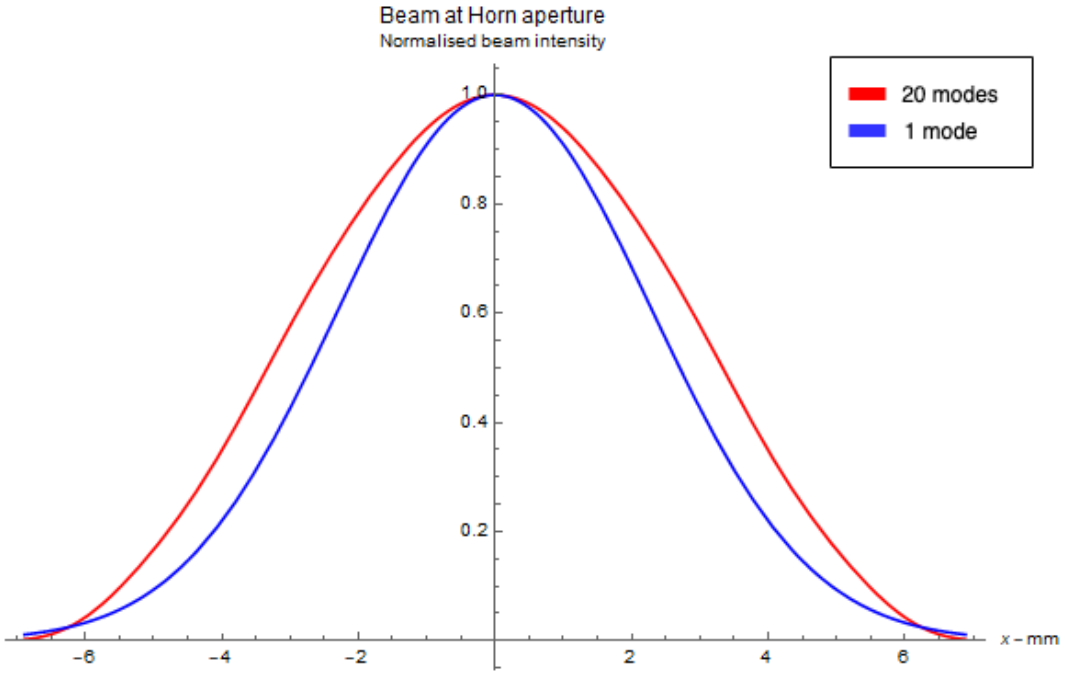

FIGURE 4.36: A comparison between the fundamental mode of a the $\mathbf{E}^2$ field at the aperture of the horn using GBMA. This plot was taken at 100 GHz

Cuts were taken at three different planes along the axis of propagation, to determine the beam profile as it propagates from the lens. The first cut was taken 0 mm from the lens, the second at 200 mm, and the third at the focus (250 mm). Figure 4.37 demonstrates the propagation of the beam as it leaves the lens. For comparison three cuts of the beam were also taken from the CST data: one at the front of the lens, one at 200 mm, and the final cut at the focus, 250 mm from the beam. Then, for comparison, the ABCD matrix plotted above (Figure 4.32) and the Gaussian function were re-normalised and plotted against each other. The plot in the top-left corner shows the CST data matching both the ABCD matrix and Gaussian function very well. The CST data also has higher side lobes at -8 dB, which do not appear in the Gaussian or ABCD data. This could be due to internal reflections within the lens material that are not accounted for in the ABCD

or Gaussian function (fundamental mode) data. The ABCD data only accounts for the refraction of the beam at either boundary of the lens and does not account for any internal reflections within the lens (which is treated as a thin lens). At 200 mm from the lens, the beam becomes collimated.

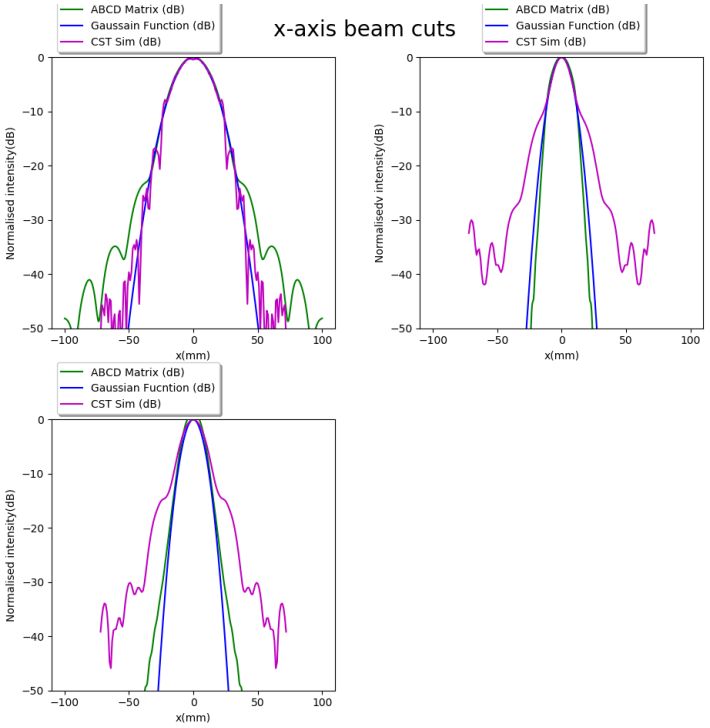

FIGURE 4.37: Top left: CST, ABCD, and Gaussian function cuts taken directly in front of the lens, Top right: CST, ABCD, and Gaussian function cuts taken 200 mm away from the lens. Bottom left: CST, ABCD, and Gaussian function cuts taken 250 mm (at the focus) from the lens.

For a complete comparison of the performance of the lens in CST, several simulations were run across the frequency band of the horn, using the results from Table 4.7. The original permitivities from Table 4.6 were used to the create the lens in CST demonstrated in Figure 4.31. The cuts in Figure 4.38 were taken at the focus of the beam. All the beams in Figure 4.38 have been renormalised to 1 for the purpose of comparison. Here we see a good fit between the CST results and the fundamental Gaussian. However, much like the results in Figure 4.37 we are seeing multiple reflections within the lens and the **E** field generated by the simple

Gaussian having an effect on the beam profile. In Section 4.8, these two effects are explored further.

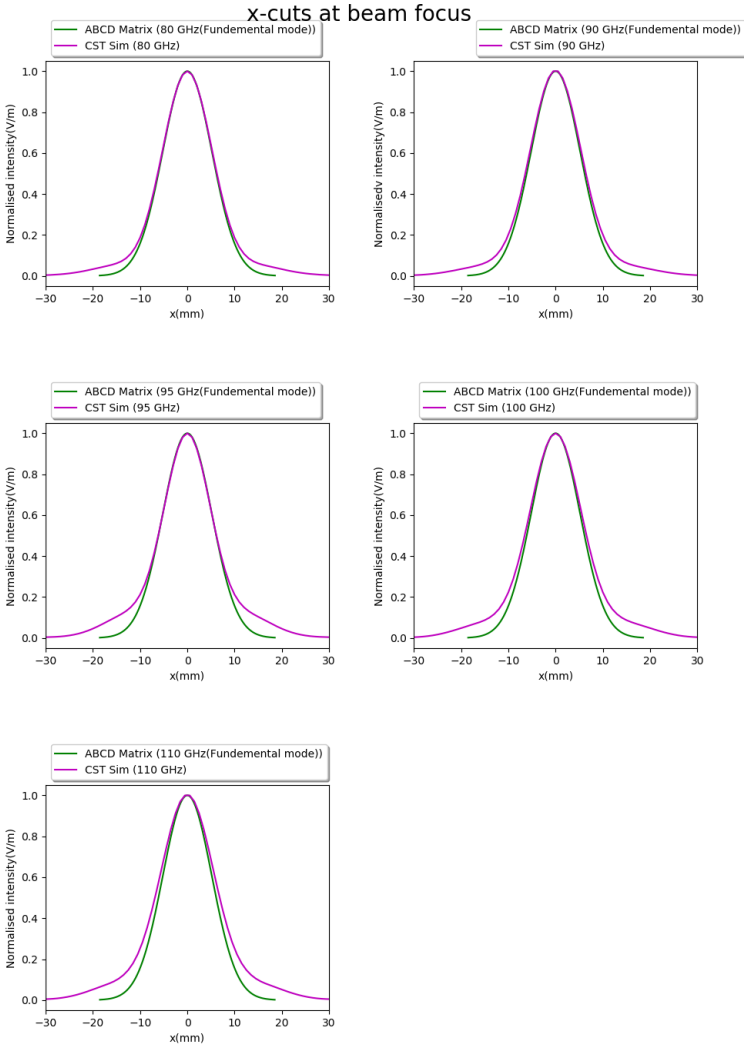

FIGURE 4.38: 80GHz, 90GHz, 95GHz, 100GHz, and 110GHz CST simulation cuts taken at the focus of the beam at 250 mm. Because the CST source has a simple Gaussian profile, the CST data is modelled against the fundamental Gaussian mode.

4.8 Final Lens Lab Results & Measurements

4.8.1 Measurements

In the laboratory, the same optical bench from Figure 4.23 was also used for scans taken of the beam of the final lens. All of the calibrations in 4.4 were preformed on the lens, including the through and reflection standards found for normalisation in post processing. Once the beam was centered, scanning pattern 1 was chosen to find the focus of the beam. The scan started at the nominal position and scanned ± 70 mm in the z-direction in steps of 1 mm and ± 60 in the x-direction in steps of 1 mm.

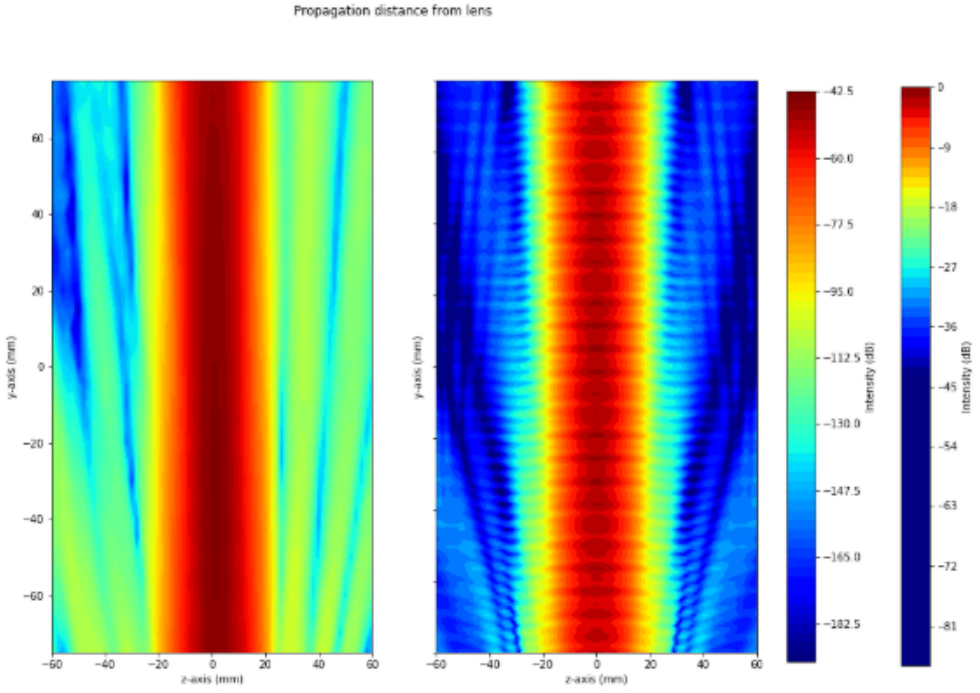

FIGURE 4.39: Left; Propagation of the of lab beam centered around 250 mm from the lens. Right; propagation of the beam in CST centered around 250 mm.

Figure 4.39 shows the collimation of the lab data and the CST beams centered around 250 mm. Both beams are well collimated around the nominal position. Once the beam focus was found for the lab data, cuts of the beam were taken. If

we consider confocal distance of the ABCD results was ± 113 mm, the CST and lab results confirm this. Both plots show the collimation of the beam is centered around (0,0) corresponding to a distance of 250 mm away from the lens. This is the focus of the beam as expected. Scans were taken at 250 mm from the lens where the beam was focused. A scanning pattern of -30 mm → 30 mm with a sample rate of 0.4 mm was used for these cuts. Once these cuts where established, the resultant field intensities across the horn bandwidth were plotted.

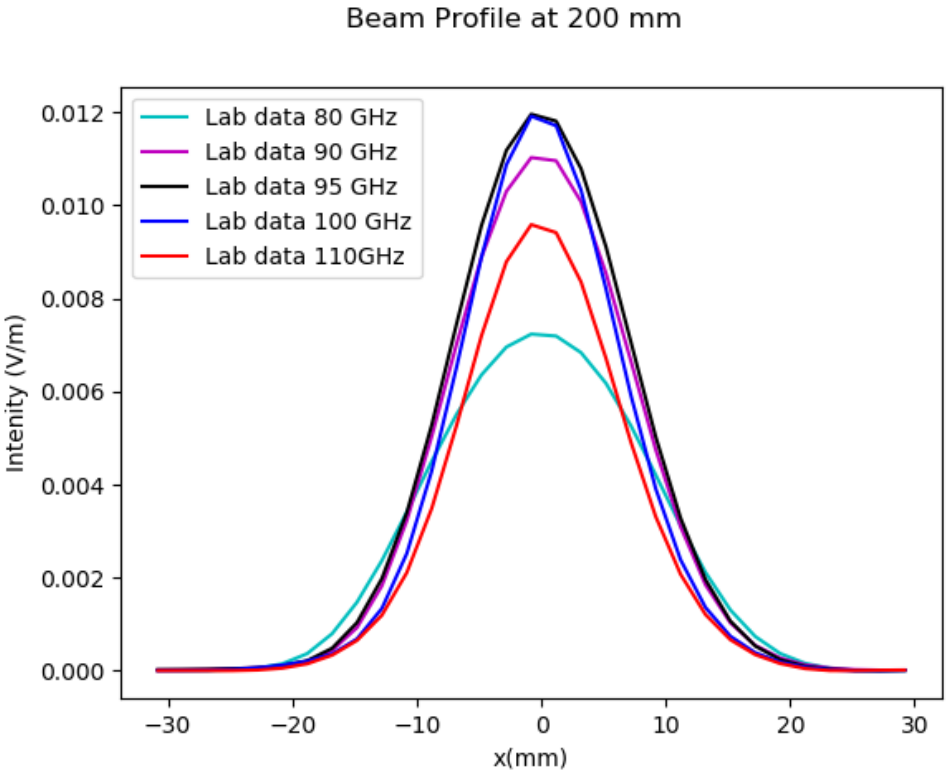

FIGURE 4.40: Comparison of amplitude profiles 80 GHz,90 GHz,95 GHz,100 GHz and 110 GHz

Figure 4.40 shows all 5 measured beams plotted against each other. The central frequencies in Figure 4.40 have the highest intensities and smallest beam radii either side of these central frequencies. This effect is due to the design of the horn, which has been optimised to operate at 94 GHz and performs better at higher frequencies (see Figure 4.12). The loss in intensity can be explained if we consider Figure 4.28. The reflection coefficient S_{22} is much higher either side of the central

frequency. If we refer back to Figure 4.12, we can see that the horn operates best in the centre of the band, its central design frequency being 94 GHz. This is the reason for higher reflections away from 95-100 GHz.

Finally, to understand how well the lab measurements compared to the ABCD and the CST models, they were plotted against each other. The lab data were re-normalised to 1 so as to compare results with the CST data and the ABCD data. Figure 4.41 demonstrates how well the lab data fit both the ABCD and the CST data. It is clear that although there is good agreement between the ABCD data and the lab data, the CST simulation differs because it is a perfect Gaussian and is being compared to a truncated Bessel function. As described in Figure 4.36, the perfect Gaussian has a more narrow profile. On top of this, the air to PLA ratio could not be simulated. In the lab, the 3D-printed lens uses Equations 4.3 and 4.4 to mimic a relative permittivity. However, the CST simulation cannot simulate the air-to-volume ratio of each annular ring; instead, a homogeneous material with a constant permittivity value is defined. To fully understand how the **E** field interacts with the 3D lens, a full simulation with different infill percentages would have to be simulated. This, unfortunately, is outside the scope of the meshing and is too computationally intensive for a finite element package such as CST on a normal PC.

At the higher frequencies (100 - 110 GHz), the CST beam width has become larger than the lab data and ABCD data. Figure 4.42 shows how the lens performed outside the design frequency of the lens. At the lowest frequency tested, the lens lab data has the largest beam radius and there is some reasonable agreement between the CST and ABCD data. At lower frequencies the performance of the horn can account for the large beam radius evident in the lab data. Figure 4.12 shows the horn performs worst from 70-85 GHz, having a much larger reflection (S_{11}) of -20 dB. This would account for the poor fit seen in the data at 80 GHz.

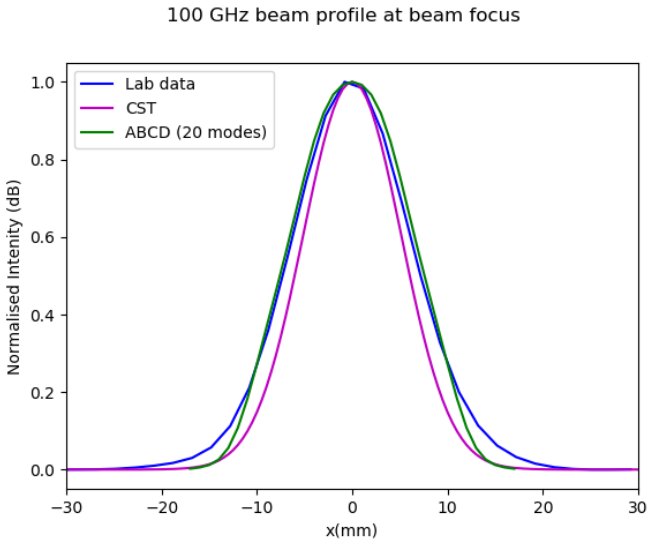

FIGURE 4.41: Lab results, ABCD (20 modes) and the predicted CST intensities using dielectric constants in table 4.6 at 100 GHz

To see a better representation of the horn, a full mode matching analysis of the horn at 75-110GHz would have to be calculated.

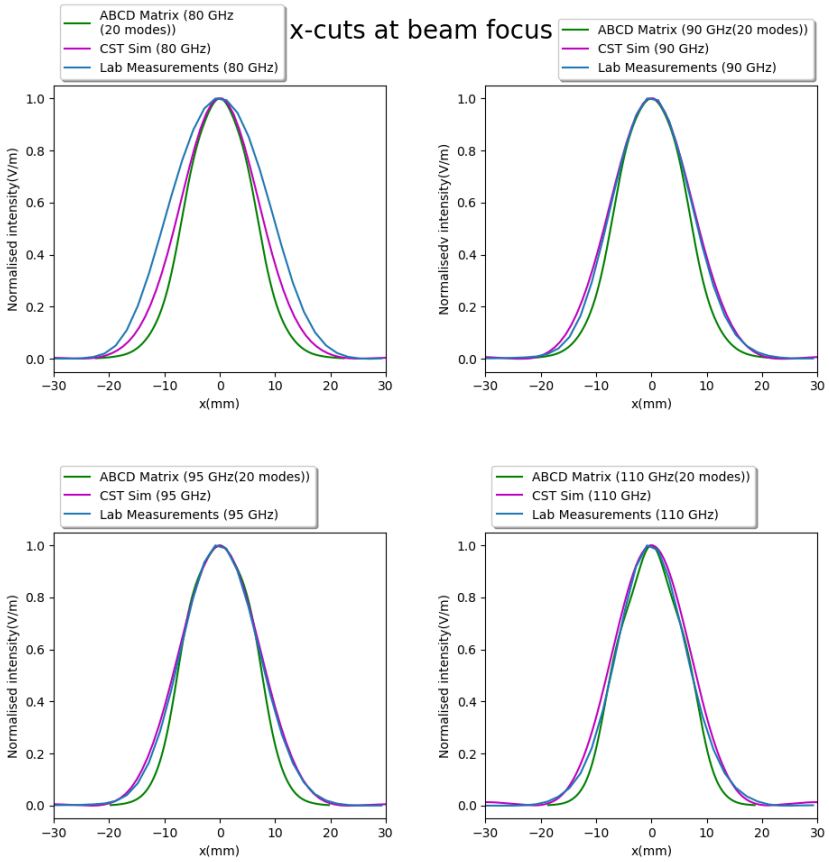

FIGURE 4.42: Comparison between normalised ABCD, Lab and CST data for 80 GHz, 90 GHz, 95 GHz and 110 GHz at 250 mm.

4.9 Conclusion

The goal of this chapter was to design, manufacture and analyse the performance of a 3D printed GRIN lens and to demonstrate its focusing capabilities at a frequency of 100 GHz. Two 3D printed lens where analysed using 3D EM simulation software CST and GBM analyses.

The first lens was designed largely as a proof of concept to test how the PLA infill percentages performed using equation 4.2, 4.4 and 4.3. Using these equations a proto lens was designed with a max permittivity of 2.72 (this was an estimation from [Zhang et al., 2016] at the time). 2D cuts of the beam were taken centred on the predicted focus of the lens and the results are shown in Figure 4.25. The beam was not behaving as predicted, focusing the radiation 40 - 60 mm from its expected position. This promoted some further investigation into PLA permitivity and its corresponding infill percentages.

To find the permivitiy of the PLA used in the laboratory, samples of different infill percentages were printed each with a thickness of 3 mm (see Table 4.4). The S_{11} value for each sample was tested accross the W-band, using the NRW method oulined in Section 4.5.3. Using Equation 4.15 the S_{11} were fitted to this function to determine the permitivity of the bespoke infill percentages. The fits can seen be in Figure 4.28 and their corresponding permitivity in Table 4.5. Figure 4.29 demonstrates the linear relationship between the permitivities and the infill percentages. The relative permitivity of 100% infill PLA was found to be 2.62 and not 2.72 as previously predicted. With this new 100% infill PLA permitivity calculated the second lens was designed.

To enhance focusing performance in the second lens a new lens holder was 3D printed which could accommodate a 100 mm lens. This allowed for 99.997% of the incident radiation be captured. This second lens had a focus of 250 mm. There are

some other key differences between the proto - lens and the final lens design: two extra annular rings were added to the design to optimise performance and a slower extrusion rate was chosen which gave the lens a more homogeneous infill, with less defects than the proto - lens. Most importantly the new lens was designed with improved calculation for 100 % PLA, using Equations 4.2, 4.4 and 4.3. Once the focus of the beam was found at 250 mm, as predicted, linear cuts where taken to determine if the beam was behaving as predicted.

To analyse the behaviour of the lens, simulations were run in CST using a perfect Gaussian as the emitter source, which emulated the performance of corrugated horn used in the lab (**E** field from a corrugated horn is 98% Gaussian). Due to high computational intensity and meshing the exact lab setup could not be simulated in CST. Alongside these simulations an ABCD matrix was written to calculate the beam widths, using GBM analyses. This allowed mathematical modelling of the exact optical setup in the laboratory as seen in Section 4.4.12. This allowed for precise modeling of the truncated Bessel (equation 4.5) profile of the EM field at the mouth of the horn, which is seen in Figure 4.24. Figure 4.37 and 4.38 show how well the ABCD matrix predicts behaviour of the lens in CST, when only the fundamental mode (e.g. a perfect Gaussian) is calculated. This can be used as a confirmation that the predicted ABCD modeling of the laboratory setup and the CST simulation are behaving as predicted. Both data sets have excellent agreement. Finally the lab data could be compared to the two models (the ABCD as a truncated Bessel). All of the data was renormalised to 1 for comparison.

If research was to continue on this project, a more optimised lens could be designed. The weighting of the annular rings could be optimised to better mirror the power percentage of radiation incident on each ring. This would allow for a more refined beam with better focusing abilities. On top of this, more material analysis could be done to test the frequency dependence of infill percentages. Infill permitivities could also be modelled against equation 4.2 to compare their relationship.

Chapter 5

MAGMA-C geomagnetic space mission

5.1 Alpbach Summer School

As part of my Masters degree I participated in the Alpbach Summer School which ran from the $16^{th} - 25^{th}$ of July, 2019. There I worked as a part of an international team of 16 students to design a candidate ESA mission, based on a number of criteria. The theme of the summer school was "*Geophysics from Space using Micro- or Nano-Satellite Constellations*". Daily morning lectures were given on both the theoretical aspects and the engineering features for prospective missions. This year the Earth's magnetic and gravitational field were the subjects in question. The particular engineering constraints for this year were based around micro and nano satellite constellations.

On the evening of the second day groups were asked to have preliminary details for a proposed mission. Team Blue (the author's team), proposed a mission based around the measurement of the mantle's conductivity, which would lead to other exciting predictions about the water content of the Earth's mantle. Each evening

an informal progress report was given on the team's current progression. Each team chose a candidate to give a speech to the professors and coworkers, for Team Blue the author was the chosen candidate. The role of the author was to research as part of the science team, to determine the scientific objectives and requirements for the prescribed mission. There were three separate formal reviews, given by different experts over the course of the 2 weeks ending with a final report and an hour long seminar given by each team.

5.2 Mission Overview

MAGMA-C is a proposed eight satellite constellation in a Low Earth Orbit (LEO) to measure the Earth's magnetic field in order to study the induced magnetic field in the mantle. The primary goal of the MAGMA-C mission is to provide an unprecedented 3-D conductivity profile of the Earth's mantle, derived from its induced field. The mission aims to measure the total magnetic field using scalar and vector magnetometers and separate the different magnetic field contributions in order to isolate the induced mantle field. One of the major advantages of the mission is the use of a microsatellite constellation, improving the measurements spatial and temporal resolution compared to previous missions (Ørsted, CHAMP, SWARM). This directly relates to the quality of the magnetic field sources separation process, and thus to the accuracy of the extracted mantle field. The higher resolution provided by the constellation measurements aims to bring the knowledge of mantle conductivity profile one step further, providing the first 3D conductivity profile derived from these measurements. Combined with ground based seismic tomography and laboratory experimental data, the 3D conductivity profile derived by the mission can better estimate the temperature and water content of the Earth's mantle. This will improve knowledge of Earth's internal dynamic processes as well as terrestrial planetary formation.

5.3 State of the Art

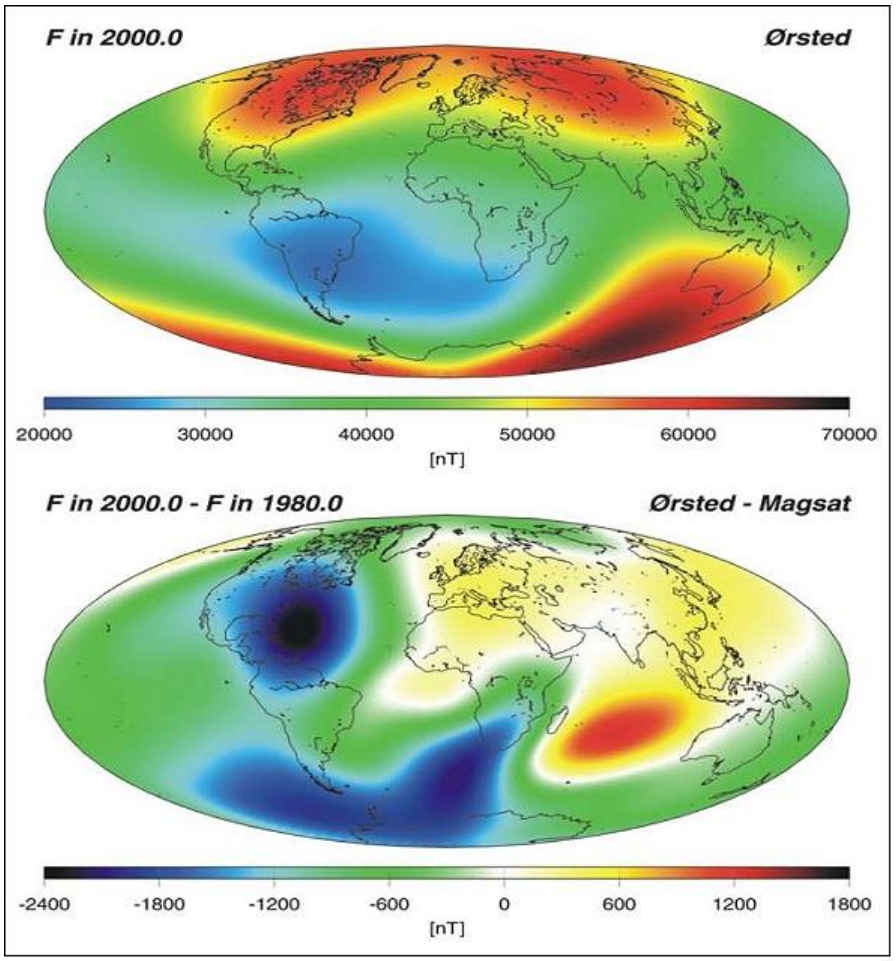

FIGURE 5.1: The top figure displays a color-coded global image (in Mollweide projection) of the Earth's overall magnetic field strength in the year 2000 as modelled from the Oersted data. The scale spans from 20000 - 70000 nT (nanoTesla). The bottom field displays the differences between Oersted results from 2000 and results from the Magsat mission (1979-1980). The scale spans here from -2400 nT to +1800 nT. The changes in field strength over the 20 years span between the two missions are mostly negative and ranges up to almost 10% of the total field [ESA, 2015b].

The Ørsted mission was launched on 23rd February 1999 [Kramer, 2002b] and was tasked with preforming highly accurate measurements of the geomagnetic field and global monitoring of the high energy charged particles. The data were used to improve the current geomagnetic models, to study the auroral phenomena, and to correlate with Earth based measurements [Lundahl Thomsen and Hansen]. The

work done by Ørsted has provided a basis for the International Geomagnetic Reference Field (IGRF) models which are used for scientific tasks such as to develop models for the geo-dynamo and the Earth's secular variations, to provide mapping the Earth's crustal magnetic anomalies. The (then) high resolution measurements enabled detailed mapping of the electric currents in space and the coupling of the solar winds to Earth's magnetosphere.

The next major mission launched due to the success of Ørsted, was CHAMP. CHAMP was a German mini satellite mission, whose overall science mission was to investigate global long-to-medium wavelength recovery of the static and time variablility of Earth's gravity field from orbit perturbation analyses for use in geophysics [ESA, 2015a] and global magnetic field recovery. As the crustal magnetic field is less then 1% of the overall field precise processing across data from three satellites is needed to identify and remove minor fluctuations in the dipole field (core) from CHAMP measurements so that the crustal field component can be imaged (see Figure 5.2). The largest crustal anomaly observed by CHAMP is the Kursk anomaly measuring about 2 nT at 400 km altitude [ESA, 2015a].

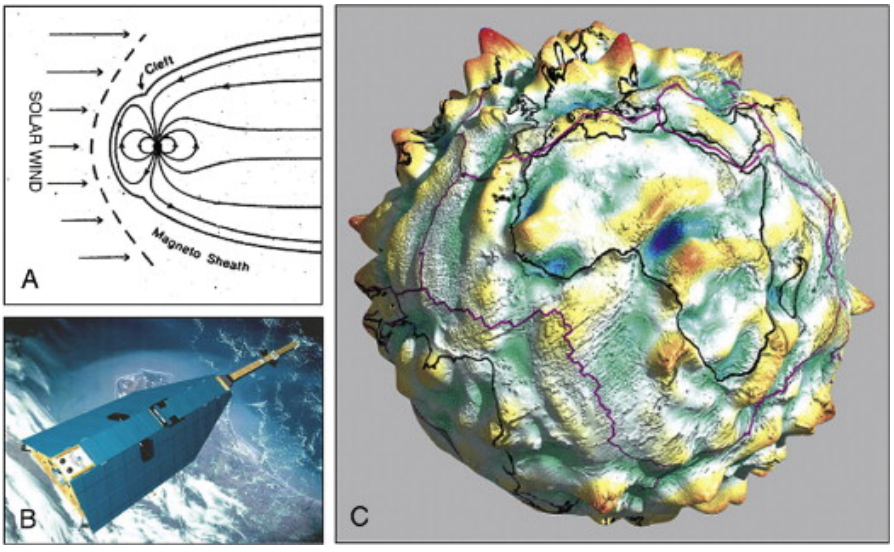

FIGURE 5.2: (A)Earth's dipole field interacting with the Sun's solar wind. (B) CHAMP satellite. (C) The crust's magnetic field as measured 400 km altitude, centred on Africa and Atlantic Ocean. [Fairhead, 2012]

The most recent ESA mission to monitor the Earth's magnetic field is SWARM. The mission itself consists of three satellites (SWARM a, b and c), which were launched on the 22 November 2013. Currently the SWARM mission is still active and relaying data to the Earth. Its main mission is measuring and untangling the different magnetic signals from the Earth's core, mantle, crust, oceans, ionosphere and magnetosphere. Since its launch, there have been a large amount of publications accredited to the mission. From the first observations of super bubbles [Cherniak and Zakharenkova, 2016b] in the ionosphere to modelling of the ocean currents and their effect on the overall magnetic field. The full list of publications can be found on the ESA website [ESA, 2020].

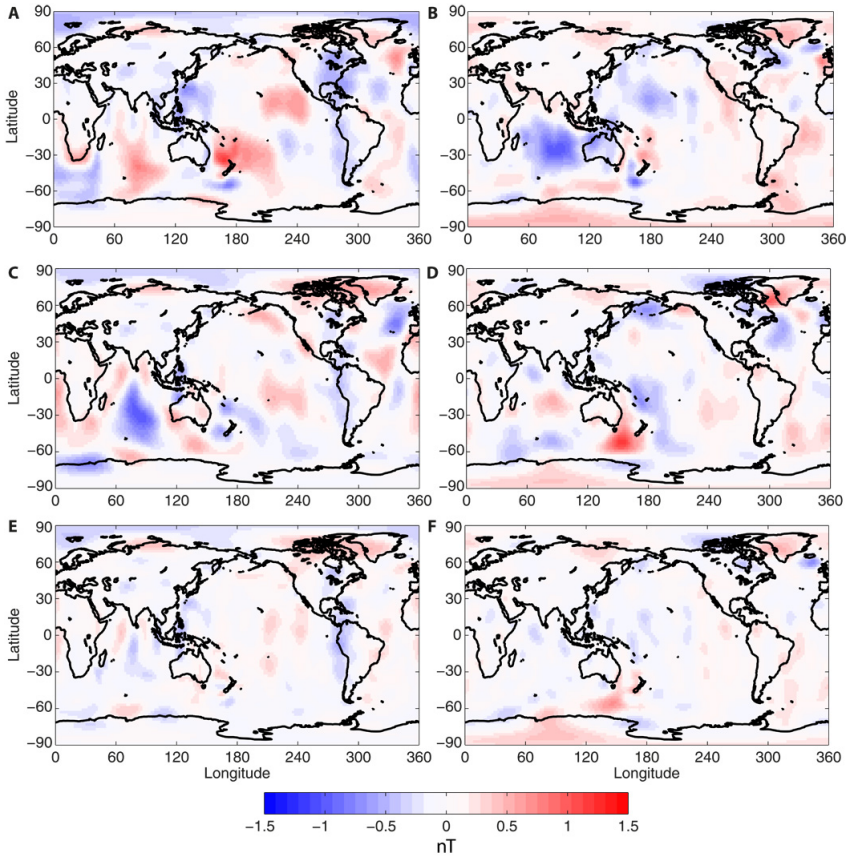

FIGURE 5.3: Difference between observed and predicted in-phase (left) and quadrature (right) radial magnetic field components due to the tidal flow at the satellite altitude (430 km). (A and B) For an insulating mantle. (C and D) For a homogeneous mantle of 0.2 S/m conductivity (used as an initial guess for the inversion) [Sachl and Hanyk, 2015].

5.4 Background and Theory

Earth's magnetic field extends from its interior out into space. The overall field has contributions from the core, crust, ocean tide, magnetosphere and ionospheric fields together with the induced mantle fields. Each zone adds an incremental contribution to the overall field, albeit the predominant component emanates from the core. The core field itself contributes to 98% of the Earth's overall field at the Earth's surface, ranging from 20,000 nT at the equator to 70,000 nT at the poles.[Cherniak and Zakharenkova, 2016a]

Heat in the Earth's core is caused by (1) the energy from the planet's formation, which has not yet been lost; (2) frictional heating, caused by the denser core material sinking to the center of the planet; and (3) from radioactive elements [Williams, 1997]. This heat energy is a driver for the convectional currents in the Earth's core which results in dynamo action. Dynamo action results from rotation of a very conductive material such as iron, which then due to its high conductivity creates a strong magnetic field.

The core field dominates at wavelengths of 3000 km and larger (see Figure 5.7), whereas the crustal field dominates at smaller wavelengths of about 2500 - 56 km. Crustal magnetism originates from ferri- and ferro-magnetic rocks which are below their Curie temperature. The increase of temperature with depth in the Earth means rocks at certain depths become less magnetic or even lose their magnetism altogether.

The next component that must be investigated is the ionosphere. The ionosphere is defined by [Thébault et al., 2010] as the layer of the Earth that is ionised by solar and cosmic radiation and lies 75 -1000 km above the Earth's surface. Due to high energy cosmic rays and solar radiation, the atoms become ionised. This creates a layer of free electrons which are in a plasma state.

The ionosphere is more time dependent than the core field and crust field. It has nightly and daily variations which are dependent on the solar cycle. At night, there is no interference from the Sun, so it is only the cosmic rays that ionise the plasma. During the day, the Sun's X-rays and UV rays increase the ionisation. This variation has a period of 12 hours at the equator [Hsieh et al., 1987].

The outer most region of the Earth's magnetic influence is known as the magnetosphere. Formally defined as the area around the Earth that is controlled by Earth's magnetic field. This field is created by the magnetohydrodynamic (MHD) dynamo in the ionised fluid in Earth's core.

At interplanetary distances gases are usually in their neutral form. Even if ionisation does occur, due to the higher density and pressure, the mean free paths of the particles are much smaller, meaning the ionised particles will recombine quickly. Starting about 80 km above the Earth's surface ionised gas dominates. With increasing height the number of neutral gas particles decreases, while the number of ionised gas particles increases. When the magnetosphere is reached, ionised gas dominates. All of the matter at this altitude is constantly being bombarded with high energy electromagnetic radiation from the sun, which immediately ionises it.

By definition these charges are in a plasma from. This plasma consists of positively and negatively charged particles, and due to these charged particles electromagnetic processes will dominate. One of the main processes in question is the high conductivity of plasma caused by the free charges. The motion of free charges causes a current, which in turn induces a magnetic field. This induced field adds to Earth's overall magnetic field.

The inner boundary of the magnetosphere is determined by the density of charge. At denser regions of lower altitude, Brownian motion [Williams, 1997] is dominant and the magnetic field has less influence. The outer boundary of the magnetosphere is the magnetopause, seen in Figure 5.4 below. In the direction of the Sun

this boundary is detected at 10 Earth radii. In the opposite direction it extends beyond the moon.

The magnetosphere is formed from the iteration between the solar wind and the Earth's magnetic field. The magnetopause is formed at the point were the solar wind equals magnetic field pressure. The bow shock develops when the supersonic wind is slowed to subsonic velocities.

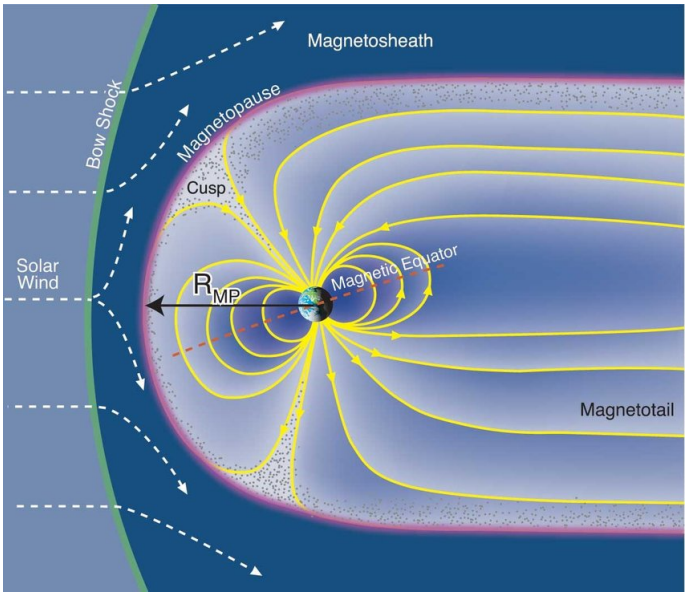

FIGURE 5.4: Layers of Earth's magnetosphere [Akbari, 2015]

The mantle itself doesn't have an intrinsic magnetic field. It instead gains its magnetic profile from all the time varying components of the overall field. The main contributions to the mantles field originate from; the ionosphere, magnetosphere and tides. The core field does vary but on much larger time scales, so for this instance it considered static. The currents in both the ionosphere and magnetosphere create magnetic fields that are highly time-dependent. The movement of sea water through the Earth's magnetic field also creates a current resulting in a magnetic field contribution with a well measured periodicity of 12.42h [Hsieh et al., 1987].

5.4.1 Ionospheric Variations

The Sun constantly bombards the ionosphere with charged particles, the energy of these particles varies on a yearly, seasonal, monthly, daily and hourly basis. [Luxorion, 2000] describes the five main perturbations that occur in the ionosphere:

- **Diurnal variation** are variations that occur due to the apparent movement of the Sun.
- **Seasonal Variation** are the variation of electron densities due to the position of the Sun with respect to the zenith (angle from the zenith is larger in winter than in the summer). If we take winter as an example case, the Sun is always lower to the horizon than in the summer.
- **Latitudinal Variation** As the seasons vary the solar zenith angle also affects the ionosphere with latitude.
- **Variations from day to day** occur due to air temperature variation following the 24 hour cycle.
- **Solar activity** is a day to day variation which is characterised by electromagnetic and particle emission of the Sun, which is the main factor effecting the ionosphere.

5.5 Mission Objectives and Scientific Requirements

Science Objectives To measure the Earth's magnetic field at ionospheric altitudes with a high spatial and temporal resolution to isolate the magnetic field due to induced currents in the mantle. The main five variations of activity in the ionosphere are defined above in Section 5.4.1.

Primary Objectives The primary aim of the mission is to establish a global 3-D conductivity profile of the mantle from the induced magnetic field due to the magnetospheric and ocean currents.

Specific Objectives The 3-D conductivity mapping of the Earth's mantle can be used to infer the presence and quantity of water dissolved in the mantle. Water in the mantle lends extra charge carriers to materials in the mantle, which then increases the conductivity of the mantle by one or two orders of magnitude depending on the water concentrations [Schmandt et al., 2014b]. Compared with temperature or composition in the mantle, this change in conductivity is much larger. Water is therefore relatively easy to detect using conductivity profiles, even when the composition and temperature are not very well characterized.

The presence of water in the Earth's mantle in large quantities is well known [Schmandt et al., 2014a]. In fact this dissolved water accounts for most of the water content on Earth. Water in the mantle causes a weakening effect in several different minerals such as quartz, olivine, pyroxene and feldspar [Fei et al., 2017]. This phenomenon escalates with increasing H^+ densities. This is due to the hydrolysis process, which moves the dislocations in the lattice. For example in wet quartz, lattices dislocated much more readily then in dry quartz. These dislocations are caused primarily by H^+ protons, as the electrons tend to diffuse within the lattice. These structural deformation of the lattice affect the conductivity and thermal properties [Schmandt et al., 2014a]. This in turn will cause a larger induced current in the mantle due to the overall increase in conductivity.

Electrical conductivity, ion-diffusion and attenuation of seismic waves are all influenced by these proton doped lattices. Lab experiments indicate an increasing conductivity with increasing water, with electrons as majority carriers. Ion diffusion rates also increase by a factor of 10-20, sometimes even 1000 for the case of Si, whose diffusion is significantly larger in olivine. Seismic properties are also heavily

dependent on the water concentration. The proton weakening affects interatomic bonds, which changes the elastic properties of the mineral in question. This in turn changes the attenuation of seismic waves due to dissipation effects of kinetic energy [Ohtani, 2020].

According to [Ni et al., 2017] the electrical conductivity in hydrogen bearing olivine are significantly higher than those of hydrogen free olivine. Not only is there a conductivity difference, there is also a difference in the enthalpy. For example the paper quotes an estimate of $3\pm.04$ ASm^{-1} for "wet"olivine and 2.404 ASm^{-1} for "dry" olivine.

The continued research of Earth's interior processes is vital to understand and embellish the heritage of data already available. Having a better understanding of mantle magnetism, conductivity profiles and water content will lead to better modelling of the Earth's interior. Furthermore, with better models more accurate seismic predictions and forecasting can be made. On top of this, the models of Earth's plate tectonics and magnetosphere could also be applied to other known celestial bodies in the solar system and exoplanets outside the solar system.

5.6 How Can We Achieve This?

As mentioned in the Section 5.5, the mantle magnetic field must be induced by activity in the ionosphere and magnetosphere. To achieve this induced magnetic field in the mantle, the Earth's total magnetic field will be measured at altitude. Then using the current data modeling method known as "Comprehensive Inversion (CI)" [Sabaka et al., 2018], the individual field components can be separated (e.g.: core, lithospheric, magnetospheric, and ionospheric spherical harmonic (SH) expansions, time-varying when appropriate, and Euler angles describing the alignment between the vector fluxgate magnetometer frame (VFM) (more on this in

Section 5.9) system and that of the Common Reference Frame (CRF) system of the star imager (more on this in Section 5.9)) [Olsen et al., 2006]. Once CI has been applied, the core, lithospheric, and primary and secondary ionospheric fields can be derived from Magma-C's satellite measurement and observatory hourly-means (OHM) from all available ground observatories. These resulting residuals (observations minus model values) should contain the magnetospheric primary and secondary fields. From these residuals estimations of the (SH) expansion coefficients q_n^m, s_n^m describing the external (magnetospheric) and g_n^m, h_m^n describing the induced field [Sabaka et al., 2013]. The total field can be characterised in 5.1 :

$$\vec{B}_{magsph/mantle} = \vec{B}_{measured} - \big(\vec{B}_{core} + \vec{B}_{tides} + \vec{B}_{ionsp}\big). \tag{5.1}$$

Equation 5.1 can be split into two main contributions; internal and external. The internal field includes the core field and crustal field. The external field caused by the electrical currents from the ionosphere and the magnetosphere.

5.6.1 The Geomagnetic Field Model

Earth's magnetic field can be described using surface harmonics These harmonics are orthogonal functions whose variables are co-latitiude (θ) or longitudinal (ϕ). Using Maxwell's equations, we know that:

$$\bigtriangledown \cdot B = 0,$$

$$\bigtriangledown \times B = \mu(J + \frac{\partial B}{\partial t}). \tag{5.2}$$

At the Earth's surface to 50-60 km there are no electrical currents and this region is also a continuous surface, we get :

$$J = \frac{\partial D}{\partial t} = 0,$$
$$\therefore \bigtriangledown \times B = 0. \tag{5.3}$$

Knowing this allows the magnetic induction to be written as a scalar potential.

$$B = - \bigtriangledown V. \tag{5.4}$$

Equation 5.4, along with zero divergence implies the geomagnetic potential must satisfy the Laplace equation.

$$\bigtriangledown^2 V(r\theta\phi) = \delta V = 0. \tag{5.5}$$

Finally, solutions to the Laplace equation can be written as spherical harmonics [Glassmeier and Tsurutani, 2014]

$$\bigtriangledown^2 V(r\theta\phi) = R(r)P(\theta)F(\phi)$$
$$R(r) = \begin{cases} (r/a)^2 \\ (a/r)^{n+1} \end{cases} \qquad P(\theta) = P_n^m(\cos(\theta)); \qquad F(\phi) = \begin{cases} \cos(m\phi) \\ \sin(m\phi) \end{cases}$$

$$P_n^m(\cos(\theta)) = \frac{1}{2^n}\frac{d^n}{d\cos(theta)^n} \times \cos^2(\theta) - 1)^n \; for \; m = 0,$$
$$P_n^m(\cos(\theta)) = \left[2\frac{n-m}{n+m}\right]^{1/2} \times sin^m(theta)\frac{d^m}{d(\cos(\theta)^m)} \times P_n^0(Cos(\theta)) for 0 < m < n.$$

The expansion of the scalar magnetic potential from [ESA Alpbach Summer Scool] gives us V, as a series of spherical harmonics is :

$$V(r\theta\phi) = a\sum_{n=1}^{\infty}\sum_{n}^{m=0}(g_n^m\cos(m\phi) + h_n^m\sin(m\phi))(\frac{a}{r})^{n+1} + q_n^m\cos(m\phi) + s_n^m\sin(m\phi)(\frac{r}{a})^n P_n^m(\cos(\theta)), \quad (5.6)$$

(g_n^m, h_n^m) are the time varying Gauss coefficients of the internal origin.

(q_n^m, s_n^m) are the Gauss coefficients of the external origin.

a is the radius of the Earth (= 6371.2km).

n and m are the degrees and order of the harmonics.

Data sets from observations and satellites contain values of the different geomagnetic field elements (e.g, X, Y and Z). These components are related to the geomagnetic potential [Olsen, 1999] through the spatial derivative in spherical coordinates seen below in Equation 5.7.

$$
\begin{aligned}
Z &= -B_r = +\frac{\partial V}{\partial r}, \\
&= \sum_{n,m} \Big\{ -(n+1)\left(g_n^m \cos m\phi + h_n^m \sin m\phi\right)\left(\frac{a}{r}\right)^{n+2} + n\left(q_n^m \cos m\phi \right. \\
&\left. + s_n^m \sin m\phi \left(\frac{r}{a}\right)^{n-1}\right\} P_n^m, \\
X &= -B_\vartheta = +\frac{\partial V}{r\partial \vartheta}, \\
&= \sum_{n,m} \Big\{ \left(g_n^m \cos m\phi + h_n^m \sin m\phi\right)\left(\frac{a}{r}\right)^{n+2} + \left(q_n^m \cos m\phi \right. \\
&\left. + s_n^m \sin m\cdot\phi \left(\frac{r}{a}\right)^{n-1}\right\} \frac{dP_n^m}{d\vartheta}, \\
Y &= +B\phi = -\frac{1}{r\sin\vartheta}\frac{\partial V}{\partial \phi}, \\
&= -\sum_{n,m} \Big\{ \left(h_n^m \cos m\phi - g_n^m \sin m\cdot\phi\right)\left(\frac{a}{r}\right)^{n+2} + \left(s_n^m \cos m\phi \right. \\
&\left. - q_n^m \sin m\phi \left(\frac{r}{a}\right)^{n-1}\right\} \frac{mP_n^m}{\sin\vartheta}.
\end{aligned}
\tag{5.7}
$$

at Earth's surface $r = a = 6371.2$ km:

$$
\begin{aligned}
X &= \sum_{n,m} \left\{a_n^m \cos m\phi + b_n^m \sin m\phi\right\} \frac{dP_n^m}{d\vartheta}, \\
Y &= -\sum_{n,m} \left\{b_n^m \cos m\phi - a_n^m \sin m\phi\right\} \frac{nP_n^m}{\sin\vartheta}, \\
Z &= \sum_{n,m} \left\{(nq_n^m - (n+1)g_n^m)\cos m\phi + (ns_n^m - (n+1)h_n^m)\sin m\phi\right\} P_n^m, \\
&= \sum_{n,m} \left\{\alpha_n^m \cos m\phi + \beta_n^m \sin m\phi\right\} P_n^m.
\end{aligned}
\tag{5.8}
$$

$$
\begin{aligned}
a_n^m &= g_n^m + q_n^m & g_n^m &= \frac{na_n^m - \alpha_n^m}{2n+1}, \\
b_n^m &= h_n^m + s_n^m & h_n^m &= \frac{nb_n^m - \beta_n^m}{2n+1},
\end{aligned}
$$

$$\alpha_n^m = nq_n^m - (n+1)g_n^m \qquad q_n^m = \frac{(n+1)a_n^m + \alpha_n^m}{2n+1},$$
$$\beta_n^m = ns_n^m - (n+1)h_n^m \qquad s_n^m = \frac{(n+1)b_n^m + \beta_n^m}{2n+1}.$$

The different components in X and Y allows us to determine the a_n^m and b_n^m coefficients, while the radial component Z allows us to solve for the α_n^m and β_n^m. Analysing all three components allows us to separate sources of internal (g and h) and external origins (q and s).

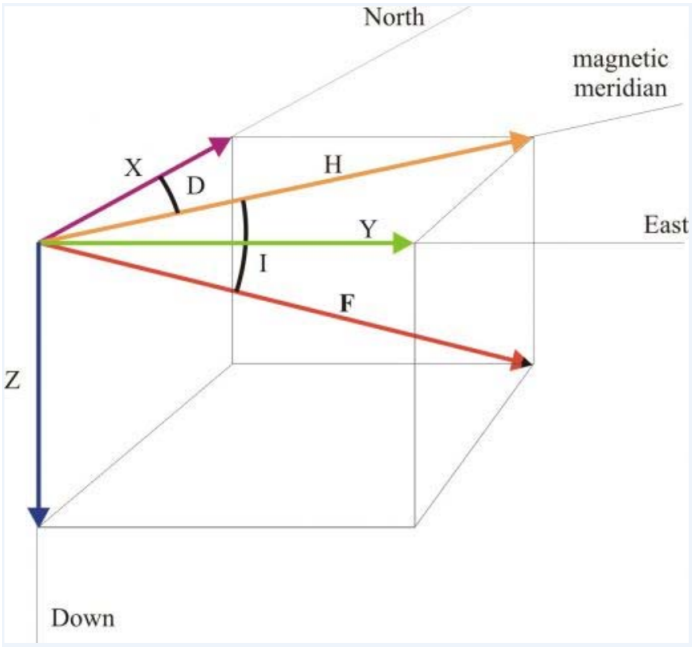

FIGURE 5.5: Diagram of the X, Y, Z, H, I, D and F components of the measured field These components are outlined in the table below [Allen, 2006]

Once internal and external coefficients are known, the spatial power spectrum of the magnetic field at a given height can be defined. [Cherniak and Zakharenkova, 2016a]

$$R_n = (n+1)\sum_{m=0}^{n}\left[(g_n^m)^2 + (h_n^m)^2\,,\right] \tag{5.9}$$

Comp	Definition
X	*northerly intensity*
Y	*easterly intensity*
Z	*vertical intensity, positive downwards*
F	*total intensity*
H	*horizontal intensity*
I	*inclination: the angle between the horizontal plane and the field vector, measured positive downwards*
D	*declination: the horizontal angle between true north and the field vector, measured positive eastwards*

FIGURE 5.6: Field-components [Allen, 2006]

R_n is in nT^2 where n is the SH degree to the squared amplitude of the observed magnetic field. Another definition which will be useful is the spatial wavelength defined by [Kramer, 2002c] as

$$\lambda = \frac{2\pi r}{\sqrt{n(n+1)}} \approx \frac{2\pi r}{n}. \tag{5.10}$$

These two equations combined show the dependency of the horizontal spatial resolution with altitude of the observation.

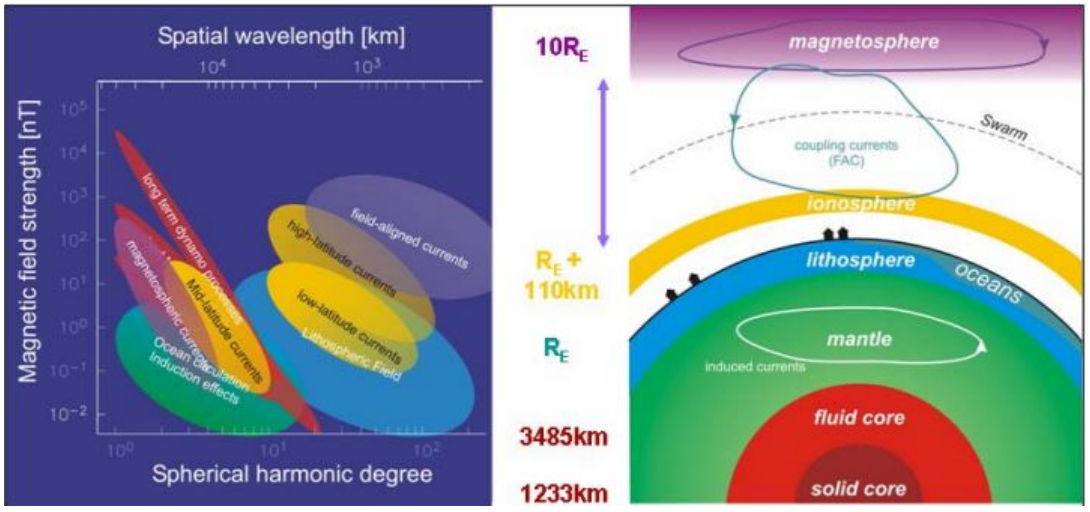

FIGURE 5.7: Layers of Earth's magnetosphere [Kramer, 2002c].

5.6.2 Measurement of Magnetic Field Components to Conductivity Profile

Section 5.6.1 shows how the magnetic field components will be interpreted. From this the conductivity profile of the Earth can be derived. To determine the conductivity profile, the electromagnetic response function of the Earth must be defined in terms of frequency [Olsen, 1998] :

$$Q_n(f) = \frac{i_n(f)}{e_n(f)}, \tag{5.11}$$

where $i_n(f)$ and $e_n(f)$ are the internal and external Gauss coefficients as a function of frequency. This Q-response function is then compared with the theoretical response of an Earth of homogeneous conductivity composed of a few layers.

The C-response was introduced by [Schmucker, 1987] to define a geomagnetic-variation field for a single spherical harmonic. In a 1-d spherically symmetrical source (conductivity depends on radius only) the conductivity distribution is connected to the Q-response by means of

$$C_n(v) = \frac{a}{n+1}\frac{1-\frac{n+1}{n}Q_n(w)}{1+Q_n(\omega)} = \frac{a}{n(n+1)}\frac{z_n^m(w)}{v_n^m(\omega)}, \tag{5.12}$$

where a is the mean Earth radius, n is the spherical harmonic order, Q_n is Q response function, $v_n^m = \epsilon_n^m + i_n^m$ ϵ are external sources and i are internal sources. $z_n^m = n\epsilon_n^m - (n+1)i_n^m$. Subbing Equation 5.11 into 5.12 will yield each component of the magnetic field (see [Olsen, 1998] for full derivation). Using the ratio of $C_0(w)$ to $C_n(w)$ (C_0 is the zero wave and 1-D conductivity models that are consistent with the mean number flat-Earth response see [Olsen, 1998]) the conductivity at specific frequencies can be found:

$$\tau = \frac{C_n(w)}{C_0(w)}. \tag{5.13}$$

5.7 Selected Inducing Sources to Map Induced Responses in the Mantle

The magnetospheric currents can be used as the sources to measure the inducing response in the mantle. Supplementary to this, the tidal fields can also be used, due to its very well defined period of 12.42 hours. This makes it possible to separate it from the other internal induced and inducing fields.

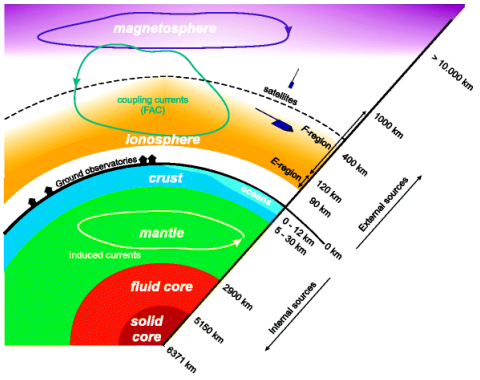

FIGURE 5.8: Earth's Magnetic field [Olsen et al., 2010a]

The main mission objectives are to measure the tidal and magnetosphere fields, so as to capture the induced response of the mantle. The tidal currents are very precisely defined. However, the frequencies of the inducing signals that can be used to extract the induced data field signals in the mantle are driven by the following constraints :

- Signals with T $<$ 1 year, to avoid overlapping with core secular variations.
- Signals with T $>$ 1 days as daily ionospheric variations cannot be separated from the field they induce in the mantle

This constrains the period range of inducing signals that are available for use to 2 days - 6 months.

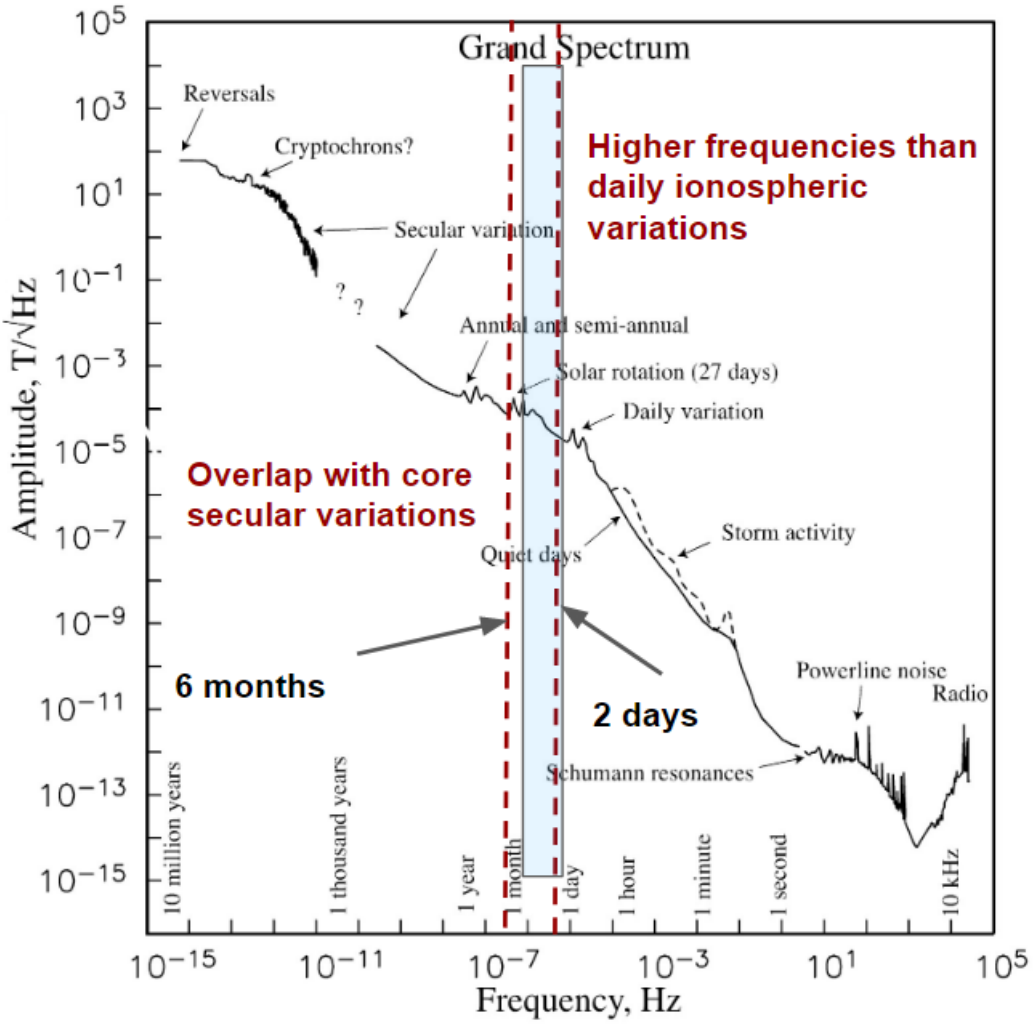

FIGURE 5.9: Full range amplitude spectrum of the Earth's magnetic field showing phenomena with cycle periods from 10 million years to 10^5 s. The dashed red lines represent inducing sources that will be measured by Magma-C [Olsen et al., 2010b].

These inducing currents will be found at different depths within the mantle determined by the frequency using the skin depth equation. From this equation the conductivity can also be found.

$$\delta = \sqrt{\frac{\rho}{\pi f \mu}}, \tag{5.14}$$

ρ is the resistivity, f is the frequency, μ is the permeability if free space.

From Equation 5.14 it follows that lower frequency waves can penetrate deeper into the mantle under the assumption the other variables are kept constant. From the selected inducing sources, the depths down to which the mantle-induced response can be mapped are derived from Equation 5.14 seen below in the table. Since the Earth's mantle has an approximate depth of 2900 km, [Society, 2012] the depths below are taken as a percentage of the total depth.

Source	Period	Penetration Depth (% of the mantle)
Magnetosphere (ring current)	2 days-6 months	13.8 %-55.2 %
Ocean tides	12.42hr	3 %-10.3 %

TABLE 5.1: Required periods and corresponding penetration depth

Currently the most up to date models of ground based conductivity measurements disagree even at the smallest depths into the mantle. As of yet, no satellite has attempted to provide a full 3D survey of Earth's mantle conductivity. Figure 5.10 demonstrates the differences in the current ground models.

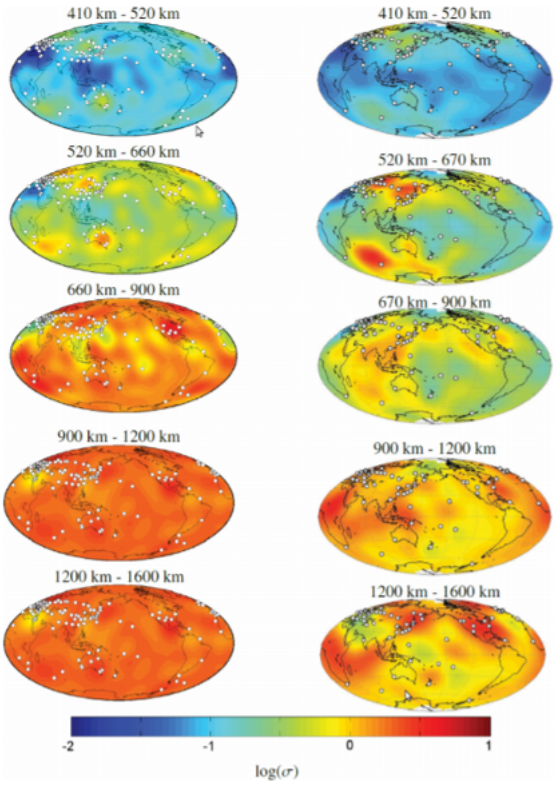

FIGURE 5.10: Comparison of 3D-conductivity profiles derived from ground-based measurements for different depths, from Semenov and Kuvshinov, 2013 (left-hand plots) with results from Kelbert et al. (2009) (right-hand plots) [Semenov and Kuvshinov, 2012]

5.7.1 Separation of Magnetic Field Contributions

From Equation 5.1 all of the individual contributions to the magnetic field can be seen. These different field contributions still need to be separated, so that the induced mantle field can be separated out. There are certain key requirements needed to perform the separation between the different contributions:

- Removing the strong daily ionospheric variations (periods of 24, 12, 8, 6 hours...) by achieving 8 local times (evenly distributed) so that the local time separation is about 3 hours.

- High temporal resolution to capture the extremely short-varying signals in the magnetosphere. (This is required as the magnetosphere is a major inducing

source to map the mantle field). This will be achieved by having full coverage of the Earth in one hour with a lower spatial (1000s of km) and a higher spatial resolution after one day (100s of km).

- The remaining contributions are more straight forward to remove as they are static or have very slow variations (crust and core fields) or because they have very well-defined spatial resolution (tidal field).

To achieve the high temporal resolution required to capture the short, varying signals in the magnetosphere a total 8 micro-satellites covering 8 local times is needed. These satellites will orbit at 4 separate orbital planes, thereby achieving 8 local times.

Additionally, the ionospheric currents are highly time dependent and have very localised variations too. In order to flag these data for removal a specialised instrument such as a Langmuir (measuring electron density and temperature) probe is needed.

Combining the measurements of the total magnetic field with the current position of the satellites, the calibrated magnetic field vector data with respect to the geophysical frame can be achieved. Using auxiliary data from ground-based measurements by magnetometers and ionosondes a model of the ionospheric contributions will be created. As described in Section 5.6 (CI) will be used to separate the field sources with the help of models describing each source [Sabaka et al., 2018]. Well known sources, such as the static crustal field as measured by SWARM, will be included in the model to aid the separation. The results of CI will be the spherical harmonic coefficients describing the internal field from the mantle and the external source field. These will used to obtain the C-responses [Olsen, 1998] describing the response of the mantle to the external fields as a function of frequency. Finally, to obtain the 3D mantle conductivity a Bayesian inversion process needs to be applied.

5.7.2 Summary of the Scientific Requirements

Scientific Requirements	**Mission Requirements**
Measure day-nightside ionosphere variations	Minimum different local times evenly distributed
Map irregular, quick varying magnetosphere currents	Coarse (∼1000km) coverage of Earth in 1h
Mapping of the mantle response to magnetosphere currents	Finer (∼300km) coverage of Earth in 1day
Measure ionospheric local phenomena	Altitude between 350-550km

TABLE 5.2: Summary of Science Requirements

5.8 Data Products

MAGMA-C shall aim to produce a 3-D conductivity map of the mantle, with high spatial resolution of 1° at the equator and temporal resolution of 8 hours. Complete Earth coverage will be achieved, with 3 hours separation in local time, down to the spatial resolution of a few 100s of km after 1 day. Once combined with laboratory experiments and seismic data, both the water content and a temperature profile can be characterised. Improvements can also be made to the current ionospheric models, by making use of the 3 hours local time separation to capture the daily variations.

Instrument	Scientific requirements	Instrumental requirements
Vector Field Magnetometer (VFM)	Range of strength of the magnetic field: ± 25000 nT to ± 60000 nT Noise density in the range of pT/√Hz	Range of the instrument: ± 65000 nT Noise density: 25 pT/√Hz
Absolute Scalar Magnetometer (ASM)		Range of the instrument: ± 71428 nT Noise density: 15 pT/√Hz
Star trackers (to have VFM precision measurements)	Accuracy: 1 nT → 0.001 deg	Accuracy: 2 arc seconds → 0.0005 deg
Electron density sensors (Langmuir probe)	Range of the ionosphere storms: 100 Hz - 3 kHz	Range of the instrument: 10 Hz to 4 kHz

30

FIGURE 5.11: Summary of Instrument Requirements

5.9 Payload

Below Table 5.11 shows the instruments needed to achieve the scientific objects of MAGMA-C. The science team used the scientific requirements to decide the individual instruments required in the payload. Table 5.11 gives a clear description of each component and why it is necessary on the spacecraft.

Each spacecraft is equipped with vector field magnetometer (VFM) and absolute scalar magnetometer (ASM). The VFM selected is a miniaturised fluxgate sensor LEMI-020, which will measure the magnetic field vectors within the range and noise density in Table 5.11. This instrument was developed by Lviv Centre of the Institute for Space Research [LEMI]. With such small dimensions of $20 \times 20 \times 21$ mm^3 the device is ideal for a microsatellite design.

Simultaneously, the ASM will be measuring the absolute magnetic field strength, independently from the magnetic field direction. This is very important for in-flight calibration of the VFM in order to reduce the offset drift issue of the space crafts.

FIGURE 5.12: Vector Field Magnetometer [LEMI]

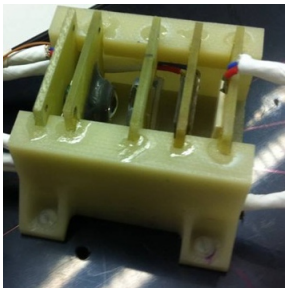

FIGURE 5.13: Scalar Magnetic field [Korth et al., 2016]

To ensure that the orientation of the magnetic field vectors are correct, three star trackers are needed. The particular trackers chosen for the mission are the KU Leuven Star Tracker sold by the CubeSatShop and developed by KU Leuven [KU Leuven, n.d]. This tracker boasts an accuracy of 2 arc seconds. With its compact electronics and size ($45 \times 50 \times 95$ mm^3), it was designed specifically for cube sat missions. Three star trackers are necessary to continue interpreting magnetic field measurements in the eventuality that one of the star trackers are Sun blinded.

FIGURE 5.14: Star Tracker [KU Leuven, n.d].

Finally a Langmuir probe can provide electron densities and temperature, as well as electrical potential. The frequencies that need to be measured in the ionosphere are between 100 Hz to 3000 Hz, which are required to characterise storms and high density bubbles in the ionosphere. The monitoring of the high frequency variations and high density bubbles is necessary for magnetic field measurement correction. The selected Langmuir probe is characterized by a relative electron density error of 10%, as well as a 4000 Hz low pass filter and 10 Hz high pass filter. [Holback et al., 2001]

5.10 Mission Profile

The work in this section was undertaken by the Engineering team who worked closely with the Science team and required their inputs to build a working model of the spacecraft and orbital profiles. The author had no direct contribution but the information is described to give an overview of the mission.

To meet the local times required for the mission (8 local times), a constellation of 8 microsatellites would be required. These satellites will orbit in 4 separate orbital planes, thereby achieving 8 local times. This will increase the temporal resolution to 300 km (1°) at the equator. Table 5.3 below shows a summary of the parameters. Delta RAAN refers to the angle between each longitudinal orbital line of each spacecraft.

Constellation	87°
Altitude	550 km
Eccentricity	Circular
Coverage	8 evenly spaced local times & 300 km spatial resolution at the equator
Delta RAAN	45°

TABLE 5.3: Constellation orbital parameters

Figure 5.15 shows the orbital paths and planes for each individual craft in the constellation, along with the preferred launch site in Anboya Norway

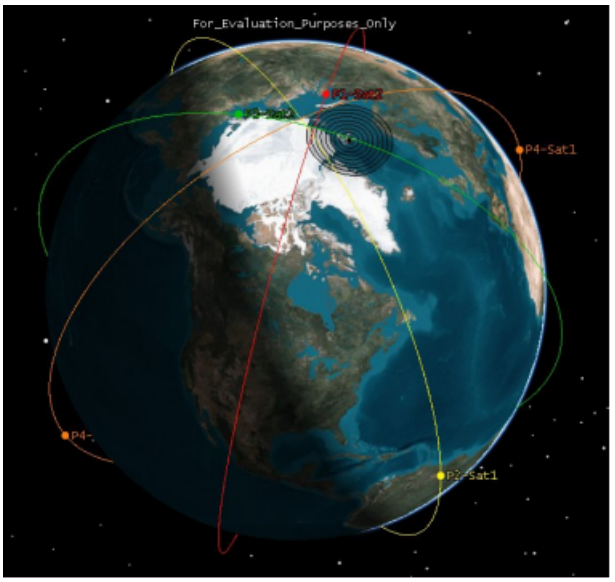

FIGURE 5.15: Orbital planes

5.10.1 Launch and Operations

The launcher chosen was an *Electron* launcher, provided by *Rocket Lab* [Kramer, 2002a]. Considering the uncommon orbit, not many rockets would be available to launch the mission in collaboration with other missions. For this reason a small rocket with a capability of carrying a load of 150 kg into a 550km SSO (Sun Synchronous Orbit) was ideal, and the cheapest option. The selected back up launcher would be the *Pegasus* rocket [Northrop, Grumman].

The launch site (Anboya Norway) was selected due its very northern latitude. If the micro-sat is not ready by 2024 an alternate location in Rocket Lab's launch complex in Mahia, New Zealand, could be used. Two launches will be needed to get all eight satellites into a quasi-polar orbits (87°), separated by 90° in Right Ascension of Ascending Node (RAAN). Then after first contact and deployment of the booms, the satellites will placed into a transfer orbit to achieve the final configuration.

During the operation lifetime of the crafts, it will perform its mission with minor ground operations. The design allows for stabilisation by gravity gradient, and body mounted solar panels will provide enough power, removing the need for solar pointing strategies.

5.11 Spacecraft Design

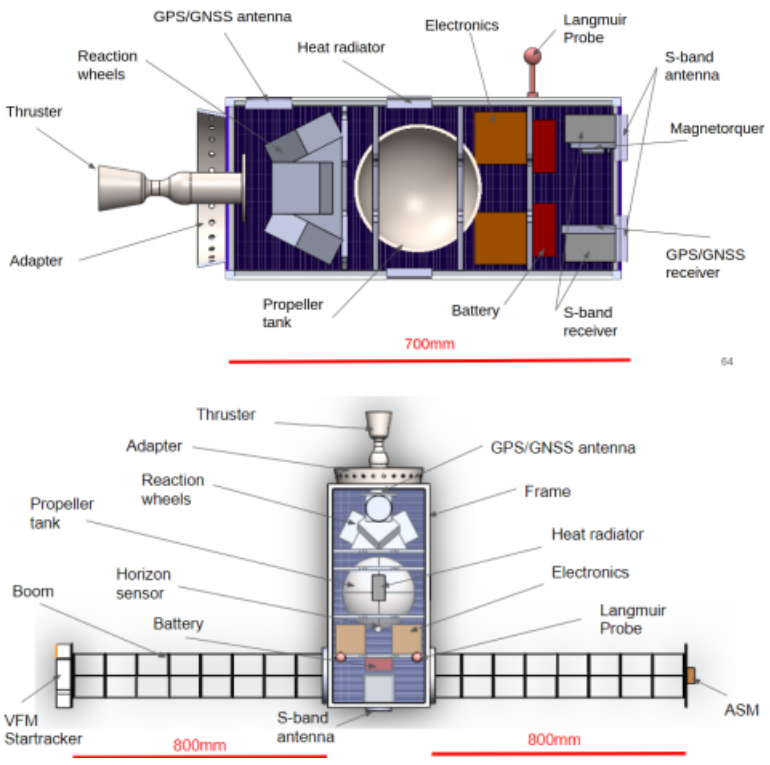

FIGURE 5.16: Diagram of the arrangements of the spacecraft's subsystems and its deployment configuration (ESA Summer School working group, 2019)

5.11.1 Structure and Mechanisms

The primary structure of MAGMA-C consists of a lightweight AI-6061 symmetrical frame reinforced by a honeycomb core sandwich panel. The reason for this design is to counter-act the magnetic field created by the electronics within the structure of the craft [Jiang et al., 2018]. The dimensions of the craft not including the

deployments of the booms are $340 \times 360 \times 935$ mm^3 and $340 \times 935 \times 2066$ mm^3 (including booms). The booms on the spacecraft are used for both stabilisation of the craft and also provide the VFM and ASM with an area on the craft that is not prohibited by EM waves originating from the main operation systems and other components in the centre of the craft.

The only deployment mechanism for the MAGMA-C satellite are the two booms. The *Coilable Boom System* (CBS) developed by the *Northrop Grumman* will be used for its well trusted, long and successful flight heritage [OrbitalATK, 2015]. The advantages of this particular CBS are its well recorded magnetic "cleanliness", excellent thermal stability, allow mass and a compact mast stowage perfect for microsatellites.

5.11.2 Summary of Propulsion, Altitude Orbit Control and Thermal Systems

The propulsion of choice for a mono propellant thruster will be the 22 N High Performance Green Propulsion (HPGP) developed by Bradford ECAPs [Performance and Propulsion].

System	Model	Developer	Features
Propulsion	22N High Performance Green Propulsion (HPGP) Thruster	Bradford ECAPs	This 25W thruster can provide 22 N of thrust, 243 s of specific impulse and weighs 1.1 kg
Attitude Orbit & Control System	NanoTorque GSW-600	GOMspace	N/A
Thermal Control	N/A	N/A	The battery packs and the propulsion system will be equipped with heaters. The radiators with an 8 approximate area of 0.02 square meters will emit about 4.8W. The propellant tank is coated with multilayer insulation. The minimum equilibrium temperature is at -53.4∘C and maximal at 55.5∘ C.

TABLE 5.4: Summary of Propulsion, Altitude Orbit Control and Thermal systems

5.11.3 Power & Power Budget

Two batteries with a capacity of 77 Wh and 8 cells each for energy storage will be used. The surface of a spacecraft will be covered by solar panels with a total area of 0.7 m^2. A summary of the power budget is shown below in Table 5.5.

Power Budget for each operating mode					
Sub System	**Safe Mode**	**Orbital Control Mode**	**Normal/Busrt Mode**	**Commissioning Mode**	**Downlink Mode**
Science Instruments	-	-	4.5 W	-	-
Telecommunications	2 W	2 W	-	-	-
Propulsion	-	8 W	-	-	-
C&DH	5 W	5 W	5 W	5 W	5 W
ADCS	-	30.5 W	30.5 W	30.5 W	30.5 W
Structure	-	-	-	10 W	-
Battery	-	-	25 W	-	-
Subtotal	7 W	45.5 W	67 W	47.5 W	43.5 W
Margin	20%	20%	20%	20%	20%
Total	**8.4 W**	**54.6 W**	**80.4 W**	**57 W**	**52.2 W**

TABLE 5.5: Summary of the power budget for each operating system

5.12 Descoping Options and Risk Analysis

5.12.1 *In case of boom deployment malfunction*

If the boom fails to deploy, the spacecraft operations will be interrupted. This will hinder the ability of the magnetometer to take accurate readings due to its proximity to the electronics. Measurements can still be taken, but with degraded quality.

5.12.2 *In case of launch failure*

If one of the launches fails and the constellation is only left with 4 satellites, the science capabilities may be diminished. It is important to have an evenly spaced distribution to acquire good spatial coverage. When the four satellites are deployed, they may not be evenly spaced, which would not meet the mission objectives.

However, MAGMA-C can still improve the current model for ionospheric currents, thereby delivering useful science data as a by product of its objective.

5.12.3 Risk Analysis

Figure 5.17 shows a quantified risk analysis of the mission, anything above orange is considered a risk failure.

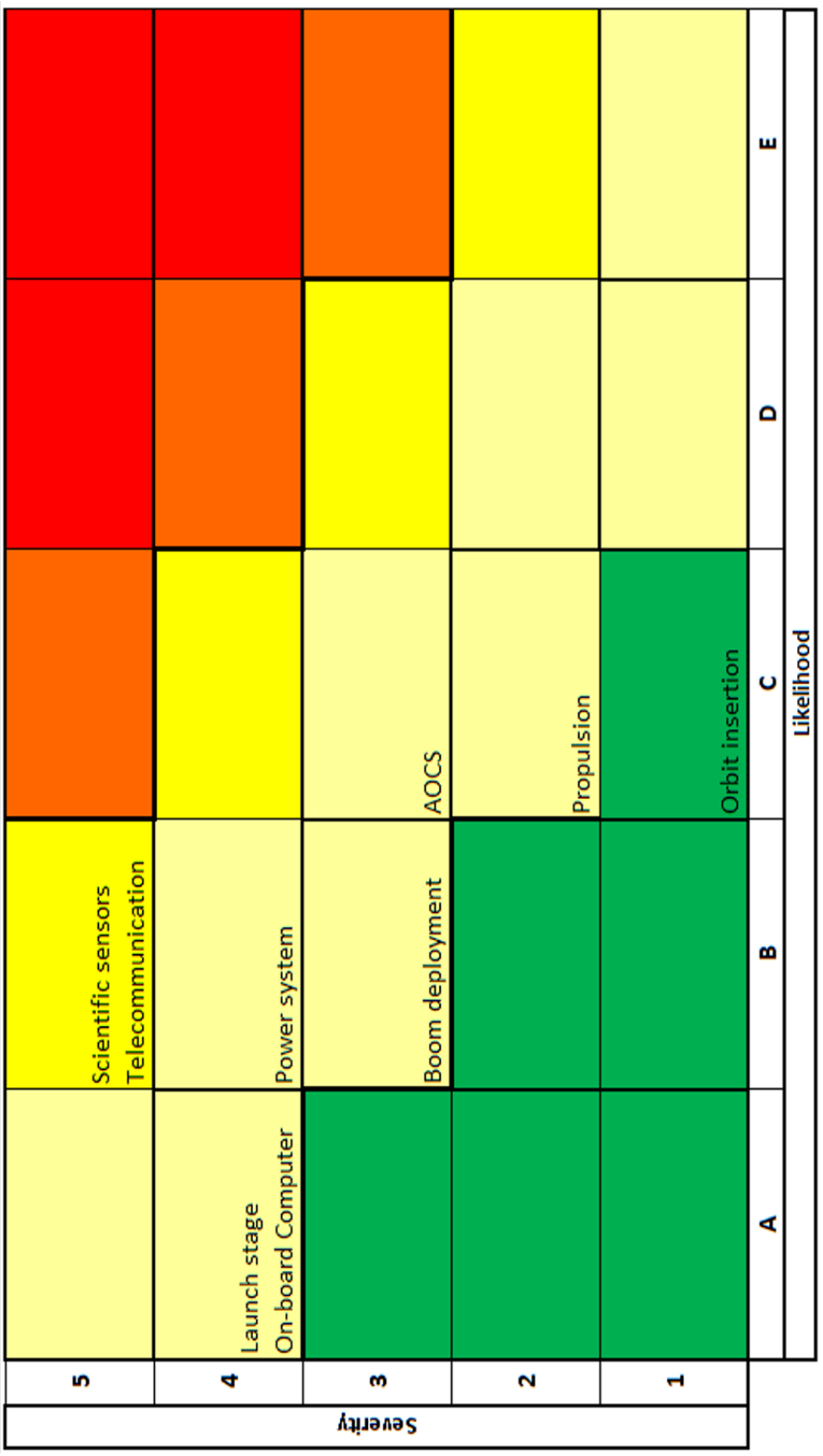

FIGURE 5.17: Risk Analysis

5.13 Programmatic Considerations

MAGMA-C could be launched in 2024, and would have an operational life time of 10 years. The mission format would be structured in the following fashion:

Mission Schedule Magma-C			
Phase 0	**Phase A**	**Phase B**	**Phase C**
2019 6 Months Feasibility Study	2020 12 Months Preliminary mission studies	2021 12 Months Detailed Definition studies	2022 18 Months phaseC/D Design, Development est
Phase D	**Phase E**	**Phase F**	
2023 18 Months phaseC/D Testing, Evaluation	2024 10 years Launch, Deployment	2035-2060 Estimated end Disposal	

Table 5.6: Mission Schedule

5.14 Conclusion

In this chapter the capabilities of a low cost micro-satellite mission were researched and proposed as part of Alpbach Summer School 2019, with the science requirement to expand the understanding of the Earth's magnetic field.

As there is already a rich heritage of missions based on other much more prevalent components of the Earth's magnetic field (SWARM, CHMAP, Orsted), exploration

into the unknown induced mantle would be our key objective. This objective would be achieved by measuring the inducing currents in the magnetosphere. In combination with ground based measurements and previous missions, using some clever data separation techniques (outlined in 5.7.1) the variables from Equation 5.1 could be separated into their component parts and the induced magnetic field could be found. From this the mantle's induced magnetic field could be measured at different depths depending on frequency as seen in Equation 5.14. These data could be used to map a 3D profile of the mantle conductivity.

Mapping the mantle's conductivity, enables insight into its water content, which will enrich the wealth of information on the structure and content of the Earth's mantle. From this better modelling of Earth's plate tectonics could be utilised to enhance early earthquake detection and volcanic activity.

Another advantageous by-product of this mission would be to improve existing models of the ionosphere. Taking advantage of the miniaturisation of electronics and the maturity of satellite constellation, MAGMA-C will use Commercial -Off-The-Shelf (COTS) components to deliver a low cost, low risk and feasible mission.

Appendix A

Lens Designer Code

```
```python
import numpy as np

def Lens_Designer(start_Er,thickness,focalLen,lens_radius,ring_radii,numRings):
    ##The user needs to define 6 important variables in order to ##
    ##determine the gradient profile lens##
    ## and the requied relative permittivites of each ring ##
    T = thickness
    F = focalLen
    Er_max = start_Er


    Diameters_Ring_Centers = np.linspace(
    ring_radii+0.5*ring_radii,
lens_radius-0.5*ring_radii,numRings-1)
    ##Determines the center of each ring ##
    Thetas = np.rad2deg(np.arctan(Diameters_Ring_Centers/F))

    print(Diameters_Ring_Centers)
    Ers = [Er_max]
    for theta in Thetas:
        ## Solves for the relative permittivities ##
        alpha = ((T/F)*np.sqrt(Er_max) - 1/np.cos(np.deg2rad(theta)) +1)/(T/F)
        gamma = (2/3)*(np.sin(np.deg2rad(theta))**2)
        kappa = gamma**2 + (alpha**2)*(np.sin(np.deg2rad(theta))**2)
        beta = (gamma + alpha**2)
```
```

```
        ## New Permittivity to the list for this lens Design ##
        Ern = (beta+(np.sqrt(beta**2 - 4*kappa)))/2
        if Ern < 1.0:
            print("Error!! Cant have Permittivity less than 1.0 try
            increassing focal len or thinkness")
            Ers.append((beta+(np.sqrt(beta**2 - 4*kappa)))/2)
        else:
            Ers.append((beta+(np.sqrt(beta**2 - 4*kappa)))/2)
    return Ers,lens_radius,ring_radii,numRings

def Get_Required_Infills(ERs,lens_radius,ring_radii,numRings):
    ## Boundary_Wall_Thickness ##
    T_boundary = 0.4

    ## Volume Percentage ##
    v = (np.asarray(ERs)-1)/(ERs[0]-1)
    Rs = np.linspace(ring_radii,lens_radius,numRings)
    Rs = np.sort(np.append(Rs,0))

    Infills = []
    for i,rn in enumerate(Rs):
        ##Caluclates the infill density needed for each ring ##
        try:
            a1 = v[i]*np.pi*(Rs[i+1]**2 - rn**2) - 2*np.pi*T_boundary*(Rs[i+1] + rn)
            a2 = np.pi*(Rs[i+1]**2 - rn**2 ) - 2*np.pi*T_boundary*(Rs[i+1] + rn)
            print("#%s Infill Percentage = %.1f percent, Start Radius = %.2f ,
            Er = %.2f,Volume Percentage = %.3f" %(i+1,a1/a2 * 100,rn,ERs[i],v[i]))
            Infills.append(a1/a2 * 100)
        except:
            #print("Outside Radii Bounds")
            break


    return Infills,ERs,Rs
%matplotlib notebook
import matplotlib.pyplot as plt
Ers, lens_radius, ring_radii, numRings = Lens_Designer(start_Er=2.62,thickness=10.0,
                                                       focalLen=250,lens_radius=50,
                                                       ring_radii=8.33,numRings=6)
## variables defined from lens designer function
Infills,ERs,Rs = Get_Required_Infills(Ers,lens_radius,ring_radii,numRings)
```

```
fig, ax = plt.subplots()
ax.set_title("Viz Lens")
Rs = Rs[::-1]
circles = []
colour = ['b','g','r','c','m','y','k']
for i,rn in enumerate(Rs):
    try:
        circle = plt.Circle((0, 0), Rs[i],color = colour[i])
        circles.append(circle)

    except:
        print("")
for c in circles:
    ax.add_artist(c)
ax.set_xlim(-lens_radius-5,lens_radius+5)
ax.set_ylim(-lens_radius-5,lens_radius+5)
ax.set_xlabel('x (mm)')
ax.set_ylabel('y (mm)')
ax.set_aspect(aspect='equal')
fig.savefig("C:/Users/daithi/OneDrive - Maynooth University/THZ Lab/ER_Lens_Designer")
'''
```

Appendix B

Ellipse parameters

```
"""
Created on Wed Oct 10 10:04:55 2018

@author: daithi
"""

import math as mt
import numpy as np


class SecondOrder(object):#r1,r2,angle_throw,inter_coord
""" Takes R1(length from the first focus to the reflector),
    R2(lenth of reflector to F2),Angle of reflection,the coordinate of
    the reflector. Outputs the equation the ellipse required to reflect the beam,
    distance between the focii and the vertex,the Origin(required for grasp) and
    the rotation value"""

    def __init__(self,r1,r2,angle_throw,inter_coord):

        self.r1=r1
        self.r2=r2
        self.angle_throw=angle_throw
        self.angle_throw=mt.radians(angle_throw)
        self.inter_coord=inter_coord
        self.a = (r1 + r2)/2
        theta=self.angle_throw/2.0
        self.b = mt.sqrt(r1*abs(r2))*mt.cos(theta) #Semi-minor axis
        self.e = mt.sqrt(1-(self.b**2/self.a**2))   #ecentricty
```

```
        self.cc=-1*self.e**2
        print("Your ecentricty is ",self.e)
        print("Your conic constant ",self.cc,".","a is ",self.a)


    def delta_foci(self):

        return np.sqrt((self.r1**2)+(self.r2**2)-(2*self.r1*self.r2*np.cos(self.angle_throw)))




    def ellipse_param(self):
        a=self.a
        b=self.b
        theta=self.angle_throw/2.0 # Angle of incident
        angle_throw=mt.radians(self.angle_throw)
        theta=mt.radians(theta)
        semi_major=2*a

        return semi_major,b

         def get_foci_vert(self):

        self.foci_vert=self.a*(1-self.e)
        print("Bug in code ?",self.foci_vert)
        return self.foci_vert



    #bbb=r2*mt.sin(theta)
    def polynomial_coefficients(self):

        rad=self.a*(1-self.e**2) #Radius of Curvature
        bb=((1+self.cc)/(2*rad)) #z-coefficient of the eq of the ellipse
        aa=(1/(2*rad)) #x and y coeffieent
        return aa,bb


    #Sine Rule
    def angle_of_rotation(self):

        r2=self.r2
```

```
        r1=self.r1
        angle_throw=self.angle_throw

        if r1<r2:
            d=(r2*mt.sin((angle_throw)))
            angle_b =(np.pi- abs(np.arcsin(d/self.delta_foci())))
            radii=(mt.degrees(angle_b))
            rotation=(round(radii,4))*-1

        else:
            d=(r2*mt.sin((angle_throw)))
            angle_b =np.arcsin(d/self.delta_foci())
            radii=(mt.degrees(angle_b))
            rotation=round(radii,4)




        return rotation,angle_b

    def angle_rot(self):

        a=self.a
        e=self.e
        angle_rot=np.arccos((a*(1-e**2)-1)/e)
        return angle_rot



    def angle_check(self):
        r2=self.r2
        r1=self.r1

        test=((r1**2+r2**2-self.delta_foci()**2)/(2*r1*r2))
        angle_c=mt.acos(test)
        angle_c=(mt.degrees(angle_c))
        return angle_c
     # X and Y points for the origin

    # if angle_throw>= (np.pi/2) and np.pi: # Any positive rotation larger than 90 smaller than 1
    def ellipse_rotation(self):

        r2=self.r2
        r1=self.r1
```

```
        rotation1,angle_b=self.angle_of_rotation()



        if r1>r2 and rotation1>=0:
           rotation="r1>r2",((90-rotation1)+90)
        if r1>r2 and rotation1<=0:
           rotation="r1>r2",((90-rotation1)+90)*-1

        if r1<r2 and rotation1>=0:
           rotation="r1<r2 pos",(180-abs(rotation1))
        if r1<r2 and rotation1<=0:
           rotation="r1<r2 neg",(180+rotation1)*-1




        return rotation

    def get_vertex_translation(self):

        r2=self.r2
        r1=self.r1
        angle_b,rotation=self.angle_of_rotation()
        angle_b=mt.radians(angle_b)
        foci_vert=self.get_foci_vert

        if r1>r2 and angle_b>0 :
            z_point= -1*(foci_vert()*mt.sin(abs(angle_b-(mt.pi/2))))-np.abs(self.inter_coord)
            x_point= foci_vert()*mt.cos(abs(angle_b-(mt.pi/2)))
            print("hi",self.inter_coord)

        if r1>r2 and angle_b<0 :

            z_point= (foci_vert()*mt.cos(abs(angle_b))+np.abs(self.inter_coord))
            x_point= foci_vert()*mt.sin(abs(angle_b))
            print("hi",self.inter_coord)

        if r1<r2 and angle_b>0 :

            z_point= (self.get_foci_vert()*mt.sin(abs(angle_b-(mt.pi/2))))-abs(self.inter_coord)
            x_point= self.get_foci_vert()*mt.cos(abs(angle_b-(mt.pi/2)))
        if r1<r2 and angle_b<0 :

            #z_point= abs(foci_vert()*mt.sin((np.pi/2)-(np.pi-abs(angle_b))))-np.abs(self.inter_
```

```
            # x_point= (foci_vert()*mt.cos((np.pi/2)-(np.pi-abs(angle_b))))
            # print("hi",self.inter_coord)
            z_point= (self.get_foci_vert()*mt.sin(abs(angle_b-(mt.pi/2))))-abs(self.inter_coord)
            x_point= self.get_foci_vert()*mt.cos(abs(angle_b-(mt.pi/2)))

        return x_point,z_point


    def get_vertex(self):

        angle_b,rotation=self.angle_of_rotation()
        angle_b=mt.radians(angle_b)

        vertex=(self.get_foci_vert()*mt.sin(abs(angle_b-(mt.pi/2))))
        print ("hi",mt.degrees(angle_b))
        return vertex
```

Bibliography

H. Akbari. *Beam plasma interactions and langmuir turbulence in the auroral ionosphere*. PhD thesis, 05 2015.

Joe Allen. Geomagnetism at ncei, Jul 2006. URL https://www.ngdc.noaa.gov/geomag/geomaginfo.shtml.

Ralph A. Alpher and Robert Herman. Evolution of the universe. *Nature*, 162 (4124):774–775, 1948. doi: 10.1038/162774b0. URL https://doi.org/10.1038/162774b0.

Carlos A. P. Bengaly, Javier E. Gonzalez, and Jailson S. Alcaniz. Is there evidence for a hotter Universe? (August), 2020. URL http://arxiv.org/abs/2007.13789.

C. L. Bennett, D. Larson, J. L. Weiland, N. Jarosik, G. Hinshaw, N. Odegard, K. M. Smith, R. S. Hill, B. Gold, M. Halpern, E. Komatsu, M. R. Nolta, L. Page, D. N. Spergel, E. Wollack, J. Dunkley, A. Kogut, M. Limon, S. S. Meyer, G. S. Tucker, and E. L. Wright. Nine-year Wilkinson Microwave Anisotropy Probe (WMAP) observations: Final maps and results. *Astrophysical Journal, Supplement Series*, 208(2):1–177, 2013. ISSN 00670049. doi: 10.1088/0067-0049/208/2/20.

L. G. Blok, M. L. Longana, H. Yu, and B. K.S. Woods. An investigation into 3D printing of fibre reinforced thermoplastic composites. *Additive Manufacturing*, 22(July):176–186, 2018. ISSN 22148604. doi: 10.1016/j.addma.2018.04.039.

Adam Byrne. Design and Analysis of Telescope Receiver Systems for Future Far-Infrared Missions Presented by. Master's thesis, Maynooth University, 2017.

Iurii Cherniak and Irina Zakharenkova. First observations of super plasma bubbles in Europe. *Geophysical Research Letters*, 43(21):11,137–11,145, nov 2016a. ISSN 19448007. doi: 10.1002/2016GL071421. URL http://doi.wiley.com/10.1002/2016GL071421.

Iurii Cherniak and Irina Zakharenkova. First observations of super plasma bubbles in Europe. *Geophysical Research Letters*, 43(21):11,137–11,145, 2016b. ISSN 19448007. doi: 10.1002/2016GL071421.

Joseph S. Choi and John C. Howell. Paraxial ray optics cloaking. *Opt. Express*, 22(24):29465–29478, Dec 2014. doi: 10.1364/OE.22.029465. URL http://www.opticsexpress.org/abstract.cfm?URI=oe-22-24-29465.

M Clemens and T Weiland. DISCRETE ELECTROMAGNETISM WITH THE FINITE INTEGRATION TECHNIQUE. Technical report, 2001.

CST. Cst studio suite 3d em simulation and analysis software, 2019. URL https://www.3ds.com/products-services/simulia/products/cst-studio-suite/.

Suie Help 2019 CST. No Title. URL file:///C:/ProgramFiles(x86)/CSTSTUDIOSUITE2019/OnlineHelp/cst{_}studio{_}suite{_}help.htm.

Antonio J. Cuesta, Licia Verde, Adam Riess, and Raul Jimenez. Calibrating the cosmic distance scale ladder: the role of the sound-horizon scale and the local expansion rate as distance anchors. *Monthly Notices of the Royal Astronomical Society*, 448(4):3463–3471, Mar 2015. ISSN 0035-8711. doi: 10.1093/mnras/stv261. URL http://dx.doi.org/10.1093/mnras/stv261.

R. Datta, J. Austermann, J. A. Beall, D. Becker, K. P. Coughlin, S. M. Duff, P. A. Gallardo, E. Grace, M. Hasselfield, S. W. Henderson, G. C. Hilton, S. P. Ho,

J. Hubmayr, B. J. Koopman, J. V. Lanen, D. Li, J. Mcmahon, C. D. Munson, F. Nati, M. D. Niemack, L. Page, C. G. Pappas, M. Salatino, B. L. Schmitt, A. Schillaci, S. M. Simon, S. T. Staggs, J. R. Stevens, E. M. Vavagiakis, J. T. Ward, and E. J. Wollack. Design and Deployment of a Multichroic Polarimeter Array on the Atacama Cosmology Telescope. *Journal of Low Temperature Physics*, 184:569, 2016. doi: 10.1007/s10909-016-1553-5.

R. H. Dicke, P. J. E. Peebles, P. G. Roll, and D. T. Wilkinson. Cosmic Black-Body Radiation. , 142:414–419, July 1965. doi: 10.1086/148306.

Lionel Duband. Space cryocooler developments. *Physics Procedia*, 67:1–10, 12 2015. doi: 10.1016/j.phpro.2015.06.003.

Ruth Durrer. The cosmic microwave background: The history of its experimental investigation and its significance for cosmology. *Classical and Quantum Gravity*, 32(12), 2015. ISSN 13616382. doi: 10.1088/0264-9381/32/12/124007.

ESA. eoPortal Directory - Satellite Missions, 2015a. URL https://directory.eoportal.org/web/eoportal/satellite-missions/c-missions/champhttps://directory.eoportal.org/web/eoportal/satellite-missions/l/lageos.

ESA. eoPortal Directory - Satellite Missions, 2015b. URL https://directory.eoportal.org/web/eoportal/satellite-missions/o/oersted{#}foot31{%}29https://directory.eoportal.org/web/eoportal/satellite-missions/l/lageos.

ESA. Swarm Publications - ESA EO Missions - Earth Online - ESA, 2020. URL https://earth.esa.int/web/guest/missions/esa-eo-missions/swarm/activities/publications.

ESA Alpbach Summer Scool. Magnetic Field Data Analysis_v5 - Google Docs. URL https://docs.google.com/document/d/1hKYgTuSvNo8zJ30Jh-DVbYmiw1qwpLL-wG{_}0oOJvAoM/edit.

J. Derek Fairhead. *Regional tectonics and basin formation: The role of potential field studies*. Elsevier B.V., 2012. ISBN 9780444530424. doi: 10.1016/B978-0-444-53042-4.00012-1. URL http://dx.doi.org/10.1016/B978-0-444-53042-4.00012-1.

Hongzhan Fei, Daisuke Yamazaki, Moe Sakurai, Nobuyoshi Miyajima, Hiroaki Ohfuji, Tomoo Katsura, and Takafumi Yamamoto. A nearly water-saturated mantle transition zone inferred from mineral viscosity. *Science Advances*, 3 (6):e1603024, jun 2017. ISSN 23752548. doi: 10.1126/sciadv.1603024. URL https://advances.sciencemag.org/lookup/doi/10.1126/sciadv.1603024.

A. G. Fox and Tingye Li. Resonant Modes in a Maser Interferometer. *Bell System Technical Journal*, 40(2):453–488, 1961. ISSN 15387305. doi: 10.1002/j.1538-7305.1961.tb01625.x.

K.-H. Glassmeier and B. T. Tsurutani. Carl Friedrich Gauss – General Theory of Terrestrial Magnetism – a revised translation of the German text . *History of Geo- and Space Sciences*, 5(1):11–62, 2014. ISSN 2190-5029. doi: 10.5194/hgss-5-11-2014.

Paul F. Goldsmith. *Quasioptical Systems*. IEEE Press, 1998. ISBN 0780310179.

Dave Goodwin. Big bang, 2012. ISSN 02624079.

Athanasios Goulas, Shiyu Zhang, Darren A. Cadman, Jan Järveläinen, Ville Mylläri, Will G. Whittow, John (Yiannis) C. Vardaxoglou, and Daniel S. Engstrøm. The Impact of 3D Printing Process Parameters on the Dielectric Properties of High Permittivity Composites. *Designs*, 3(4):50, 2019. ISSN 2411-9660. doi: 10.3390/designs3040050.

Marcin Gradziel and Neil Trappe. Model driven standing wave altering in compact free space millimetre wave Vector Network Analyser driven measurement systems. Research group internal memo, 2018.

Louise M Griffiths, Domingos Barbosa, and Andrew R Liddle. Cosmic microwave background constraints on the epoch of reionization. Technical report, 1999.

Alan H. Guth. Inflationary universe: A possible solution to the horizon and flatness problems. *Physical Review D*, 23(2):347–356, 1981. ISSN 05562821. doi: 10.1103/PhysRevD.23.347.

D Hanson, S Hoover, A Crites, P A R Ade, K A Aird, J E Austermann, J A Beall, A N Bender, B A Benson, L E Bleem, J J Bock, J E Carlstrom, C L Chang, H C Chiang, H-M Cho, A Conley, T M Crawford, T De Haan, M A Dobbs, W Everett, J Gallicchio, J Gao, E M George, N W Halverson, N Harrington, J W Henning, G C Hilton, G P Holder, W L Holzapfel, J D Hrubes, N Huang, J Hubmayr, K D Irwin, R Keisler, L Knox, A T Lee, E Leitch, D Li, C Liang, D Luong-Van, G Marsden, J J Mcmahon, J Mehl, S S Meyer, L Mocanu, T E Montroy, T Natoli, J P Nibarger, K K Schaffer, B Schulz, G Smecher, A A Stark, K T Story, C Tucker, K Vanderlinde, J D Vieira, M P Viero, G Wang, V Yefremenko, O Zahn, and M Zemcov. Detection of B-mode Polarization in the Cosmic Microwave Background with Data from the South Pole Telescope. Technical report, 2013.

Steen G. Hanson, Michael L. Jakobsen, and Harold T. Yura. *Complex-valued ABCD matrices and speckle metrology*, volume 198. 2016. ISBN 9781493930289. doi: 10.1007/978-1-4939-3028-9_14.

Bogna Haponiuk. Snell's Law Calculator, 2020. URL https://www.omnicalculator.com/physics/snells-law.

B Holback, Å Jacksén, L Åhlén, S Jansson, A I Eriksson, J Wahlund, T Carozzi, and J Bergman. Annales Geophysicae LINDA – the Astrid-2 Langmuir probe instrument. *Langmuir*, pages 601–610, 2001.

Paul A. Hsieh, John D. Bredehoeft, and John M. Farr. Determination of aquifer transmissivity from Earth tide analysis. *Water Resources Research*, 23(10): 1824–1832, 1987. ISSN 19447973. doi: 10.1029/WR023i010p01824.

Wayne Hu. CMB Temperature and Polarization Anisotropy Fundamentals. Technical report.

Wayne Hu. *Wandering in the Background: A Cosmic Microwave Background Explorer*. PhD thesis, University of California, Berkeley, 1990.

Wayne Hu and Martin White. A CMB polarization primer. *New Astronomy*, 2 (4):323–344, 1997. ISSN 13841076. doi: 10.1016/S1384-1076(97)00022-5.

Jin Huang, Shenjian Jammy Chen, Zhenghui Xue, Withawat Withayachumnankul, and Christophe Fumeaux. Impact of Infill Pattern on 3D Printed Dielectric Resonator Antennas. In *Proceedings of the 2018 IEEE 7th Asia-Pacific Conference on Antennas and Propagation, APCAP 2018*, pages 233–235. Institute of Electrical and Electronics Engineers Inc., nov 2018. ISBN 9781538656488. doi: 10.1109/APCAP.2018.8538296. URL https://ieeexplore.ieee.org/document/8538296/.

Marc Imbert, Anna Papio, Franco De Flaviis, Lluis Jofre, and Jordi Romeu. Design and performance evaluation of a dielectric flat lens antenna for millimeter-wave applications. *IEEE Antennas and Wireless Propagation Letters*, 14(c):342–345, 2015. ISSN 15361225. doi: 10.1109/LAWP.2014.2363596.

Wei Jiang, Leilei Yan, Hua Ma, Ya Fan, Jiafu Wang, Mingde Feng, and Shaobo Qu. Electromagnetic wave absorption and compressive behavior of a three-dimensional metamaterial absorber based on 3D printed honeycomb. *Scientific Reports*, 8(1), dec 2018. ISSN 20452322. doi: 10.1038/s41598-018-23286-6.

K. S. Karkare, P. A. R. Ade, Z. Ahmed, R. W. Aikin, K. D. Alexander, M. Amiri, D. Barkats, S. J. Benton, C. A. Bischoff, J. J. Bock, J. A. Bonetti, J. A. Brevik, I. Buder, E. W. Bullock, B. Burger, J. Connors, B. P. Crill, G. Davis, C. D. Dowell, L. Duband, J. P. Filippini, S. T. Fliescher, S. R. Golwala, M. S. Gordon, J. A. Grayson, M. Halpern, M. Hasselfield, S. R. Hildebrandt, G. C. Hilton, V. V. Hristov, H. Hui, K. D. Irwin, J. H. Kang, E. Karpel, S. Kefeli, S. A. Kernasovskiy, J. M. Kovac, C. L. Kuo, E. M. Leitch, M. Lueker, P. Mason, K. G. Megerian, C. B. Netterfield, H. T. Nguyen, R. O'Brient, R. W. Ogburn, C. L. Pryke, C. D. Reintsema, S. Richter, R. Schwarz, C. D. Sheehy, Z. K. Staniszewski, R. V. Sudiwala, G. P. Teply, K. L. Thompson, J. E. Tolan, A. D. Turner, A. Vieregg, A. Weber, C. L. Wong, W. L. K. Wu, and K. W. Yoon. Keck array and BICEP3: spectral characterization of 5000+ detectors. In Wayne S. Holland and Jonas Zmuidzinas, editors, *Millimeter, Submillimeter, and Far-Infrared Detectors and Instrumentation for Astronomy VII*, volume 9153, page 91533B. SPIE, aug 2014. ISBN 9780819496218. doi: 10.1117/12.2056779. URL http://proceedings.spiedigitallibrary.org/proceeding.aspx?doi=10.1117/12.2056779.

K.S. Kelleher and C. Goatley. *Electronics*. H. W. MATEER, 1955a.

K.S. Kelleher and C. Goatley. Dielectric Lens for Microwaves. *Electronics*, pages 142–145, 1955b.

Paul Kelly. Analysis of Quasi-Optical Components for Far-Infrared Astronomy. Master's thesis, Maynooth University, Maynooth, Co. Kildare, Ireland.

Maxim Yu. Khlopov and Sergei G. Rubin. *Cosmological Pattern of Microphysics in the Inflationary Universe*. Springer Netherlands, Dordrecht, 2004. doi: 10.1007/978-1-4020-2650-8. URL http://link.springer.com/10.1007/978-1-4020-2650-8.

Sung Kim and James Baker-Jarvis. An Approximate Approach to Determining the Permittivity and Permeability near $\lambda/2$ Resonances in Transmission/Reflection Measurements. Technical report, 2014.

Haje Korth, Kim Strohbehn, Francisco Tejada, Andreas G. Andreou, John Kitching, Svenja Knappe, S. John Lehtonen, Shaughn M. London, and Matiwos Kafel. Miniature atomic scalar magnetometer for space based on the rubidium isotope 87Rb. *Journal of Geophysical Research: Space Physics*, 121(8):7870–7880, August 2016. ISSN 21699402. doi: 10.1002/2016JA022389.

Herbert Kramer. Observation of the Earth and Its Environment: Survey of Missions and Sensors, 2002a. URL https://directory.eoportal.org/web/eoportal/satellite-missions/content/-/article/electron-launcher-of-rocket-lab.

Herbert Kramer. Oersted - eoPortal Directory - Satellite Missions, 2002b. URL https://earth.esa.int/web/eoportal/satellite-missions/o/oersted.

Herbert J Kramer. Observation of the earth and its environment: Survey of missions and sensors, 2002c. URL https://directory.eoportal.org/web/eoportal/satellite-missions/s/swarm.

KU Leuven. KU Leuven Star Tracker, n.d. URL http://www.cubesatpointing.com/DownloadFiles/Datasheets/KULSTDatasheet.pdf.

publisher=Livil Center of Institute for Space Research year=2015 month=Nov LEMI, journal=LEMI 020. Digital magnetometer for microsatellites lemi-020. URL https://www.isr.lviv.ua/lemi020.htm.

Lepine-Szily, A. Lépine-Szily, Alinka Descouvemont, Pierre Descouvemont, and Pierre. Nuclear astrophysics: Nucleosynthesis in the universe. *International Journal of Astrobiology*, 11:243–250, 10 2012. doi: 10.1017/S1473550412000158.

Lorenzo Luini, Roberto Nebuloni, and Carlo Riva. Ka-to-W Band EM Wave Propagation: Tropospheric Effects and Countermeasures. In *Wave Propagation Concepts for Near-Future Telecommunication Systems*. InTech, May 2017. doi: 10.5772/66660. URL http://www.intechopen.com/books/wave-propagation-concepts-for-near-future-telecommunication-systems/ka-to-w-band-em-wave-propagation-tropospheric-effects-and-countermeasures.

Jean-Pierre Luminet, Jeffrey R. Weeks, Alain Riazuelo, Roland Lehoucq, and Jean-Philippe Uzan. Dodecahedral space topology as an explanation for weak wide-angle temperature correlations in the cosmic microwave background. *Nature*, 425(6958):593–595, Oct 2003. ISSN 1476-4687. doi: 10.1038/nature01944. URL https://doi.org/10.1038/nature01944.

Per Lundahl Thomsen and Flemming Hansen. Danish Ørsted Mission In-Orbit Experiences and Status of The Danish Small Satellite Programme. Technical report.

Luxorion. Ionospheric perturbations, 2000. URL http://www.astrosurf.com/luxorion/qsl-perturbation.htm.

D. H. Martin and E. Puplett. Polarised interferometric spectrometry for the millimetre and submillimetre spectrum. *Infrared Physics*, 10(2):105–109, jun 1970. ISSN 00200891. doi: 10.1016/0020-0891(70)90006-0. URL https://linkinghub.elsevier.com/retrieve/pii/0020089170900060.

Enda McLoughlin. Optimisation of a Near-Field Scanning System. Master's thesis, Maynooth University, 2012.

Mustafa Megahed. Additive Manufacturing: Revolutionizing How Products Are Made. *ESItalk*, (47):1–24, 2016. ISSN 0361-0853, 0361-0853. doi: 10.1016/B978-0-08-099922-7.00011-1. URL https://linkinghub.elsevier.com/retrieve/pii/B9780080999227000111.

Aghanim Nabila et al. Polarised Radiation Interferometer for Spectral disTortions and INflation Exploration. 2018.

National Instruments. Introduction to Network Analyzer Measurements. *National Instruments RF Academy*, pages 1–44, 2012.

Huaiwei Ni, Yong-Fei Zheng, Zhu Mao, Qin Wang, Ren-Xu Chen, and Li Zhang. Distribution, cycling and impact of water in the Earth's interior. *National Science Review*, 4:879–891, 2017. doi: 10.1093/nsr/nwx130. URL https://academic.oup.com/nsr/article/4/6/879/4569204.

Northrop, Grumman. Pegasus Rocket – Northrop Grumman. URL https://www.northropgrumman.com/space-old/pegasus-rocket/.

Eiji Ohtani. The role of water in Earth's mantle. *National Science Review*, 7(1): 224–232, 2020. ISSN 2053714X. doi: 10.1093/nsr/nwz071.

N. Olsen. Induction studies with satellite data. *Surveys in Geophysics*, 20(3-4): 309–340, 1999. ISSN 01693298. doi: 10.1023/a:1006611303582.

Nils Olsen. The electrical conductivity of the mantle beneath Europe derived from C-responses from 3 to 720 hr. *Geophysical Journal International*, 133(2): 298–308, 1998. ISSN 0956540X. doi: 10.1046/j.1365-246X.1998.00503.x.

Nils Olsen, Hermann Lühr, Terence J Sabaka, Mioara Mandea, Martin Rother, Lars Tøffner-Clausen, and Sungchan Choi. CHAOS-a model of the Earth's magnetic field derived from CHAMP, Ørsted, and SAC-C magnetic satellite data. *Geophys. J. Int*, 166:67–75, 2006. doi: 10.1111/j.1365-246X.2006.02959.x. URL https://academic.oup.com/gji/article/166/1/67/633768.

Nils Olsen, Gauthier Hulot, and Terence J. Sabaka. *Sources of the Geomagnetic Field and the Modern Data That EnableTheir Investigation*, pages 105–124. Springer Berlin Heidelberg, Berlin, Heidelberg, 2010a. ISBN 978-3-642-01546-5. doi: 10.1007/978-3-642-01546-5_5. URL https://doi.org/10.1007/978-3-642-01546-5_5.

Nils Olsen, Gauthier Hulot, and Terence J. Sabaka. *Sources of the Geomagnetic Field and the Modern Data That EnableTheir Investigation*, pages 105–124. Springer Berlin Heidelberg, Berlin, Heidelberg, 2010b. ISBN 978-3-642-01546-5. doi: 10.1007/978-3-642-01546-5_5. URL https://doi.org/10.1007/978-3-642-01546-5_5.

OrbitalATK. Coilable Boom Systems. pages 0–1, 2015.

Créidhe O'Sullivan and J Anthony Murphy. *Terahertz Sources , Detectors , and Optics*. SPIE press, Bellingham, Washington USA, 2012. ISBN 9780819491671.

J. R. Pardo, J. Cernicharo, and E. Serabyn. Atmospheric transmission at microwaves (atm): an improved model for millimeter/submillimeter applications. *IEEE Transactions on Antennas and Propagation*, 49(12):1683–1694, 2001.

High Performance and Green Propulsion. FLIGHT-PROVEN. High Performance Green Propulsion. URL http://ecaps.space/assets/pdf/Bradford{_}ECAPS{_}Folder{_}2017.pdf.

Planck. Looking back to the dawn of time. 2009. URL www.esa.int.

Planck Collaboration, Aghanim, N., Akrami, Y., Arroja, F., Ashdown, M., Aumont, J., Baccigalupi, C., Ballardini, M., Banday, A. J., Barreiro, R. B., Bartolo, N., Basak, S., Battye, R., Benabed, K., Bernard, J.-P., Bersanelli, M., Bielewicz, P., Bock, J. J., Bond, J. R., Borrill, J., Bouchet, F. R., Boulanger, F., Bucher,

M., Burigana, C., Butler, R. C., Calabrese, E., Cardoso, J.-F., Carron, J., Casaponsa, B., Challinor, A., Chiang, H. C., Colombo, L. P. L., Combet, C., Contreras, D., Crill, B. P., Cuttaia, F., de Bernardis, P., de Zotti, G., Delabrouille, J., Delouis, J.-M., Désert, F.-X., Di Valentino, E., Dickinson, C., Diego, J. M., Donzelli, S., Doré, O., Douspis, M., Ducout, A., Dupac, X., Efstathiou, G., Elsner, F., Enßlin, T. A., Eriksen, H. K., Falgarone, E., Fantaye, Y., Fergusson, J., Fernandez-Cobos, R., Finelli, F., Forastieri, F., Frailis, M., Franceschi, E., Frolov, A., Galeotta, S., Galli, S., Ganga, K., Génova-Santos, R. T., Gerbino, M., Ghosh, T., González-Nuevo, J., Górski, K. M., Gratton, S., Gruppuso, A., Gudmundsson, J. E., Hamann, J., Handley, W., Hansen, F. K., Helou, G., Herranz, D., Hildebrandt, S. R., Hivon, E., Huang, Z., Jaffe, A. H., Jones, W. C., Karakci, A., Keihänen, E., Keskitalo, R., Kiiveri, K., Kim, J., Kisner, T. S., Knox, L., Krachmalnicoff, N., Kunz, M., Kurki-Suonio, H., Lagache, G., Lamarre, J.-M., Langer, M., Lasenby, A., Lattanzi, M., Lawrence, C. R., Le Jeune, M., Leahy, J. P., Lesgourgues, J., Levrier, F., Lewis, A., Liguori, M., Lilje, P. B., Lilley, M., Lindholm, V., López-Caniego, M., Lubin, P. M., Ma, Y.-Z., Macías-Pérez, J. F., Maggio, G., Maino, D., Mandolesi, N., Mangilli, A., Marcos-Caballero, A., Maris, M., Martin, P. G., Martinelli, M., Martínez-González, E., Matarrese, S., Mauri, N., McEwen, J. D., Meerburg, P. D., Meinhold, P. R., Melchiorri, A., Mennella, A., Migliaccio, M., Millea, M., Mitra, S., Miville-Deschênes, M.-A., Molinari, D., Moneti, A., Montier, L., Morgante, G., Moss, A., Mottet, S., Münchmeyer, M., Natoli, P., Nørgaard-Nielsen, H. U., Oxborrow, C. A., Pagano, L., Paoletti, D., Partridge, B., Patanchon, G., Pearson, T. J., Peel, M., Peiris, H. V., Perrotta, F., Pettorino, V., Piacentini, F., Polastri, L., Polenta, G., Puget, J.-L., Rachen, J. P., Reinecke, M., Remazeilles, M., Renault, C., Renzi, A., Rocha, G., Rosset, C., Roudier, G., Rubiño-Martín, J. A., Ruiz-Granados, B., Salvati, L., Sandri, M., Savelainen, M., Scott, D., Shellard, E. P. S., Shiraishi, M., Sirignano, C., Sirri, G., Spencer, L. D., Sunyaev, R., Suur-Uski, A.-S., Tauber, J. A., Tavagnacco, D., Tenti, M., Terenzi, L., Toffolatti, L.,

Tomasi, M., Trombetti, T., Valiviita, J., Van Tent, B., Vibert, L., Vielva, P., Villa, F., Vittorio, N., Wandelt, B. D., Wehus, I. K., White, M., White, S. D. M., Zacchei, A., and Zonca, A. Planck 2018 results - i. overview and the cosmological legacy of planck. *A&A*, 641:A1, 2020. doi: 10.1051/0004-6361/201833880. URL https://doi.org/10.1051/0004-6361/201833880.

Mei Qing Qi, Wen Xuan Tang, and Tie Jun Cui. A broadband bessel beam launcher using metamaterial lens. *Scientific Reports*, 5, 2015. ISSN 20452322. doi: 10.1038/srep11732. URL www.nature.com/scientificreports.

Antonio Riotto. Inflation and the Theory of Cosmological Perturbations. (July 2002):1–95, 2002. URL http://arxiv.org/abs/hep-ph/0210162.

Terence J Sabaka, Lars Tøffner-Clausen, and Nils Olsen. Use of the Comprehensive Inversion method for Swarm satellite data analysis. In *Earth Planets Space*, volume 65, pages 1201–1222, 2013. doi: 10.5047/eps.2013.09.007.

Terence J. Sabaka, Lars Tøffner-Clausen, Nils Olsen, and Christopher C. Finlay. A comprehensive model of Earth's magnetic field determined from 4 years of Swarm satellite observations. *Earth, Planets and Space*, 70(1), 2018. ISSN 18805981. doi: 10.1186/s40623-018-0896-3. URL https://doi.org/10.1186/s40623-018-0896-3.

Libor Sachl and Ladislav Hanyk. Magnetic Signatures of Barotropic and Baroclinic Flows in Swarm Data. 2015.

A. A. Samarskii, P. N. Vabishchevich, O. P. Iliev, and A. G. Churbanov. Numerical simulation of convection/diffusion phase change problems-a review. *International Journal of Heat and Mass Transfer*, 36(17):4095–4106, 1993. ISSN 00179310. doi: 10.1016/0017-9310(93)90071-D.

Giorgio Savini, Peter A R Ade, and Jin Zhang. Gradient-index lenses; (160.1245) Artificially engineered materials; (220.3630) Lenses; (260.2710) Inhomogeneous optical media. Technical report, 2012. URL www.ansys.com.

Brandon Schmandt, Steven D. Jacobsen, Thorsten W. Becker, Zhenxian Liu, and Kenneth G. Dueker. Dehydration melting at the top of the lower mantle. *Science*, 344(6189):1265–1268, 2014a. ISSN 10959203. doi: 10.1126/science.1253358.

Brandon Schmandt, Steven D. Jacobsen, Thorsten W. Becker, Zhenxian Liu, and Kenneth G. Dueker. Dehydration melting at the top of the lower mantle. *Science*, 344(6189):1265–1268, jun 2014b. ISSN 10959203. doi: 10.1126/science.1253358. URL https://www.sciencemag.org/lookup/doi/10.1126/science.1253358.

Alexey Semenov and Alexey Kuvshinov. Global 3-D imaging of mantle conductivity based on inversion of observatory C-responses-II. Data analysis and results. *Geophysical Journal International Geophys. J. Int*, 191:965–992, 2012. doi: 10.1111/j.1365-246X.2012.05665.x. URL https://academic.oup.com/gji/article/191/3/965/564956.

Shaul Shauly, Michael D. Niemack, and Lyman Page. CMB telescopes and optical systems. *Planets, Stars and Stellar Systems: Volume 1: Telescopes and Instrumentation*, 1:431–480, 2013. doi: 10.1007/978-94-007-5621-2_10.

National Geographic Society. Mantle, Oct 2012. URL https://www.nationalgeographic.org/encyclopedia/mantle/#:~:text=1/12-,Themantleisthemostly-solidbulkofEarth'sinterior,84%ofEarth'stotalvolume.

Erwan Thébault, Michael Purucker, Kathryn A Whaler, Benoit Langlais, and Terence J Sabaka. The magnetic field of the earth's lithosphere. In *Space Science Reviews*, volume 155, pages 95–127, 2010. doi: 10.1007/s11214-010-9667-6.

Neil Trappe. *Quasi-optical Analysis of thre HIFI Instrument fro the Herschel Space Telescope*. PhD thesis, Maynooth University, 2002.

TRICA. *GRASP User's Manual GRASP User's Manual*. TRICA, LANDEMÆRKET 29 DK-1119 COPENHAGEN K,DENMARK, 10.5.0 edition, 2015.

Niall Tynan. Accurate Characterisation of Refractive Components for Future CMB Missions. Master's thesis, Maynooth University, 2016.

Md Uddin, Md Kowsher, and Mir Md Moheuddin. A new method of central difference interpolation. Vol.6:14, 09 2019.

Pyotr Ya. Ufimtsev. *Wedge Diffraction: The Physical Optics Field*, chapter 3, pages 87–102. John Wiley Sons, Ltd, 2014. ISBN 9781118753767. doi: 10.1002/9781118753767.ch3. URL https://onlinelibrary.wiley.com/doi/abs/10.1002/9781118753767.ch3.

Louis Vaught. What is the best infill pattern for 3D printing? - Quora. URL https://www.quora.com/What-is-the-best-infill-pattern-for-3D-printing.

Michael Voplatka. Esa – 18. díl – astronomický stroj času, Apr 2014. URL https://kosmonautix.cz/2014/04/esa-18-dil-astronomicky-stroj-casu/.

Pam Waterman. 3D Printing Infill Styles – the What, When and Why of Using Infill, 2019. URL https://www.padtinc.com/blog/3d-printing-infill-styles-the-what-when-and-why-of-using-infill/.

T. Weiland. Time domain electromagnetic field computation with finite difference methods. *International Journal of Numerical Modelling: Electronic Networks, Devices and Fields*, 9(4):295–319, 1996. ISSN 08943370. doi: 10.1002/(SICI)1099-1204(199607)9:4⟨295::AID-JNM240⟩3.0.CO;2-8.

William B. Weir. Automatic Measurement of Complex Dielectric Constant and Permeability at Microwave Frequencies. *Proceedings of the IEEE*, 62(1):33–36, 1974. ISSN 15582256. doi: 10.1109/PROC.1974.9382.

D M White, A Zacchei, and A Zonca. Planck 2018 results. VI. Cosmological parameters Planck. *Astronomy & Astrophysics*, 62, 2018. URL https://pla.esac.esa.int.

Quentin Williams. Why is the earth's core so hot? and how do scientists measure its temperature? *Scientific American*, Oct 1997. URL https://www.scientificamerican.com/article/why-is-the-earths-core-so/.

Ken Wong. The "unknown thru" calibration advantage. *63rd ARFTG Conference Digest, Spring 2004, Automatic RF Techniques Group: On Wafer Characterization*, pages 73–81, 2004. doi: 10.1109/arftg.2004.1387858.

Shiyu Zhang, Ravi Kumar Arya, Shaileshchandra Pandey, Yiannis Vardaxoglou, Will Whittow, and Raj Mittra. 3D-printed planar graded index lenses. *IET Microwaves, Antennas and Propagation*, 10(13):1411–1419, 2016. ISSN 17518733. doi: 10.1049/iet-map.2016.0013.